

COMPUTATIONAL ANALYSIS OF THE OBSERVED  
SELECTIVITIES AND YIELDS FROM THE PRODUCTION  
OF BENZOTHAIAZOLE DERIVATIVES



A THESIS SUBMITTED IN PARTIAL FULFILLMENT OF THE REQUIREMENT FOR  
THE DEGREE OF MASTER OF SCIENCE IN APPLIED CHEMISTRY  
DEPARTMENT OF CHEMISTRY SCHOOL OF SCIENCE  
KING MONGKUT'S INSTITUTE OF TECHNOLOGY LADKRABANG  
2024

KMITL-2024-SC-M-012-061

This material is reserved for educational use only, not allowed for commercial use.

Forbidden to modify the content, and cite the document when use.



**COPYRIGHT 2024**

**SCHOOL OF SCIENCE**

**KING MONGKUT'S INSTITUTE OF TECHNOLOGY LADKRABANG**

This material is reserved for educational use only, not allowed for commercial use.

Forbidden to modify the content, and cite the document when use.

Thesis Title	Computational Analysis of the Observed Selectivities and Yields from the Production of Benzothiazole Derivatives
Student Name	Pacharaporn Krawmanee
Student ID	62605048
Degree	Master of Science (Applied Chemistry)
Department	Chemistry
Year	2024
Thesis Advisor	Assoc. Prof. Dr. Duangkamol Gleeson

### Abstract

Synthesis of novel benzothiazoles via intramolecular C–S bond formation reactions is increasingly being explored since they have been found in a wide range of natural products and pharmaceutical agents. Sharma et al. reported the ruthenium-catalyzed preparation of novel benzothiazole derivatives from *N*-arylthiourea precursors, with a range of reaction yields and selectivity being observed. We have employed a density functional theory-based computational model to investigate the reaction mechanism leading to the benzothiazole product and help uncover the origin of the differing experimental yields and substrate specificities. We proposed a modified mechanistic scheme where the rate-determining step to be the synchronized breaking of the peroxide bond of the oxidizing agent with the concomitant proton-coupled electron transfer from the haloarene urea and a Ru-bound water molecule, not electrophilic Ru–C bond activation. Evidence for this being the rate-determining step is (a) the barrier is consistent with a lack of kinetic isotope effects associated with the *ortho*-H atom and (b) the computed rate-determining barriers for 10 *N*-arylthiourea substrates show good correlation with the observed yield.

Keywords : mechanism, ruthenium catalyst, DFT, benzothiazoles, *N*-arylthiourea

## Acknowledgements

I would like to acknowledge several individuals who have contributed to my research and thesis and have supported me in several ways.

Firstly, I would like to express my deepest gratitude to my thesis advisor, Assoc. Prof. Dr. Duangkamol Gleeson of the Department of Science and Assoc. and Prof. Dr. Mathew Paul Gleeson of the Department of Biomedical Engineering at King Mongkut's Institute of Technology Ladkrabang, for their invaluable guidance, support and encouragement throughout my research over the years. Their expertise and helpful suggestions have helped improve the quality of this work and gave me great research experience.

Additionally, this study has received financial support from King Mongkut's Institute of Technology Ladkrabang (KMITL), TSRI and NSRF. I would like to acknowledge support by the School of Science, KMITL, (RA/TA-2562-M017).

Secondly, I would like to thank members of the Computational & Medicinal Chemistry Laboratory (CMCL) for their help, support and friendship. Furthermore, I would like to extend my heartfelt thanks to my close friend for continuous support and always cheering me on throughout this journey.

Finally, I am profoundly thankful to my family for their love and support. Thank you for always standing by my side all the time, whether I am tired or happy. Thank you for their trust and belief until the completion of this project.

Pacharaporn Krawmanee

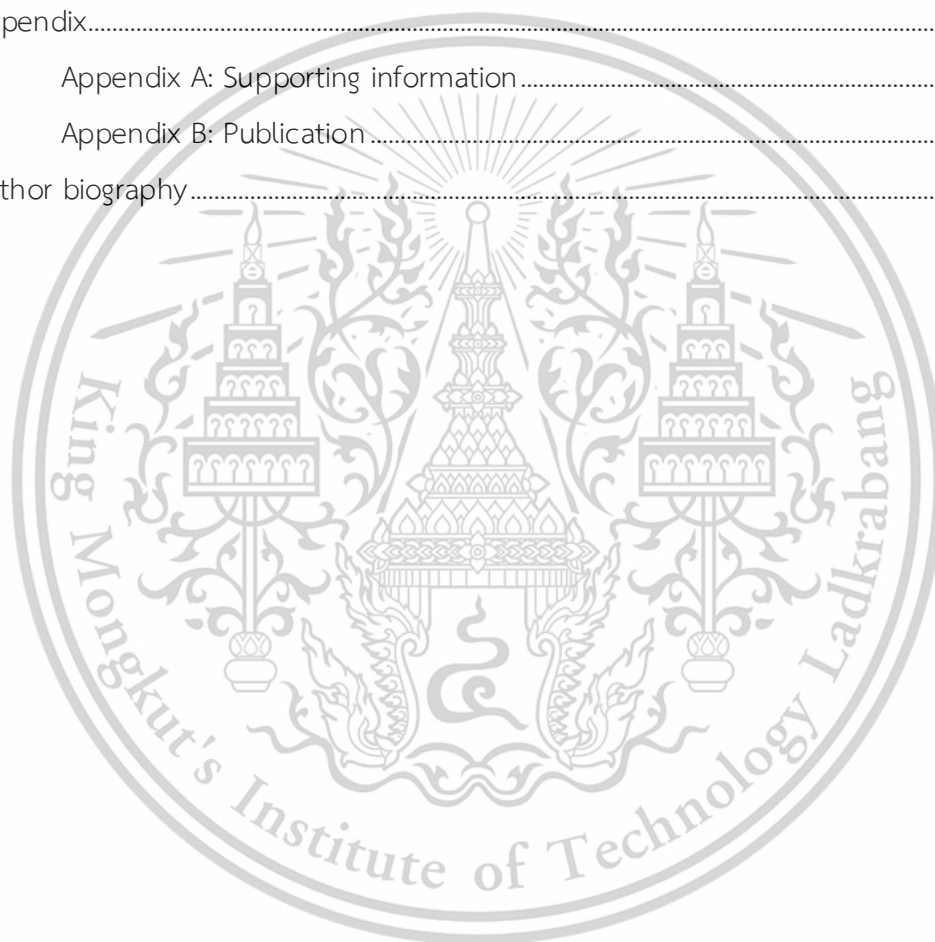
# Table of contents

	Page
Abstract.....	i
Acknowledgements.....	ii
Table of contents.....	iii
List of tables.....	v
List of schemes.....	vi
List of figures.....	viii
<b>Chapter 1</b> .....	<b>1</b>
1.1 Research motivation .....	1
1.2 Objectives of the study .....	2
1.3 Scopes of the study .....	2
1.4 Benefits of the study .....	3
<b>Chapter 2</b> .....	<b>4</b>
2.1 Benzothiazole .....	4
2.2 Synthesis of benzothiazole .....	4
2.2.1 Condensation of 2-aminothiophenols with aldehydes .....	4
2.2.2 Condensation of 2-aminothiophenols with ketones .....	7
2.2.3 Condensation of 2-aminobenzenethiols with acyl chlorides .....	8
2.2.4 Condensation of 2-aminobenzenethiols with acids .....	9
2.2.5 Cyclization of diverse substituted thioamides .....	10
2.2.6 Cyclization of CO <sub>2</sub> as raw materials .....	10
2.2.7 C–S coupling via C–H bond functionalization .....	11
2.3 Computational chemistry .....	15
2.3.1 Density Functional Theory (DFT) .....	15
2.3.2 Basis sets .....	19
2.3.3 Restricted and unrestricted configurations .....	23
2.3.4 Spin density and spin contamination .....	25
2.4 Kinetic isotope effect .....	28
2.5 Literature reviews.....	31
<b>Chapter 3</b> .....	<b>35</b>

This material is reserved for educational use only, not allowed for commercial use.

Forbidden to modify the content, and cite the document when use.

<b>Chapter 4</b> .....	<b>38</b>
4.1 Pathway A .....	41
4.2 Pathway B .....	47
4.3 Pathway C .....	50
4.4 Probable reaction mechanism .....	51
4.5 Correlation of yield vs. RDS barrier .....	52
<b>Chapter 5</b> .....	<b>56</b>
References .....	58
Appendix.....	66
Appendix A: Supporting information.....	67
Appendix B: Publication .....	76
Author biography.....	86



This material is reserved for educational use only, not allowed for commercial use.

Forbidden to modify the content, and cite the document when use.

## List of tables

Table	Page
2.1 the value of $S^2$ is calculated and compared to $S(S+1)$ .....	23
4.1 The computed $\Delta E$ and $\Delta G$ energies of stationary points using the UB3PW91/6-31+G**/LANL2DZ level. The $\Delta E_{sp}$ correspond to the single point energy of stationary points using the UB3PW91/6-311++G**/def2-TZVP level. Energies are reported in kcal/mol and relative to the reactant. Absolute barriers heights are in parenthesis. ....	40
4.2 Computed energies obtained from the examination of the influence of electron-donating and electron-withdrawing groups substituent on the <i>ortho</i> -, <i>meta</i> -, and <i>para</i> -positions. Energies are relative to the reactant and reported in kcal/mol.	53



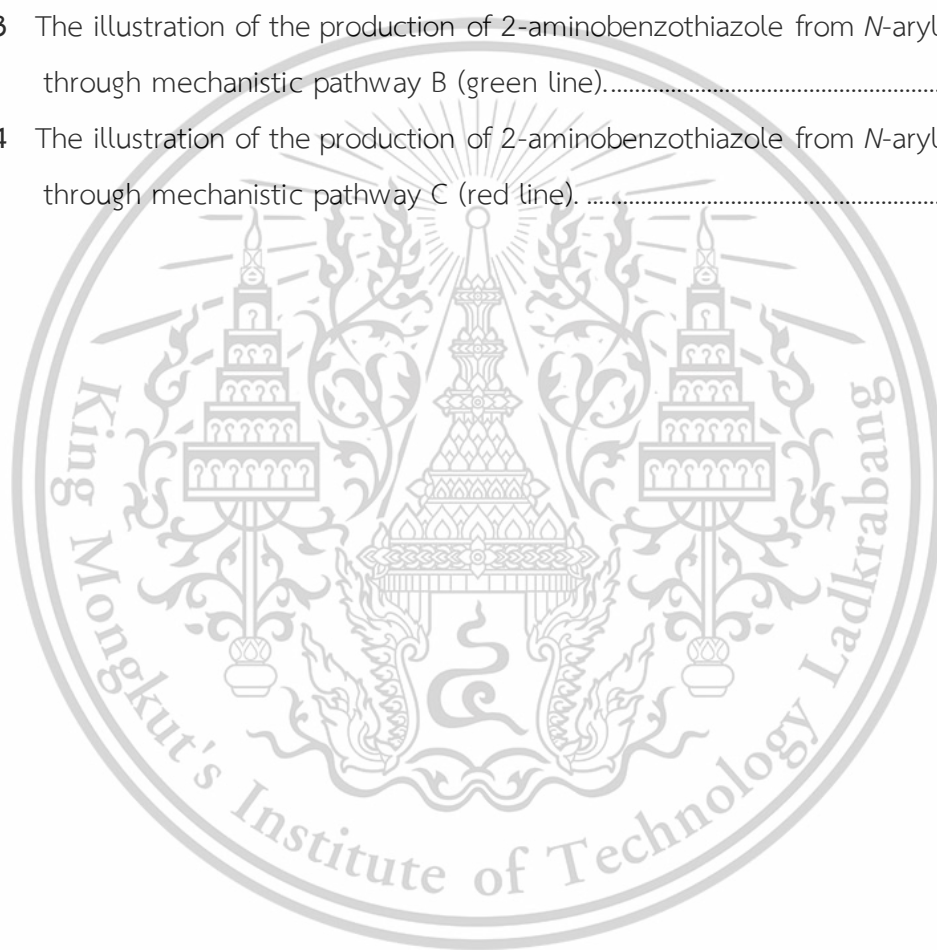
## List of schemes

Scheme	Page
2.1 Interaction of 2-aminobenzenethiol with 5-aldehyde bisthiophene through condensation process to generate benzothiazole.....	5
2.2 Interaction of 2-aminobenzenethiol with benzaldehyde through condensation process to generate benzothiazole. ....	5
2.3 The condensation process between 2-aminothiophenol and aldehyde under visible light generates benzothiazole.....	6
2.4 The condensation process between 2-aminothiophenol and aromatic aldehyde generates benzothiazole. ....	6
2.5 The synthesis of benzothiazole through condensation of 2-aminothiophenol and aryl aldehyde.....	6
2.6 Condensation process of 2-aminobenzenethiol with $\beta$ -diketone to generate benzothiazole.....	7
2.7 Condensation process of aryl methyl ketones and 2-aminobenzenethiol to generate benzothiazole.....	8
2.8 The reaction of thiols, oxalyl chloride and 2-aminothiophenol facilitates the formation of benzothiazole.....	8
2.9 The interaction between 2-aminothiophenol and chloroacetyl chloride through the condensation process. ....	9
2.10 Interaction of 2-aminobenzenethiol with aliphatic or aromatic carboxylic acids to generate benzothiazole.....	9
2.11 The condensation process between 2-aminothiophenol disulfides and carboxylic acids to generate benzothiazole.....	10
2.12 Cyclization of thioamide derivatives.....	10
2.13 The cyclization of 2-aminobenzenethiol and CO <sub>2</sub> to generate benzothiazole product.....	10
2.14 Patel's palladium and copper-catalyzed synthesis of benzothiazoles. ....	12
2.15 Mechanism for the differential selectivity using palladium catalyst. ....	12
2.16 The production of 2-aminobenzothiazoles from aryl isothiocyanates by copper catalyst.....	14

This material is reserved for educational use only, not allowed for commercial use.

Forbidden to modify the content, and cite the document when use.

2.17	Mechanism for copper catalyzed oxidative cyclization of <i>N</i> -arylthiourea. ....	14
2.18	Ruthenium catalyzed intramolecular C–S coupling leading to 2-aminobenzothiazole. ....	31
3.1	Proposed mechanism leading to the preparation of 2-aminobenzothiazoles. ....	35
4.1	Illustration of the discrete steps involved in the production of 2-aminobenzothiazole from <i>N</i> -arylthiourea. ....	39
4.2	The illustration of the production of 2-aminobenzothiazole from <i>N</i> -arylthiourea through mechanistic pathway A (blue line). ....	42
4.3	The illustration of the production of 2-aminobenzothiazole from <i>N</i> -arylthiourea through mechanistic pathway B (green line). ....	47
4.4	The illustration of the production of 2-aminobenzothiazole from <i>N</i> -arylthiourea through mechanistic pathway C (red line). ....	50



## List of figures

Figure	Page
2.1 Chemical structure of Benzothiazole.....	4
2.2 Flowchart of density functional theory (DFT) calculation.....	19
2.3 Spin restricted configurations require both alpha ( $\alpha$ ) and beta ( $\beta$ ) spins to occupy the same spatial orbitals (left). For spin unrestricted configurations allow each spin (alpha ( $\alpha$ ) or beta ( $\beta$ )) to occupy different spatial orbital (right).....	24
2.4 Calculated structures of 12, 13, and 14 using DFT method.....	32
2.5 Explanation for the rational behind the regiochemical outcome of NO <sub>2</sub> -phenylthiourea. ....	32
3.1 The yield for 10 <i>N</i> -arylthioureas which cover a range of electron-donating/neutral (MeO, H) and withdrawing groups (F, Cl, Br, I, and NO <sub>2</sub> ) at the <i>ortho</i> -, <i>meta</i> - and <i>para</i> - positions of the aryl thioureas.....	36
4.1 Computed reaction energy profile corresponding to the production of 2-aminobenzothiazole from <i>N</i> -arylthiourea.....	41
4.2 Optimized geometries obtained in the production of 2-aminobenzothiazole from <i>N</i> -arylthiourea in mechanistic pathway A (blue line). Key distances are illustrated in Å. ....	46
4.3 Optimized geometries obtained in the production of 2-aminobenzothiazole from <i>N</i> -arylthiourea in mechanistic pathway B (green line). Key distances are illustrated in Å. (For REACT, TS1, INT1, TS2, INT2 and TS3 can see at Figure 4.2).....	49
4.4 Optimized geometries obtained in the production of 2-aminobenzothiazole from <i>N</i> -arylthiourea in mechanistic pathway C (red line). Key distances are illustrated in Å. (For REACT, TS1 and INT1 can see at Figure 4.2).....	51
4.5 A comparison of TS1 (M = 4) energy barriers and %yield, obtained for 9a and the substituents on the <i>ortho</i> -, <i>meta</i> -, and <i>para</i> -positions. ....	54
5.1 Drugs designed for chemical synthesis to improve reactivity for high yield.....	57

# Chapter 1

## Introduction

### 1.1 Research motivation

Benzothiazole is an important heterocyclic compound found in a wide range of pharmaceutically active agents and natural products. It represents a common heterocyclic scaffold consisting of a benzene ring fused with a thiazole ring containing sulfur and nitrogen in its thiazole structure. Benzothiazole and its derivatives have been reported to possess anticancer, antimicrobial, anti-inflammatory, anti-viral, and other activities [1-6]. As a result of the benefits mentioned above, there has been significant effort in exploring new ways to prepare molecules of this class [7-10]. The classical synthesis of 2-aminobenzothiazoles involves the intramolecular aromatic electrophilic substitution of thiobenzanilides using various oxidants and condensation of 2-aminothiophenols with aldehydes or carboxylic acids. This includes the cyclization of *N*-(2-halo)arylthioureas or direct intramolecular C–S bond formations via C–H functionalization of *N*-arylthiourea under transition metal catalysis, which expands the range of synthesis methods [11-12]. Progress towards the development of transition metal catalyzed reactions for the construction of C–S bonds has been challenging compared to other carbon-heteroatom coupling types (C–C or C–N) [13-16] due to difficulties related to efficiency and selectivity. However, these problems have largely been overcome through the identification of new transition metal catalysts in conjunction with C–H bond functionalization [17-21].

Sharma et al. [18] reported the synthesis of 2-aminobenzothiazoles from *N*-arylthioureas using a Ru-catalyzed intramolecular C–S coupling reaction with oxone acting as the reducing agent. The screening of diverse *N*-arylthioureas demonstrated the reaction had a broad scope, with electron-donating substituents generally displaying higher reactivity. The authors proposed a five-step mechanism based on kinetic isotope effect (KIE) data, which indicated that the more conventional direct C–H bond activation was not rate-determining. Instead, they suggested an electrophilic Ru-mediated rate-determining step consistent with the KIE data where the *ortho* carbon transitions from  $sp^2$  to  $sp^3$ , without involving C–H bond activation. Limited DFT

calculations exploring the reaction were performed, predicting the rate-determining barrier to be 26.5 kcal/mol.

Computational methods have proven extremely useful in clarifying experimental phenomenon associated with Ru-based catalytic systems. Therefore, these methods have been applied to further explore the mechanistic proposals associated with the ruthenium-catalyzed formation of benzothiazoles from *N*-arylthioureas. This study expands on the DFT reported by Sharma et al. [18] by using a larger octahedral  $\text{RuCl}_3$ -based DFT model in contrast to the previously tetrahedral configuration and includes the required oxidizing agent. This more complete model allows to investigate the five steps in the proposed mechanism, as well as other possibilities. Additionally, the effect of spin on the Ru (II/III) system on the structures and energetics is also considered [22-24].

## 1.2 Objectives of the study

- 1) To validate or revise the current mechanistic proposal related to the ruthenium catalyzed formation of 2-aminobenzothiazoles from *N*-arylthioureas.
- 2) To confirm the rate-determining step of the reaction.
- 3) To determine whether the proposed mechanism can explain the experimental yields of the diverse substrates, which range from 55% to 91%. This understanding should facilitate the design of future catalysts for the synthesis of novel benzothiazole derivatives.

## 1.3 Scopes of the study

This study is divided into two main paths :

- 1) The validity of current and two new mechanistic proposals associated with benzothiazole production is examined using DFT calculations and considers the effect of spin on the structures and energetics of the Ru(II/III) system.
- 2) To evaluate the validity of the new mechanistic proposal, the correlation between the rate-determining barrier and the yield for 10 *N*-arylthioureas is examined. These cover a range of electron-donating/neutral and withdrawing groups at the *ortho*-, *meta*-, and *para*- positions of the aryl thioureas.

#### 1.4 Benefits of the study

1) Computational simulations of benzothiazole derivatives provide clear insights into the reaction mechanism at the molecular level.

2) Rationalization of the selectivities and yields of organic chemistry reaction. It is highly sought after for the preparation of fine chemicals for industry or drug molecules in the pharmaceutical industry.



This material is reserved for educational use only, not allowed for commercial use.

Forbidden to modify the content, and cite the document when use.

## Chapter 2

# Theory and literature reviews

### 2.1 Benzothiazole

Benzothiazole (Figure 2.1) is a class of heterocyclic compounds containing a benzene ring fused with a five-membered ring that consists of nitrogen and sulfur atoms. The benzothiazole ring system was found in diverse marine and terrestrial natural compounds, which have a broad range of pharmaceutical applications. Especially, the benzothiazole group displays an important role in medicinal chemistry and is also demonstrated in a various of biologically active compounds [5-6, 25] including antitumor, anticancer, antibacterial, antimicrobial, antidiabetic, anti-inflammatory, anticonvulsant, antiviral, antioxidant, antitubercular, antimalarial, antiasthmatic, anthelmintic, photosensitizing, diuretic, analgesic and other activities. Therefore, the study of benzothiazoles is considered to be of great interest by reason of their high pharmaceutical and biological activity.

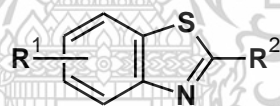
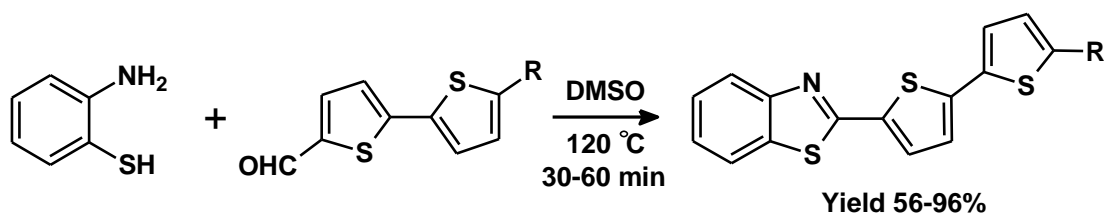


Figure 2.1 Chemical structure of Benzothiazole.

### 2.2 Synthesis of benzothiazole

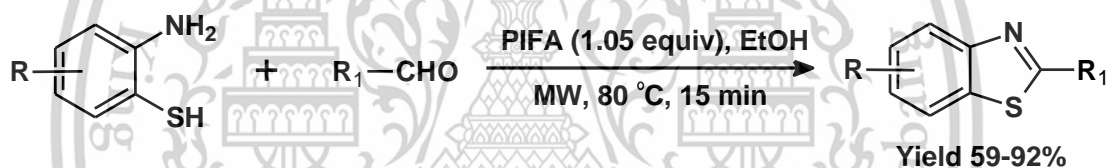
#### 2.2.1 Condensation of 2-aminothiophenols with aldehydes

Products of 2-bisthiophene substituted benzothiazole are obtained through the condensation reaction between 2-aminobenzenethiol and 5-aldehyde bisthiophene compounds by using dimethyl sulfoxide (DMSO) under reflux conditions for 1 hour. (Scheme 2.1) [26]. The evaluation proceeded with the fluorescent properties of the products. In the range of 450-600 nm, they exhibited strong fluorescence, significant Stokes shifts and high quantum yields. These compounds could potentially be applied as fluorescent markers due to their intense fluorescence.



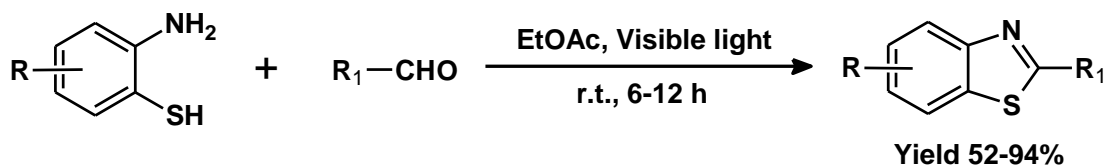
**Scheme 2.1** Interaction of 2-aminobenzenethiol with 5-aldehyde bisthiophene through condensation process to generate benzothiazole.

The synthesis of benzothiazoles through condensation of 2-aminobenzenethiol with benzaldehyde compounds by using phenyl iodoniumbis(triuroacetate) (PIFA) as the oxidizing agent could be effectively promoted under microwave conditions (Scheme 2.2) [27]. Compared to traditional heating methods, the use of microwave irradiation significantly reduces reaction time, improve yields and broadens the scope of applicable substrates.



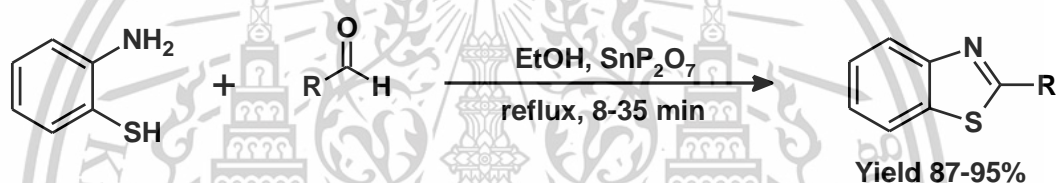
**Scheme 2.2** Interaction of 2-aminobenzenethiol with benzaldehyde through condensation process to generate benzothiazole.

A visible light could promote the preparation of benzothiazole products from 2-aminothiophenol and aldehyde (Scheme 2.3). The reaction system was exposed to irradiation from a 12W blue LED for 6 hours under the air [28]. A variety of aldehydes were investigated to assess the reaction's applicability across various substrates, revealing that aromatic, heteroaromatic and aliphatic aldehydes are compatible. This discovery provides an efficient, non-transitional metal catalyst, an additional additive and presents a convenient synthetic method for producing benzothiazole.



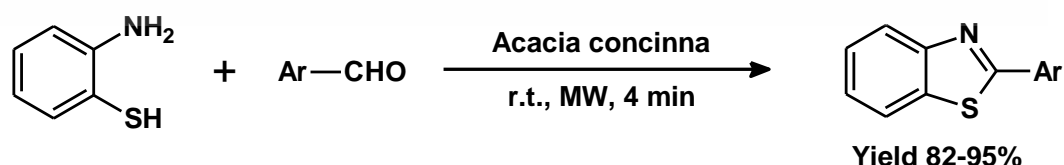
**Scheme 2.3** The condensation process between 2-aminothiophenol and aldehyde under visible light generates benzothiazole.

An effective, simple, environmentally friendly approach for the production of benzothiazole involves the condensation reaction of 2-aminothiophenol with diverse aromatic aldehyde employing SnP<sub>2</sub>O<sub>7</sub> as a novel heterogeneous catalyst (Scheme 2.4). This approach yields high product efficiency (87–95%) with short reaction times and the catalyst could be reused without any degradation of its activity [29].



**Scheme 2.4** The condensation process between 2-aminothiophenol and aromatic aldehyde generates benzothiazole.

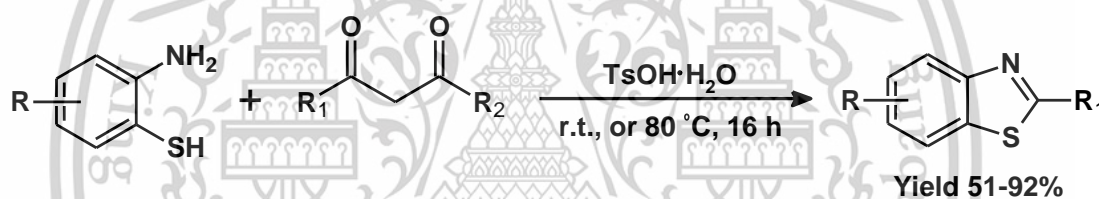
The rapid synthesis of 2-aryl-benzothia/(oxa)zole is achieved through the condensation reaction of 2-aminothiophenol and various aryl aldehydes using *Acacia concinna* as a biocatalyst under microwave irradiation (Scheme 2.5) [30]. Compared to traditional approach, the microwave irradiation technique offers significantly shorter reaction times with higher yields of the desired products. Additionally, this process is environmentally friendly, as it is carried out without the use of solvents.



**Scheme 2.5** The synthesis of benzothiazole through condensation of 2-aminothiophenol and aryl aldehyde.

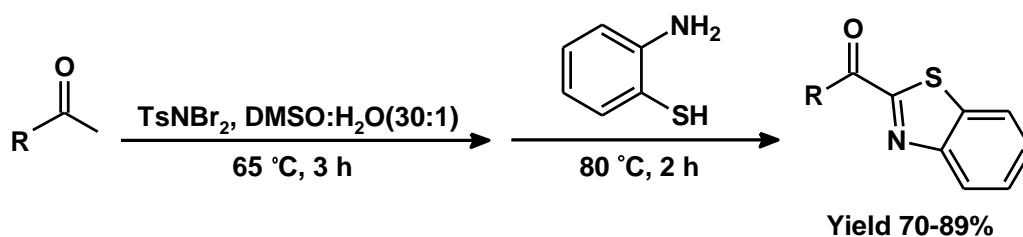
### 2.2.2 Condensation of 2-aminothiophenols with aetones

The condensation reaction between 2-aminobenzenethiol and  $\beta$ -diketone was catalyzed toluenesulfonic acid under metal-, radiation- and oxidant-free conditions to provide 2-substituted benzenes in great yields (Scheme 2.6). To identify the optimal catalytic system, the authors attempted various acids, such as benzoic acid (PhCOOH), trifluoroacetic acid (CF<sub>3</sub>COOH), and acetic acid (CH<sub>3</sub>COOH). However, TsOH·H<sub>2</sub>O was selected as a catalyst for solvent screening in terms of yield. The mechanism revealed that the Brønsted acid-catalyzed condensation reaction of 2-amino thiophenol with 2,4-pentanedione would occur to generate a ketamine intermediate in the presence of TsOH·H<sub>2</sub>O. The intramolecular nucleophilic addition and the C–C bond cleavage reaction would finally occur to generate the desired product. The advantages of this method include simple procedures, readily available raw materials, mild reaction conditions, broad substrate universality and good application potential [31].



Scheme 2.6 Condensation process of 2-aminobenzenethiol with  $\beta$ -diketone to generate benzothiazole.

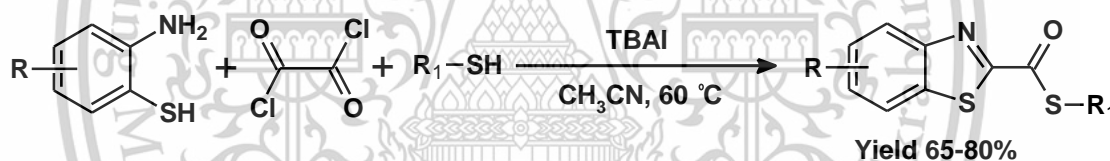
A one pot strategy has been developed for the synthesis of 2-acylbenzothiazoles under metal-free conditions. The reaction proceeded with aryl methyl ketones and 2-aminobenzenethiol (Scheme 2.7). The mechanism revealed that the aromatic ketones are reacted with TsNBr<sub>2</sub> in DMSO at 65 °C for 3 hours. The resulting crude reaction mixture is treated with 2-aminobenzenethiol through condensation reaction, Michael addition and oxidative dehydrogenation sequence to produce the desired product [32].



**Scheme 2.7** Condensation process of aryl methyl ketones and 2-aminobenzenethiol to generate benzothiazole.

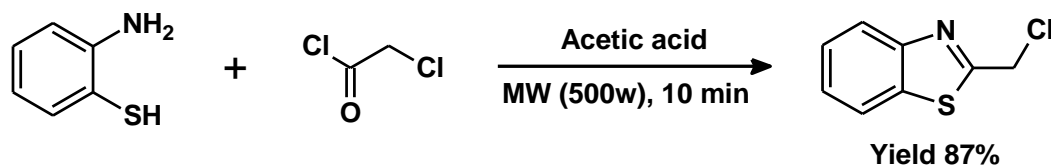
### 2.2.3 Condensation of 2-aminobenzenethiols with acyl chlorides

The synthesis of benzothiazoles is achieved through a one-pot, three-component reaction involving thiols, oxalyl chloride, and 2-aminothiophenol within the system of n-tetrabutylammonium iodide (TBAI) at 60 °C (Scheme 2.8). The present methodology favored the preparation of the desired products in good yields with a wide range of substrates through simultaneous formation of C–N and C–S bonds. The advantages of this method include mild reaction conditions and high efficiency [33].



**Scheme 2.8** The reaction of thiols, oxalyl chloride and 2-aminothiophenol facilitates the formation of benzothiazole.

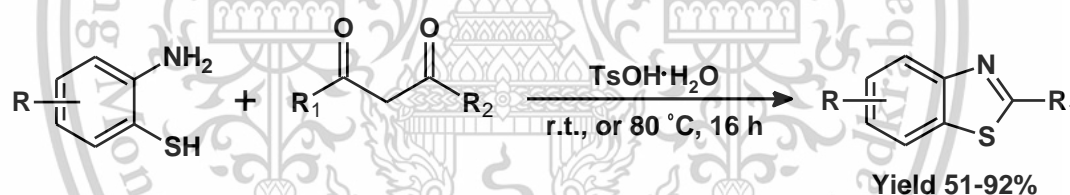
The 2-chloromethyl-benzothiazole could be achieved from the condensation reaction of 2-aminothiophenols with chloroacetyl chloride under microwave irradiation for 10 min in the presence of acetic acid (Scheme 2.9). In comparison to traditional methods, the microwave-assisted procedures are more efficient and environmentally friendly, offering shorter reaction times and high yield [34].



**Scheme 2.9** The interaction between 2-aminothiophenol and chloroacetyl chloride through the condensation process.

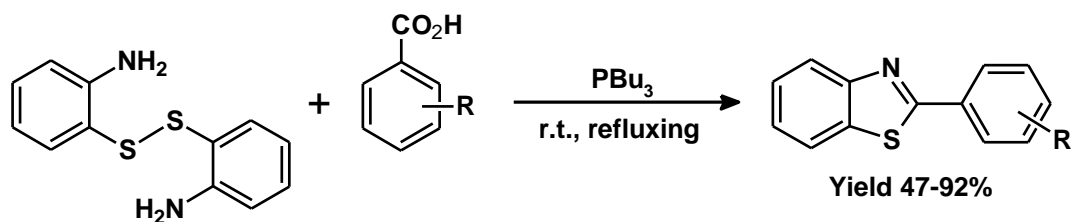
#### 2.2.4 Condensation of 2-aminobenzenethiols with acids

The synthesis of 2-substituted benzothiazole through the condensation reaction of 2-aminobenzenethiol with various types of aliphatic or aromatic carboxylic acids (Scheme 2.10). The novel heterogeneous mixture of methanesulfonic acid and silica gel had been developed as an efficient medium for the synthesis of 2-substituted benzothiazole. Moreover, the silica gel could be reused multiple times without a reduction in yield. This method offers several advantages including simplicity, the use of readily available and diverse carboxylic acids and ease of handling under reaction conditions [35].



**Scheme 2.10** Interaction of 2-aminobenzenethiol with aliphatic or aromatic carboxylic acids to generate benzothiazole.

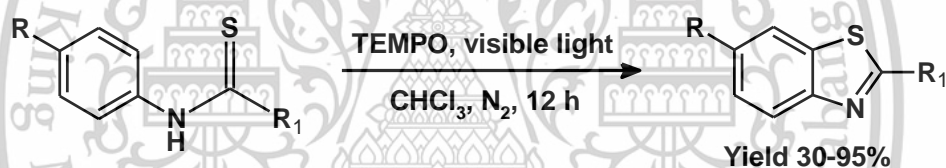
A common and efficient methodology to synthesize benzothiazole through the condensation reaction of 2-aminothiophenol disulfides with carboxylic acids in the presence of tributylphosphine at room temperature (Scheme 2.11). This method was explored using 2-aminothiophenol disulfides and a variety of carboxylic acids containing both electron-donating and electron-withdrawing substituents. This resulted in the formation of the desired benzothiazole with moderate to good yields. The advantages of this approach include mild reaction conditions and the use of non-toxic reagents [36].



**Scheme 2.11** The condensation process between 2-aminothiophenol disulfides and carboxylic acids to generate benzothiazole.

### 2.2.5 Cyclization of diverse substituted thioamides

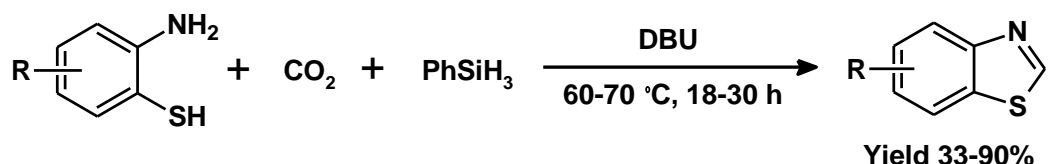
A methodology has been developed for visible light-driven, intramolecular C–S bond formation of aromatic substrates to synthesize benzothiazole in good yields through the cyclization of thioamide derivatives under 2,2,6,6-tetramethylpiperidine *N*-oxide (TEMPO) (Scheme 2.12). Notably, this photochemical cyclization proceeds without the need for an additional photoredox catalyst, transition-metal catalyst, or base [37].



**Scheme 2.12** Cyclization of thioamide derivatives.

### 2.2.6 Cyclization of CO<sub>2</sub> as raw materials

The preparation of benzothiazoles is achieved from 2-aminobenzenethiols and carbon dioxide under the condition of 1,8-diazabicyclo[5.4.0]undec-7-ene (DBU) at 1 atm of CO<sub>2</sub> and 60–70 °C (Scheme 2.13). The reaction exhibited a wide scope of substrate and demonstrated good tolerance for functional groups. Additionally, the precatalyst salt could be reused multiple times without any reduction in activity [38].



**Scheme 2.13** The cyclization of 2-aminobenzenethiol and CO<sub>2</sub> to generate benzothiazole product.

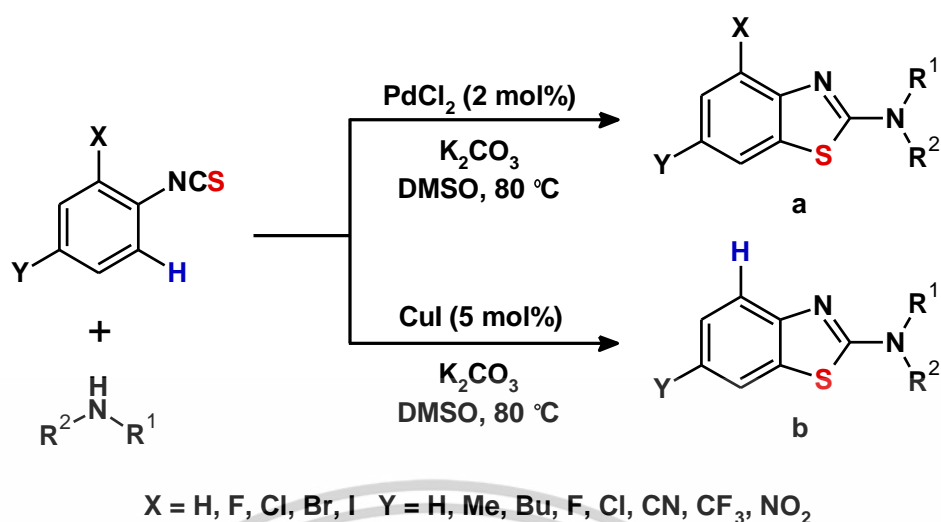
This material is reserved for educational use only, not allowed for commercial use.

Forbidden to modify the content, and cite the document when use.

### 2.2.7 C–S coupling via C–H bond functionalization

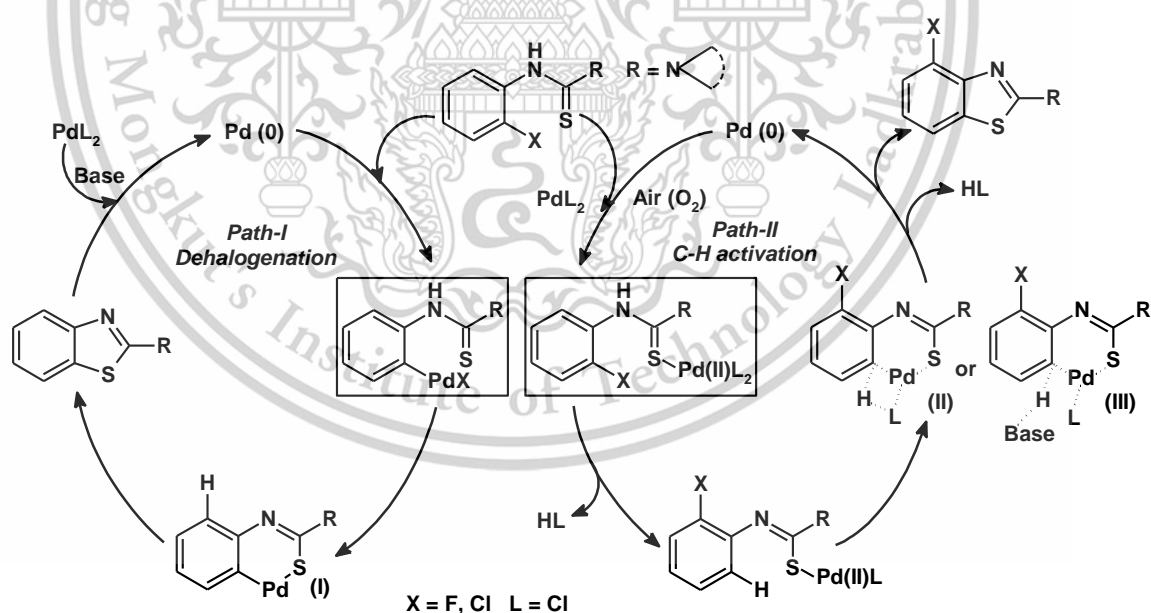
The ability to activate the typically inert C–H bonds have significance for hydrocarbon functionalization, which necessitates the cleavage of at least one C–H bond. These bonds are generally challenging to cleave directly because of their thermodynamic stability (calculated at approximately 420 kcal/mol for primary C–H bonds). Traditionally, the formation of C–C bonds in alkanes through C–H bond activation has often depended on radical chemistry. However, the selective functionalization of C–H bonds with sulfur groups is less frequent due to the limited availability of suitable reagents that can accommodate sulfur-containing functional groups. The challenge in expanding this area is finding new transition metal complexes that can efficiently surmount the thermodynamic and kinetic barriers associated with C–H bond activation [17]. The application of C–H activation facilitated by specific transition metals to generate carbon–heteroatom (S, N, O) bonds is a valuable asset in pharmaceutical and medicinal chemistry [39]. Transition metals, with their varied oxidation states, are ideal catalysts for C–H activation. Generally, transition metal ions act as effective electron-pair acceptors that easily bind to electron-rich molecules and anions. The interaction between metals and ligands can cause changes in the relevant frontier molecular orbitals, potentially enhancing the conditions for efficient C–S bond coupling.

Patel and co-workers discovered that regioselective formation of intramolecular C–S bonds (a and b) occurs during the synthesis of 2-aminobenzothiazole from 2-halo-substituted thioureas, utilizing either PdCl<sub>2</sub> or CuI as the catalyst (Scheme 2.14) [11].



Scheme 2.14 Patel's palladium and copper-catalyzed synthesis of benzothiazoles.

In many instances, the reactions involving substrates with less reactive 2-halo groups favored the C–H activation via palladium rather than proceeding through the dehalogenation pathway. The specificity of the reactions is influenced by the choice of the metal catalyst as well as the substituents present on the aryl thioureas.



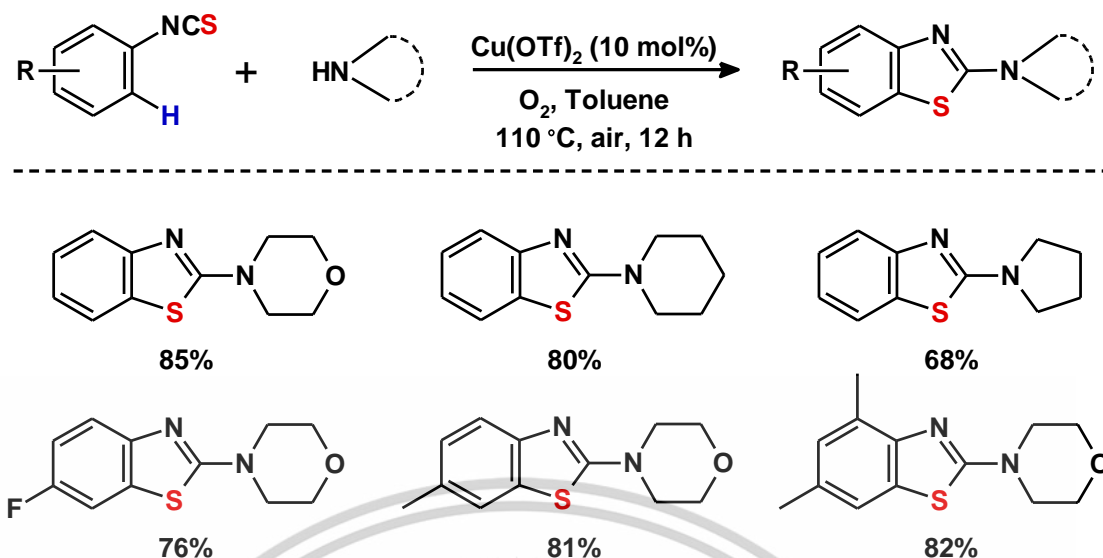
Scheme 2.15 Mechanism for the differential selectivity using palladium catalyst.

In path I, Pd(II) is reduced to Pd(0) in the presence of a base. The Pd(0) then undergoes oxidative insertion into the halo group of thiourea followed by coordination

with sulfur to generate intermediate (I). Subsequent reductive elimination produces benzothiazoles and regenerates Pd(0) which maintains the catalytic cycle (path I, Scheme 2.15). In path II, for substrates containing 2-fluoro or 2-chloro substituents, precoordination of sulfur to Pd leads to the formation of a palladacycle either via  $\sigma$  bond metathesis generating intermediate (II) or via a base-assisted deprotonative metalation generating intermediate (III). In this pathway, benzothiazole is obtained via the C–H activation pathway with the retention of 2-halo (Cl, F) substituents. The in situ generated Pd(0) gets oxidized to Pd(II) in the presence of air to continue the catalytic cycle. Depending on the nature of the substituents present, they prefer to go either via path I or path II and in some cases both paths compete with each other giving a mixture of products. In contrast, the Cu catalyzed reaction involves intramolecular C–S cross-coupling of ortho-halothiureas for all halogens (F, Cl, Br, and I) and proceeds through an oxidative insertion/reductive elimination mechanism via a Cu(I)/Cu(III) cycle.

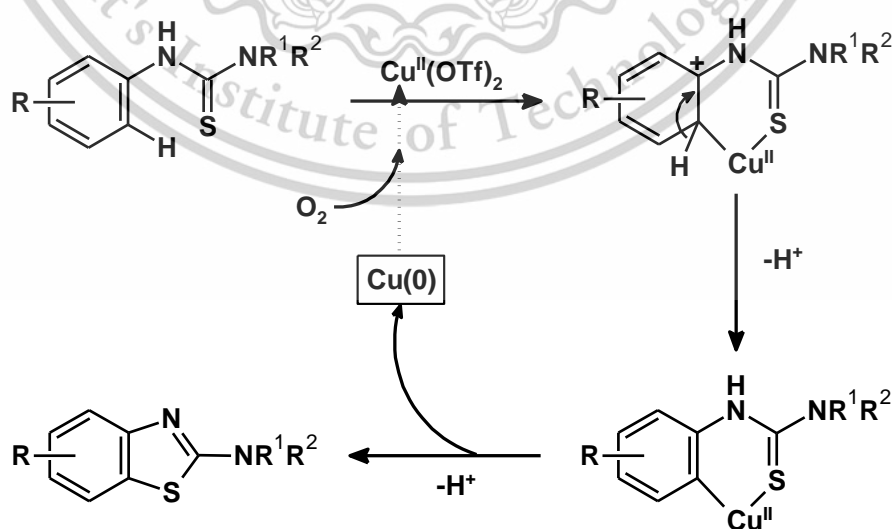
From the regioselective intramolecular C–S bond formation during the formation of 2-aminobenzothiazole from 2-halo substituted thioureas using Cu and Pd catalyst. Palladium prefers the C–H activation pathway over dehalogenative for less reactive halogens, such as fluoro. However, no satisfactory explanation for this selectivity emerged from the study. For bromo and iodo substituents prefer the dehalogenation pathway while chloro substituted thioureas follow either pathway, resulting in both types of benzothiazoles. In contrast, Cu favors the dehalogenation pathway for all halogens.

In subsequent research, Patel and co-workers presented an efficient approach for synthesizing 2-aminobenzothiazoles from aryl isothiocyanates via Cu(OTf)<sub>2</sub>-catalyzed intramolecular C–H functionalization/C–S bond formation (Scheme 2.16) [40]. Using 10 mol% of Cu(OTf)<sub>2</sub> in toluene and under 1 atm of O<sub>2</sub> at 110 °C, both electron-poor and -rich substrates were successfully converted into the desired products.



Scheme 2.16 The production of 2-aminobenzothiazoles from aryl isothiocyanates by copper catalyst.

This research is consistent with the findings of Nagasawa et al. [40-42]. These findings indirectly support the oxidative cyclization mechanism where copper triflate is initially coordinated with the sulfur atom leading to a directed ortho-metalation via an electrophilic aromatic substitution pathway. This is followed by the formation of a six-membered metallacycle and subsequent reductive elimination to give 2-aminobenzothiazole. The  $\text{Cu}(0)$  species formed in this step is oxidized to  $\text{Cu}(\text{II})$  by molecular oxygen thereby maintaining the catalytic cycle (Scheme 2.17).



Scheme 2.17 Mechanism for copper catalyzed oxidative cyclization of *N*-arylthiourea. This material is reserved for educational use only, not allowed for commercial use.

Forbidden to modify the content, and cite the document when use.

## 2.3 Computational chemistry

Computational chemistry aims to simulate and predict molecular structures and properties using a variety of calculations based on quantum and classical physics. These approaches greatly minimize the time, costs, and resources required for experimental processes. Furthermore, computational chemistry enables the exploration of a broader chemical space, which can result in discovering novel and unexpected molecules.

### 2.3.1 Density Functional Theory (DFT)

Density functional theory (DFT) [43-46] is an approach to the electronic structure of atoms and molecules that has received a lot of attention since the 1980s and 1990s. Hartree-Fock theory is the first attempt to develop density functional theory. In this theory, the multi-electron wavefunction is expressed as a Slater determinant which is made from a set of single-electron wavefunctions. However, density functional theory attempts to calculate all electronic energy and the total electronic density distribution, while Hartree-Fock theory exactly calculates the overall electron wavefunction. The main idea behind density functional theory is a relation between all electronic energy and the total electronic density. And later density functional theory was developed by Hohenberg and Kohn theory and Kohn and Sham theory. Hohenberg and Kohn theory proved that all energy of an electron gas is a characteristic function of the electron density. The ground state energy of the system and the density are the minimum of the all energy functional which is indeed the indeed single-particle density of the ground state. Kohn and Sham theory presented that can replace them any electron problem by an equivalent set of self-consistent single-particle equations, can called Kohn-Sham (KS) equations. The Kohn-Sham overall energy functional is

$$E[\Psi_i] = 2 \sum_i \int \Psi_i \left( -\frac{\hbar^2}{2m} \right) \nabla^2 \Psi_i d^3r + \int V^{ion}(r) n(r) dr + \frac{e^2}{2} \int \frac{n(r)n(r')}{|r-r'|} dr dr' + E_{xc}[n(r)] + E_{nn} \quad (2.1)$$

where the  $\Psi_i$  are electron states

$$E_{nn} = \sum_{ij} \frac{Z_i Z_j}{|R_i - R_j|} \quad (2.2)$$

The equation is the Coulomb energy of the nuclei,  $V^{ion}$  is the electron-ion potential,  $n(\mathbf{r})$  is the electron density.

$$n(\mathbf{r}) = 2 \sum_{i=1}^{N_{occupied}} |\psi_i(\mathbf{r})|^2 \quad (2.3)$$

And  $E_{xc}[n(\mathbf{r})]$  is the exchange-correlation functional. In (Equation 2.3), factor 2 occurs due to there being contributions from up spin and down spin. Only the minimum of the energy functional is the ground state energy of the system that has a physical meaning. At the minimum of the energy functional, the electronic states  $\psi_i$  are self-consistent solutions of the Kohn-Sham equation.

$$H_{KS}\psi_i(\mathbf{r}) = E_i\psi_i(\mathbf{r}), \quad H_{KS} = -\frac{\hbar^2}{2m}\nabla^2 + V^{KS}[n(\mathbf{r})] \quad (2.4)$$

with

$$V^{KS} = V^{ion}(\mathbf{r}) + V^H(\mathbf{r}) + V^{XC}(\mathbf{r}) \quad (2.5)$$

Here  $E_i$  is the Kohn-Sham eigenvalue and  $V^H$  is the Hartree potential of the electrons, defined as follows

$$V^H(\mathbf{r}) = e^2 \int \frac{n(\mathbf{r}')}{|\mathbf{r} - \mathbf{r}'|} d\mathbf{r}' \quad (2.6)$$

The exchange-correlation functional  $V^{XC}$  is the functional derivative of the exchange-correlation energy.

$$V^{xc}(\mathbf{r}) = \frac{\delta E_{xc}[n(\mathbf{r})]}{\delta[n(\mathbf{r})]} \quad (2.7)$$

The interacting many-electron system is planed by the Kohn-Sham equation onto a system of noninteracting electrons moving into an effective potential. The effective

potential shows the effect of the interactions with the other electrons. The theory would be feasible if the exchange-correlation energy were clearly known. In operation, the exchange-correlation energy must rely on approximate expression. The simplest approximation is the local density approximation (LDA). The exchange-correlation energy of LDA is assumed to be

$$E_{xc}^{LDA} = \int dr \epsilon[n(r)]n(r) \quad (2.8)$$

Where is the exchange-correlation energy per unit volume of a homogeneous electron gas of density.

Once the Kohn-Sham orbitals are determined, the overall energy can be received from the simplified equation (Equation 2.1) as follows

$$E[\Psi_i] = \sum_{i=1}^{N_{occupied}} E_i + \int dr \left( \frac{1}{2} V^H(r) + V^{xc}(r) \right) n(r) + E_{xc}[n] + E_{nn} \quad (2.9)$$

The pseudopotential idea is used to simplify the treatment of a many-electron system. By dividing the electrons of the atoms into core electrons and valence electrons. Then the core electrons are assumed to display only a passive role and the terms of pseudopotentials can be described the ion valence electron interaction. The pseudopotential idea removes the core electrons and replaces the strong ionic potential by a weaker “pseudopotential”. The famous form of pseudopotential is the Kleinman and Bylander form.

$$V^{ion}(r) = V^{ps,local}(r) + \sum_l \sum_{m=-1}^l \frac{\phi_{lm}(r) \Delta w_l(r) \Delta w_l(r') \phi_{lm}(r')}{\int dr \phi_{lm}(r) \Delta w_l(r) \phi_{lm}(r)} \quad (2.10)$$

Where  $\Delta w_l(r) = \Delta w_l(r) - V^{ps,local}(r)$ . The function  $w_l$ ,  $V^{ps,local}(r)$ , and  $\phi_{lm}$  are determined by solving the Schrodinger equation, projecting out the core state, and receiving a potential for the valence state. The scattering properties of potential should be conserved and this potential could be transferable led to it should exactly describe the valence electrons in different chemical environments.

Figure 2.2 Flowchart of density functional theory (DFT) calculation. shows the flowchart of the self-consistent calculation of the Kohn-Sham states  $\psi_i$ . The sum of the atomic densities is the initial density  $n_0(\mathbf{r})$ . The Kohn-Sham equation is then solved self-consistently. When some convergence criterion is reached, the self-consistency cycle is stopped. The two most ordinary criteria depend on the difference in the total energies or densities at repetitions  $i$  and  $i-1$ , i.e., the cycle is stopped when  $|E_i - E_{i-1}| < \eta$  or  $\int d\mathbf{r} |n_i(\mathbf{r}) - n_{i-1}(\mathbf{r})| < \eta$ , where  $E_i$  and  $n_i$  are the overall energy and density at repetition  $i$  and  $\eta$  is a determination tolerance parameter. If the self-consistency criteria are not satisfied, then one continues to repeat. In principle, the starting density in the new cycle would be the density obtained in the prior step. In solving the nonlinear Kohn-Sham equations which led to instabilities. This problem has been avoided by various density-mixing schemes. The commonly used pattern is linear mixing, when the two prior repetitions were proposed, the new density is a linear combination of the densities.

$$n_{i+1} = \alpha n_i + (1 - \alpha) n_{i-1} \quad (2.11)$$

Where  $n_i$  is obtained from (Equation 2.3).

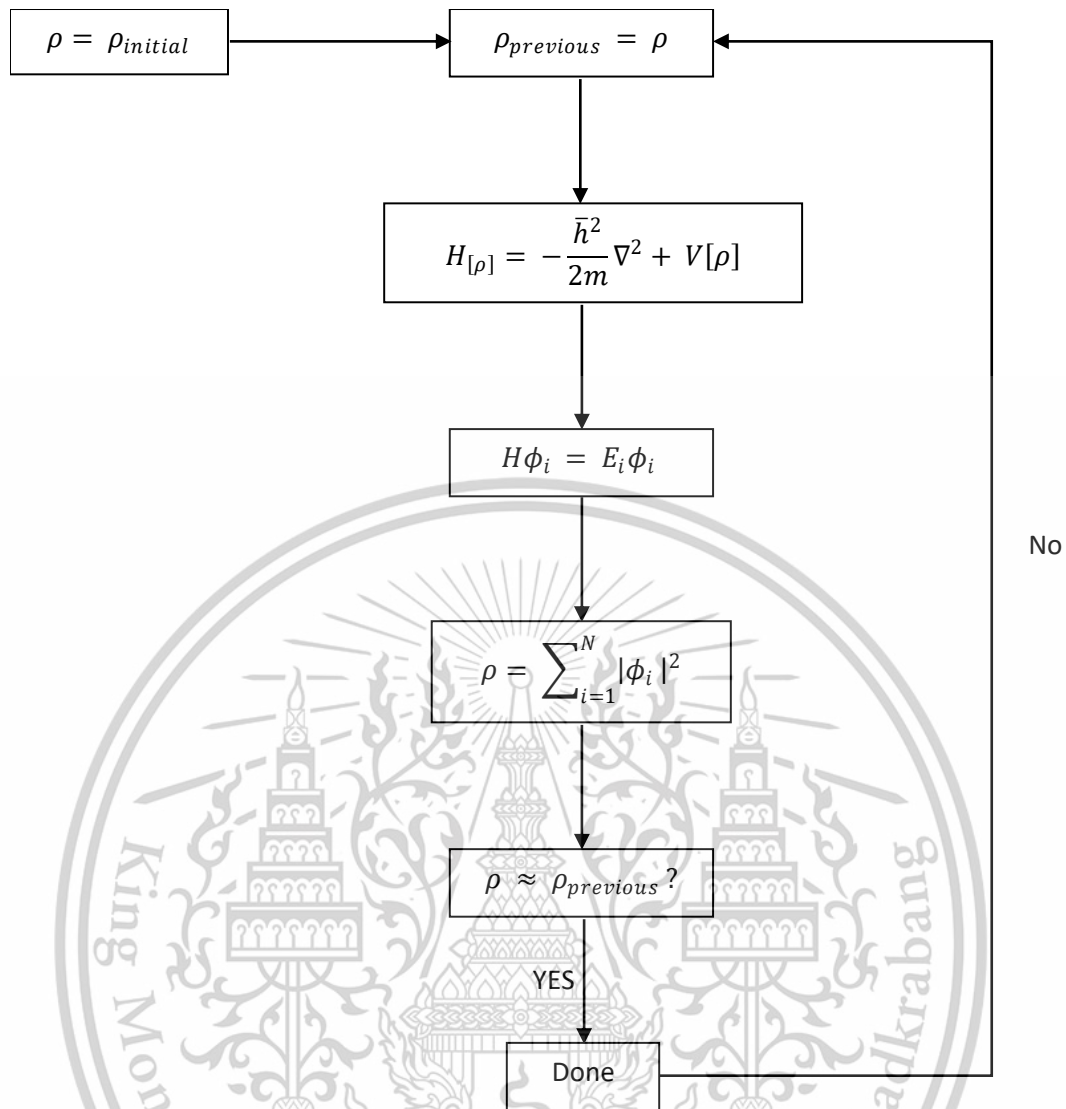


Figure 2.2 Flowchart of density functional theory (DFT) calculation.

### 2.3.2 Basis sets

The basis sets [44-46] most normally used in quantum mechanical calculations are composed of atomic functions. The Slater type orbitals are a clear alternative. Unfortunately, Slater functions are not especially responsible for implementation in molecular orbital calculations. The reason is because some of the integrals are difficult to evaluate, particularly when the atomic orbitals are centered on different nuclei. It is relatively straight-forward to calculate integrals involving one or two centers. Three- and four-centre integrals are also plausible with Slater functions if the atomic orbitals are located on the same atom. But if the atomic orbitals are based upon different atoms, three- and four-centre integrals are very difficult to calculate. The Slater orbitals

are replaced by ab initio calculations with functions based upon Gaussians. The Gaussian function has the form  $\exp(\alpha r^2)$  and the basis functions are used in ab initio calculations consisting of integral powers of  $x$ ,  $y$  and  $z$  multiplied by  $\exp(\alpha r^2)$ .

$$x^a y^b z^c \exp(-\alpha r^2) \quad (2.12)$$

$\alpha$  defines the radial extent (or spread) of a Gaussian function and a function with a small value of  $\alpha$  provides a large spread. The powers of the Cartesian variables can determine the order of these Gaussian functions such as a zeroth-order function with  $a + b + c = 0$ , a first-order function with  $a + b + c = 1$ , etc. Therefore, there is one zeroth-order function, three first-order functions and six second-order functions. The idea of using Gaussian functions in quantum mechanical calculations is frequently cited to Boys [47]. A major strength of Gaussian functions is that the product of two Gaussians can be expressed as a single Gaussian, placed along the line joining the centers of the two Gaussians  $m$  and  $n$ .

$$\exp(-\alpha_m r_m^2) \exp(-\alpha_n r_n^2) = \exp\left(-\frac{\alpha_m \alpha_n}{\alpha_m + \alpha_n} r_{mn}^2\right) \exp(-\alpha r_c^2) \quad (2.13)$$

$r_{mn}$  is the distance between the centers  $m$  and  $n$ , and the orbital exponent  $\alpha$  of the combined function is related to the exponents  $\alpha_m$  and  $\alpha_n$  by

$$\alpha = \alpha_m + \alpha_n \quad (2.14)$$

$r_c$  is the distance from point C, which has coordinates.

$$x_c = \frac{\alpha_m x_m + \alpha_n x_n}{\alpha_m + \alpha_n}; \quad y_c = \frac{\alpha_m y_m + \alpha_n y_n}{\alpha_m + \alpha_n}; \quad z_c = \frac{\alpha_m z_m + \alpha_n z_n}{\alpha_m + \alpha_n} \quad (2.15)$$

$x_m, y_m, z_m$  and  $x_n, y_n, z_n$  are the centers of the two original Gaussians  $m$  and  $n$  respectively.

Consequently, in a two-electron integral of the form  $(\mu\nu|\lambda\sigma)$ , the product  $\phi_\mu(1)\phi_\nu(1)$  can be replaced by a single Gaussian function that is centered at the suitable point C. For Cartesian Gaussian calculation is more complicated than the

example have been mentioned above due to the presence of the Cartesian functions. However, efficient methods for performing the integrals have been invented.

Quantum chemists have devised efficient short-hand notation schemes to denote the basis set used in an ab initio calculation, although this does mean that a proliferation of abbreviations and acronyms is introduced. However, the codes are usually quite simple to understand.

A minimal basis set is a type of representation that includes only the number of functions necessary to describe all the occupied orbitals of an atom. In practical terms, this means that for each atom, the basis set contains the atomic orbitals in its corresponding shell. For instance, hydrogen and helium require a single *s*-type function while elements from lithium to neon use the *1s*, *2s*, and *2p* functions, and so on. The STO-3G, STO-4G, and other STO-*n*G basis sets are examples of minimal basis sets where each orbital is approximated using *n* Gaussian functions. It is found that at least three Gaussian functions are required to properly represent each Slater type orbital and so the STO-3G basis set is the absolute minimum that should be used in an ab initio molecular orbital calculation. In fact, there is often little difference between the results obtained with the STO-3G basis set and the larger minimal basis sets with more Gaussian functions, although for hydrogen-bonded complexes STO-4G can perform significantly better. The STO-3G basis set does perform remarkably well in predicting molecular geometries, though this is due in part to a fortuitous cancellation of errors. Of course, the computational effort increases with the number of functions in the Gaussian expansion.

The use of polarization basis functions is indicated by an asterisk (\*). Thus, 6-31G\* refers to a 6-31G basis set with polarization functions on the heavy atoms. Two asterisks (6-31G\*\*) indicate the use of polarization (*p*) functions on hydrogen and helium. The 6-31G\*\* basis set is particularly useful where hydrogen acts as a bridging atom. Partial polarization basis sets have also been developed. For example, the 3-21G<sup>(\*)</sup> basis set has the same set of Gaussians as the 3-21G basis set supplemented by six *d*-type Gaussians for the second-row elements. This basis set therefore attempts to account for *d*-orbital effects in molecules containing second-row elements. There are no special polarization functions on first-row elements, which are described by the 3-21G basis set.

A limitation of minimal basis sets is their inability to effectively describe species such as anions or molecules with lone pairs which have a significant electron density distributed farther from the nuclear centers. This issue arises because Gaussian basis functions have relatively low amplitudes at distances far from the nuclear centers. To address this, highly diffuse functions can be added to the basis set which improves its capacity to represent the electron density farther away. Such basis sets are indicated by a "+" thus the 3-21+G basis set includes an additional set of diffuse *s*- and *p*-type Gaussian functions for heavy atoms. The notation "++" is used, it indicates that diffuse functions are also included for hydrogen atoms in addition to heavy atoms. At these levels the terminology starts to become a little unwieldy. For example, the 6-311++G(3*df*, 3*pd*) basis set uses a single zeta core and triple zeta valence representation with additional diffuse functions on all atoms. The (3*df*, 3*pd*) indicates three sets of *d* functions and one set of *f* functions for first-row atoms and three sets of *p* functions and one set of *d* functions for hydrogen. This latter convention is probably the most generic. One commonly encountered example is the 6-31G(*d*) basis set, which is synonymous with 6-31G\*.

The basis sets have been considered thus far are sufficient for most calculations. However, for some high-level calculations, a basis set that effectively enables the basis set limit to be achieved is required. The even-tempered basis set is designed to achieve this which each function in this basis set is the product of a spherical harmonic and a Gaussian function multiplied by a power of the distance from the origin.

$$x_{klm}(\rho, \theta, \phi) = \exp(-\zeta_k^2) r^k Y_{lm}(\theta, \phi) \quad (2.16)$$

The orbital exponent is  $\zeta_k$  expressed as a function of two parameters  $\alpha$  and  $\beta$  as follows

$$\zeta_k = \alpha \beta^k \quad k = 1, 2, 3, \dots, N \quad (2.17)$$

The even-tempered basis set consists of the following sequence of functions: 1*s*, 2*p*, 3*d*, 4*f*,..., which correspond to increasing values of *k*. The advantage of this basis set is that it is relatively easy to optimize the exponents for a large sequence of basis functions.

This material is reserved for educational use only, not allowed for commercial use.

Forbidden to modify the content, and cite the document when use.

### 2.3.3 Restricted and unrestricted configurations

The derivation of Hartree-Fock equations was performed for a special case of a closed shell systems. In a closed-shell configuration, each molecular orbital (MO) is occupied by two electrons with opposite spins. Consequently, the total spin of the system, which is the (vector) sum of all electron spins, is zero [48].

$$\hat{S} = \sum_{i=1}^N S_i(i) = 0 \quad (2.18)$$

This is referred to as a singlet or spin singlet because the multiplicity is defined as the number of possible orientations of the total spin, which is

$$\text{multiplicity} = 2S + 1 \quad (2.19)$$

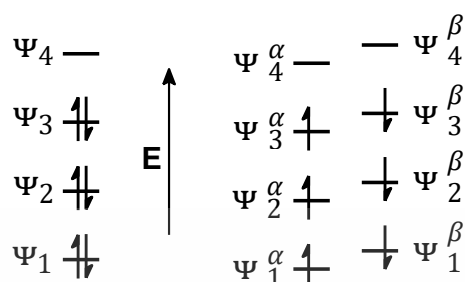
is one for  $S = 0$ .

The  $S$  is the spin quantum number and can take half integer and integer values, i.e.  $S=0, 1/2, 1, 3/2, 2$  etc. The quantum numbers  $S$  come from the allowed values of the total spin operator  $\hat{S}^2$  which are  $S(S+1)$  in the units of  $\hbar$  (but in atomic units this is 1). Therefore, the square of the total spin is  $S(S+1)$ , where  $S$  is the quantum number (not  $S^2$ ). By contrast, open shell systems are those where all electrons are not paired. For example, a radical or atom with a single unpaired electron is a doublet, because  $S = 1/2$  and  $2S + 1 = 2$ . An atom or a molecule with two electrons with the same spin is a triplet, because  $S = 1$ , therefore  $2S + 1 = 3$ .

**Table 2.1** the value of  $S^2$  is calculated and compared to  $S(S+1)$ .

spin quantum number $S$	multiplicity $2S+1$	total spin $S^2 = S(S+1)$
0	1 (singlet)	0
1/2	2 (doublet)	0.75
1	3 (triplet)	2
3/2	4 (quartet)	3.75
2	5 (quintet)	6

There are two ways to describe the electron configurations in open shell systems, restricted and unrestricted.



**Figure 2.3** Spin restricted configurations require both alpha ( $\alpha$ ) and beta ( $\beta$ ) spins to occupy the same spatial orbitals (left). For spin unrestricted configurations allow each spin (alpha ( $\alpha$ ) or beta ( $\beta$ )) to occupy different spatial orbital (right).

### 2.3.3.1 Restricted configurations

Restricted open shell wavefunctions have a well-defined value of the total spin ( $S=0, 1/2, 1$  etc. which correspond to singlet, doublet, triplet etc.). In quantum mechanics, these are eigenfunctions of the total spin operator  $\hat{S}^2$ . However, in certain cases, the wavefunction with the appropriate spin and antisymmetric cannot be accurately represented as a single Slater determinant.

An illustrative example is an open-shell singlet, exemplified by the singlet state of the oxygen molecule  $^1O_2$ , the appropriate singlet wavefunction is

$$\Psi(1,2) = \frac{1}{2}[\Psi_1(1)\Psi_2(2) + \Psi_2(1)\Psi_1(2)][\alpha(1)\beta(2) - \alpha(2)\beta(1)] \quad (2.20)$$

This function cannot be expressed as a single determinant but is represented as a combination of two determinants.

$$\Psi(1,2) = \frac{1}{\sqrt{2}} \left[ \frac{1}{\sqrt{2}} \det \begin{pmatrix} \Psi_1(1)\alpha(1) & \Psi_2(1)\beta(1) \\ \Psi_1(2)\alpha(2) & \Psi_2(2)\beta(2) \end{pmatrix} + \frac{1}{\sqrt{2}} \det \begin{pmatrix} \Psi_1(1)\beta(1) & \Psi_2(1)\alpha(1) \\ \Psi_1(2)\beta(2) & \Psi_2(2)\alpha(2) \end{pmatrix} \right] \quad (2.21)$$

The spin polarization is not considered which arises from the electrons with the same spin interact differently than those with opposite spins.

This material is reserved for educational use only, not allowed for commercial use.

Forbidden to modify the content, and cite the document when use.

### 2.3.3.2 Unrestricted configurations

Unrestricted wavefunctions permit different spatial distributions for electrons with  $\alpha$  spins and  $\beta$  spins, allowing for the description of spin polarization. Spin polarization arises from exchange-correlation effects due to the interactions of electrons with the same spin, particularly in systems with unpaired electrons, such as radicals. However, unrestricted wavefunctions do not possess a well-defined value of spin, meaning they are not eigenfunctions of  $\hat{S}^2$ . They suffer from the spin contamination by states with higher spin. For example, singlet states may exhibit contamination from triplet and quintet states, while doublets may be contaminated by quartets and sextets.

### 2.3.4 Spin density and spin contamination

#### 2.3.4.1 Spin density [49-50]

Electrons within an atom are described quantum-mechanically by their wavefunctions,  $\Psi(\mathbf{r})$ , which are determined by four quantum numbers consisting of  $n$ ,  $\ell$ ,  $m_\ell$ , and  $m_s$ . The probability of locating an electron at position  $\mathbf{r}$  within a small volume  $d\mathbf{r}$  is represented by the electron probability density or also known as electron density.

$$\rho(\mathbf{r}) = |\Psi(\mathbf{r})|^2 d\mathbf{r} \quad (2.22)$$

The two values of the spin quantum number,  $m_s$  ( $\pm 1/2$ ), correspond to two possible spin states, leading to the decomposition of the non-relativistic wavefunction,  $\Psi(\mathbf{r})$ , into two orthonormal functions,  $\Psi_\alpha(\mathbf{r})$  and  $\Psi_\beta(\mathbf{r})$ . The  $\alpha$  state is called "spin up" while the  $\beta$  state is called "spin down." The electronic probability density for all electrons in the  $\alpha$  state is represented as

$$\rho_\alpha(\mathbf{r}) = \sum_1^{N_\alpha} |\Psi_\alpha(\mathbf{r})|^2 \quad (2.23)$$

Where  $N_\alpha$  is the total number of  $\alpha$  electrons. Similarly, the probability density for all  $\beta$  electrons is expressed as

$$\rho_\beta(\mathbf{r}) = \sum_1^{N_\beta} |\Psi_\beta(\mathbf{r})|^2 \quad (2.24)$$

The total electronic probability density can thus be expressed as

$$\rho(r) = \rho_{\alpha}(r) + \rho_{\beta}(r) \quad (2.25)$$

These electron densities are commonly visualized as isodensity surfaces or isosurfaces. An isosurface is a three-dimensional representation of all points where a particular function (in this case,  $\rho(r)$ ) equals a specified value, known as the isovalue.

Electron density isosurfaces are valuable for examining various molecular systems. However, in cases where an unpaired electron is displayed, it is often more insightful to calculate spin density, which is defined as the difference between the  $\alpha$  electron density and the  $\beta$  electron density.

$$\rho_s(r) = \rho_{\alpha}(r) - \rho_{\beta}(r) \quad (2.26)$$

Electronic spin density is positive in regions where an electron is more likely to occupy the  $\alpha$  spin state and negative in regions where an electron is more likely to occupy the  $\beta$  spin state. Experimentally, electronic spin density is measured using electron paramagnetic resonance (EPR). Computationally, it is visualized through an isosurface, similar to the representation used for the total electron density.

In calculating the spin density, one issue that must be taken into account is spin contamination. In unrestricted self-consistent field (SCF) calculations, the alpha and beta electrons and their corresponding orbitals are computed separately. As a result, the wavefunction is no longer considered an eigenfunction of the total spin,  $\langle S^2 \rangle$ , which introduces errors into the calculation. This error, referred to as spin contamination, indicates that a given wavefunction appears to be in a given spin state but is actually mixed with a different spin state. High levels of spin contamination can impact the total energy, geometry, population analysis, and spin density of the system.

#### 2.3.4.2 Spin contamination [51-53]

Introductory explanations of Hartree-Fock calculations (generally employing Rootaan's Self Consistent Field (SCF) approach) typically concentrate on singlet systems where all electron spins are coupled. The computation can be performed with relative ease when assuming the calculations are restricted to two electrons

occupying each orbital. This is commonly termed a spin restricted Hartree-Fock (RHF) calculation. For systems exhibiting a multiplicity other than one, the RHF method cannot be directly applied. Instead, an unrestricted self-consistent field (UHF) calculation is typically employed. In this approach, two separate sets of orbitals are established, one for the alpha electrons and another for the beta electrons. Generally, both sets of orbitals utilize the same basis functions but feature distinct molecular orbital coefficients. The benefit of unrestricted calculations is their ability to be executed with high efficiency. However, the disadvantage is that the wave function is no longer an eigenfunction of the total spin,  $\langle S^2 \rangle$ , which may introduce certain errors into the calculation. This issue is known as spin contamination.

Spin contamination leads to wave functions that appear to be the intended spin state but actually contain a mixture of other spin states. This can occasionally cause the computed total energy to decrease slightly due to increased variational flexibility. It more commonly causes a slight increase in the total energy as a higher energy state is introduced into the mix. However, this variation is an artifact of an incorrect wavefunction. Since the error is not systematic, the energy difference between states will be negatively impacted. High levels of spin contamination can impact the geometry, population analysis and notably distort the spin density.

Most ab initio programs provide the expectation value of the total spin,  $\langle S^2 \rangle$ , to detect spin contamination. In the absence of spin contamination, this value should equal  $S(S+1)$  where  $S$  is 1/2 times the number of unpaired electrons. Spin contamination is considered negligible if the value of  $\langle S^2 \rangle$  differs from  $S(S+1)$  by less than 10%. Spin contamination frequently occurs in unrestricted Hartree-Fock (UHF) calculations as well as in unrestricted Møller-Plesset (UMP2, UMP3, UMP4) calculations. In contrast, significant spin contamination is less commonly observed in density functional theory (DFT) calculations, even when employing unrestricted Kohn-Sham orbitals. Unrestricted calculations often incorporate a spin annihilation step which eliminates a significant portion of the spin contamination from the wavefunction during the calculation process. This approach aids in reducing spin contamination, but it does not entirely eliminate it. The final value of  $\langle S^2 \rangle$  serves as the most reliable indicator of the level of spin contamination present.

For example, an unrestricted calculation on a CH radical presents a doublet (spin multiplicity of 2), with the total spin  $S^2$  expected to be 0.75.

**Annihilation of the first spin contaminant :**

$S^2$  before annihilation            0.7529,            after            0.7500

The  $\langle S^2 \rangle$  value after the UHF calculation was 0.7529 which is slightly higher than 0.75. This suggests that the wavefunction was influenced by a higher spin, although the contamination was not excessive. Gaussian attempts to correct for the contamination using a method known as spin annihilation. In this instance, the contribution from the higher spin component was completely eliminated, resulting in the accurate spin value of 0.75.

## 2.4 Kinetic isotope effect

The kinetic isotope effect (KIE) displays the substitution of isotope affects the reaction rate. This valuable method for elucidating reaction mechanisms and identifying whether a specific bond is cleaved during the rate-determining step. The KIE is typically assessed by replacing a hydrogen atom in the bond of interest with a deuterium atom. In these instances, the KIE is represented as the ratio of the rate constants,  $k_H/k_D$ . The KIE can be classified in several ways, including as primary or secondary and as normal or inverse. To elucidate the basis of the KIE, attention will be given to the primary KIE where C–H or C–D bond cleavage happens during the rate-determining step.

Examine the homolytic cleavage of C–H and C–D bonds. The activation energy for reaction is determined by the gap between the dissociation energy and the lowest vibrational level which corresponds to the zeroth ( $n = 0$  in Equation 2.27). At 300 K, this lowest energy state accounts for up to 99% of C–H bonds and is referred to as the zero-point energy (ZPE).

$$E_n = \left(n + \frac{1}{2}\right) h\nu \quad \text{where } n = 0, 1, 2, \dots \quad (2.27)$$

The chemical bond can be likened to a spring with masses at both ends, allowing the vibrational frequency of the bond's stretching motion to be calculated using the

classical spring model (Equation 2.28). By combining Equation 2.27 with Equation 2.28, we can establish that the zero-point energy (ZPE) is inversely related to the square root of the reduced mass ( $m_r$ ). Since the  $m_r$  for a C–D bond is higher than that of a C–H bond ( $m_r^{CH} = 1.08$ ,  $m_r^{CD} = 1.71$ ), the ZPE for the C–D bond is lower. This implies that the higher activation energy ( $E_a$ ) for a C–D bond, resulting in a slower dissociation rate that leads to the KIE greater than 1.

$$v = \frac{1}{2\pi} \sqrt{\frac{k}{m_r}} \quad \text{where } m_r = \frac{m_1 m_2}{m_1 + m_2} \quad (2.28)$$

By assuming that the bond is fully broken at the transition state, we can estimate the maximum KIE using Equation 2.29. At 300 K, the KIE for a C–H bond with a vibrational frequency of  $3000 \text{ cm}^{-1}$  is roughly 6.5.

$$\begin{aligned} KIE_{full} &= \frac{k_H}{k_D} = \exp\left(-\frac{E_a^{CH} - E_a^{CD}}{RT}\right) \\ &= \exp\left(-\frac{E_{lim} - ZPE^{CH} - (E_{lim} - ZPE^{CD})}{RT}\right) \\ &= \exp\left(\frac{ZPE^{CH} - ZPE^{CD}}{RT}\right) = \exp\left(\frac{\Delta ZPE_{react}}{RT}\right) \end{aligned} \quad (2.29)$$

Examples of complete bond breakage at the transition state are uncommon and primary kinetic isotope effect (KIE) values are usually below 6.5. In most cases, the bond is only partially cleaved or an alternative bond starts to form concurrently at the transition state. When a bond is not fully dissociated, it exhibits different zero-point energies for the C–H and C–D cases (similar to the ground state) but the bond in the transition state is less robust, resulting in a smaller difference in the ZPE. Although the activation energy remains greater for the deuterated substrate compared to the non-deuterated version, the disparity in activation energies is lower than in cases of full dissociation, leading to lower values of the KIE (Equation 2.30).

$$\begin{aligned} KIE_{part} &= \frac{k_H}{k_D} = \exp\left(-\frac{E_a^{CH} - E_a^{CD}}{RT}\right) \\ &= \exp\left(-\frac{ZPE_{TS}^{CH} - ZPE^{CH} - (ZPE_{TS}^{CD} - ZPE^{CD})}{RT}\right) \\ &= \exp\left(\frac{ZPE^{CH} - ZPE^{CD} - (ZPE_{TS}^{CH} - ZPE_{TS}^{CD})}{RT}\right) \\ &= \exp\left(\frac{\Delta ZPE_{react} - \Delta ZPE_{TS}}{RT}\right) < KIE_{full} \end{aligned} \quad (2.30)$$

This material is reserved for educational use only, not allowed for commercial use.

Forbidden to modify the content, and cite the document when use.

Equation 2.30 facilitates the comparison of experimental KIE with theoretical values by utilizing zero-point energies derived from calculations.

There are three common approaches to measuring the KIE.

1) Performing two separate experiments, one with a substrate containing a C–H bond and another with a substrate containing a C–D bond and then measuring the rate constants for each.

2) Carrying out a competitive experiment involving deuterated and non-deuterated substrates where the KIE is measured based on the relative amounts of products formed from each substrate or by tracking the depletion of the starting materials.

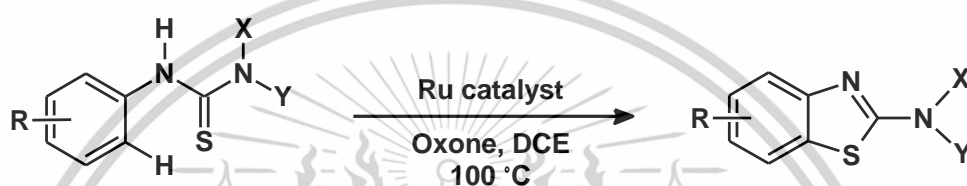
3) Performing an intramolecular competition experiment using a substrate containing both hydrogen and deuterium atoms in equivalent positions. In this scenario, the KIE can also be determined by the relative amounts of product resulting from the functionalization of the C–H or C–D bonds.

These approaches can yield different KIE values for the same reaction, depending on the relation between the rate-determining step (RDS) and the C–H cleavage step. By analyzing the KIE values derived from two or more of these techniques, researchers can gain important insights into the reaction mechanism and the position of the elementary steps relative to one another. For example, if the RDS coincides with the C–H cleavage step, the KIE will be detected in all three experimental approaches. Conversely, if the RDS occurs before the C–H cleavage step and the substrate containing the bond of interest is not engaged in this step, the KIE will only be detected with the second and third methods. This discrepancy arises because the product distribution is determined by the rate differences in C–H bond cleavage, irrespective of whether it is the RDS. In the first method, the reaction rates for both deuterated and non-deuterated substrates will be identical, resulting in no observable KIE. Further details and analysis of other potential reaction scenarios can be found in a recent publication by Simmons and Hartwig [54].

The KIE is an effective and straightforward technique for investigating reaction mechanisms, providing critical information about which bond is cleaved during the reaction and at what stage it occurs [55].

## 2.5 Literature reviews

Sharma et al. [18] reported an efficient approach to the preparation of 2-aminobenzothiazoles. The authors utilized a ruthenium catalyzed intramolecular C–S coupling reaction of *N*-arylthioureas for the synthesis of 2-aminobenzothiazoles that has been developed. They used kinetic, isotope labeling and some limited computational studies to shed light on the catalytic mechanism (Scheme 2.18). They propose an electrophilic ruthenation pathway instead of a direct C–H activation. The scope of the method was also examined for the diverse *N*-arylthioureas.



**Scheme 2.18** Ruthenium catalyzed intramolecular C–S coupling leading to 2-aminobenzothiazole.

The authors performed some limited theoretical calculations using the hybrid DFT based B3LYP functional to provide insights into the reaction mechanism. They replaced the morpholino group with hydrogen for the simplicity of calculation and used *p*-cymene and chlorine (Cl) as ligands in the ruthenium complex within their system. They evaluated three possible intermediates in the proposed mechanism (Figure 2.4). The structure **12** displayed an interaction between Ru and C2 of phenyl ring with a bond distance of 2.47 Å and the hydrogen attached to C2 was distorted from planarity by approximately 17°. Following the reaction mechanism, the corresponding transition state was identified where the hybridization of C2 of phenyl has been changed from  $sp^2$  to a distorted  $sp^3$ , supporting the formation of the structure **13**. The strong interaction between C2 and the electrophilic Ru(II) promotes the breaking of the C–H and Ru–Cl bonds, leading to the formation of **14** and HCl. The energy barrier for this reaction is calculated to be 26.5 kcal/mol. However, the secondary kinetic isotope effect (KIE) suggests that the C–H bond breaking is not the rate-determining step. Instead, it is associated with the change in hybridization state (from  $sp^2$  to  $sp^3$ ) of the arene carbon to which either the proton or deuterium is attached [56].

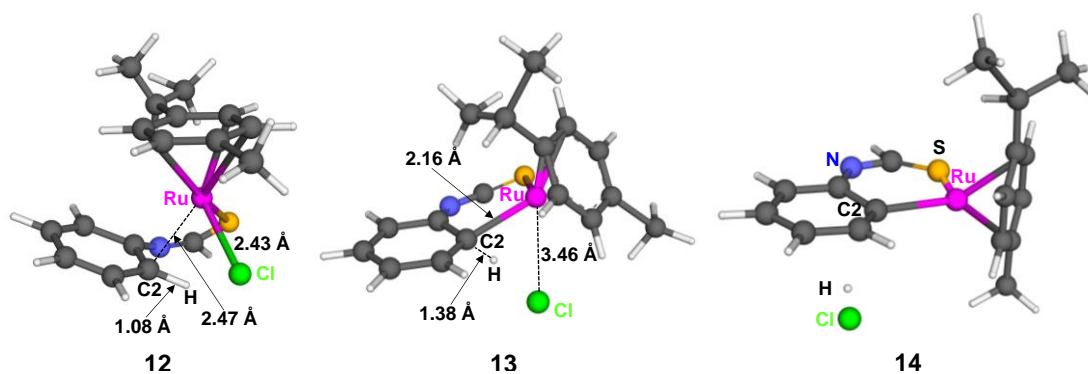


Figure 2.4 Calculated structures of 12, 13, and 14 using DFT method.

The methodology exhibited broad substrate scope and diversity which cover a range of electron-donating and withdrawing groups. Notably, in substrates with an electron-donating substituents, the cationic charge present in the structure **13** on the phenyl ring is effectively stabilized by the presence of the electron-rich group. In contrast, electron-withdrawing substituents on the phenyl ring destabilize the structure **13**, leading to slower reactions. The authors observed that electron-rich *N*-phenylthiourea exhibited a reaction faster than electron-deficient *N*-phenylthiourea. It was proposed that this was influenced by the direct coordination of the substituent with the ruthenium complex (Figure 2.5).

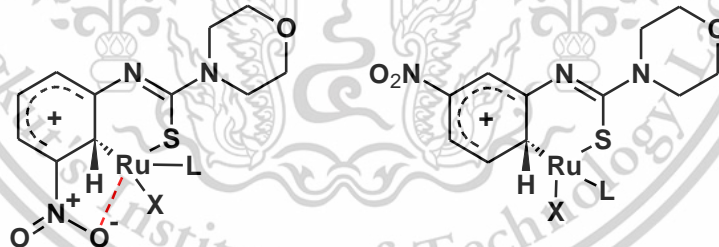


Figure 2.5 Explanation for the rationale behind the regiochemical outcome of  $\text{NO}_2$ -phenylthiourea.

In 2020, Henry et al. [21] explored the iron-catalyzed synthesis of 2-arylbenzoxazoles and 2-arylbenzothiazoles. They developed two distinct methods for these syntheses, utilizing iron(III)-triflimide to activate *N*-bromosuccinimide (NBS). The first method involves the one-pot cyclization of *N*-arylbenzamidates via a regioselective iron(III)-catalyzed bromination reaction, followed by a copper(I)-catalyzed C–O bond

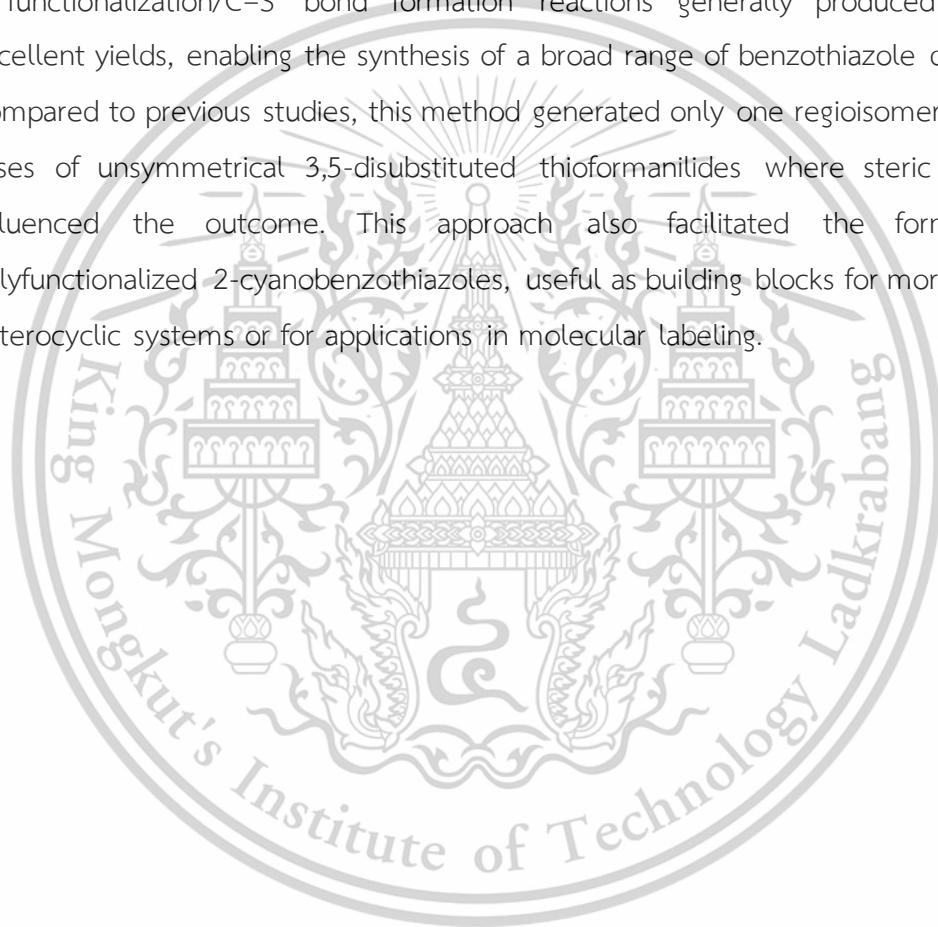
formation. The second method achieves direct cyclization of *N*-arylthiobenzamides through iron(III)-mediated bromination, followed by intramolecular electrophilic aromatic substitution reaction. Both approaches were applied to a wide range of substrates, resulting to the synthesis of a small library of products, including two compounds of pharmaceutical significance. It is notable that the single step C–S bond forming process occurs under milder conditions than typically required for this type of cyclization, resulting in a cleaner generation of the desired compounds.

In 2020, Gao et al. [57] presented an efficient and mild method for the synthesis of 2-substituted benzothiazoles using readily available arylthioureas and NiBr<sub>2</sub> as the catalyst. This approach offers good yields, lower costs, simpler performance, and reduced reaction time. Additionally, the scalability of the reaction without significant loss in yield shows its potential for pharmaceutical and industrial applications. After determining the optimized reaction conditions, the scope of substrates for the synthesis of 2-dimethylamino-benzothiazoles was investigated. A variety of substrates containing electron-withdrawing or electron-donating groups were efficiently and rapidly converted to the desired products. Initially, phenylthioureas with halogen substituents in the *para*-position provided excellent yields (83–86%). However, stronger electron-withdrawing groups, such as nitro and cyano, slightly reduced the yields. On the other hand, substrates with electron-donating groups gave excellent yields (90–94%).

In 2020, Ongagna et al. [58] studied a series of [M(NHC)<sub>2</sub>X<sub>2</sub>] (where M is nd<sup>8</sup> transition metal and X represents halogens Cl, Br and I) were optimized in the gas phase using three different functionals (B3LYP, M06 and B3PW91) and two basis sets. The LanL2DZ basis set was applied to nd<sup>8</sup> transition metals and halogens while 6-311+G(d,p) was used for other atoms. The performance of these methods was compared by examining the bond distances between metal and carbon (C–M) as well as metal and halogen (M–X) atoms. The B3PW91 functional yielded bond distances closest to experimental data. Additionally, the calculated total energies showed that the complexes favored a normal coordination mode for binding. The bond critical point (BCP) analysis suggested that the M–X bonds are more stable than the M–C bonds, and the hybridization of metal cation in C–M and C–X bonds are  $\sim dsp^2$ , with increased *d* character when moves from nickel (Ni) to platinum (Pt). Charge

decomposition analysis (CDA) revealed that Pt-halide complexes had lower  $|d/b|$  ratios due to the relativistic effects that contracts the  $s$  and  $p$  orbitals and diffuse  $d$  and  $f$  orbitals.

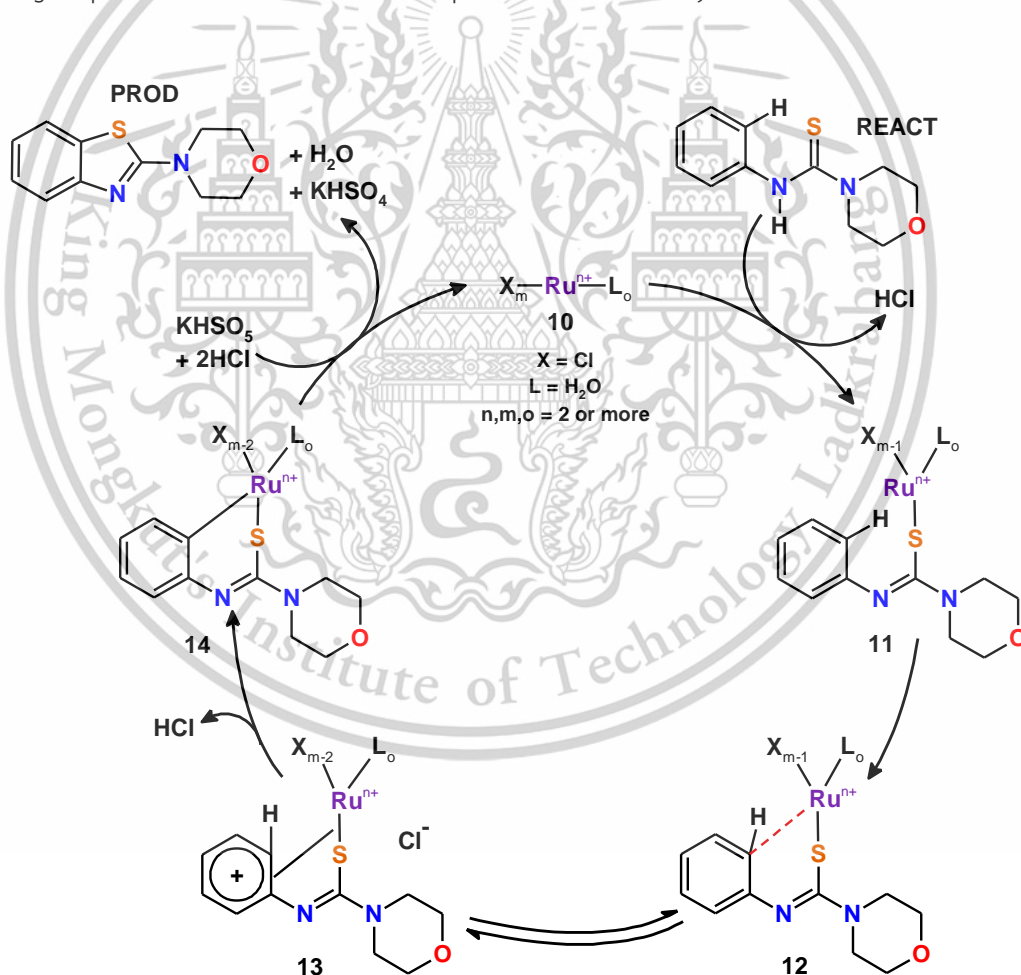
In 2022, Broudic et al. [59] investigated reaction conditions using palladium and copper to successfully cyclize cyanothioformamides into benzothiazoles substituted at various positions, with a versatile carbonitrile group at C2. The presence of 2 equiv of potassium iodide (KI, as an inorganic additive) was found to be essential for better conversion, and air was essential for reoxidizing  $\text{Pd}^0$  at the end of the reaction. The C–H functionalization/C–S bond formation reactions generally produced good to excellent yields, enabling the synthesis of a broad range of benzothiazole derivatives. Compared to previous studies, this method generated only one regioisomer, except in cases of unsymmetrical 3,5-disubstituted thioformanilides where steric hindrance influenced the outcome. This approach also facilitated the formation of polyfunctionalized 2-cyanobenzothiazoles, useful as building blocks for more complex heterocyclic systems or for applications in molecular labeling.



## Chapter 3

### Research methodology

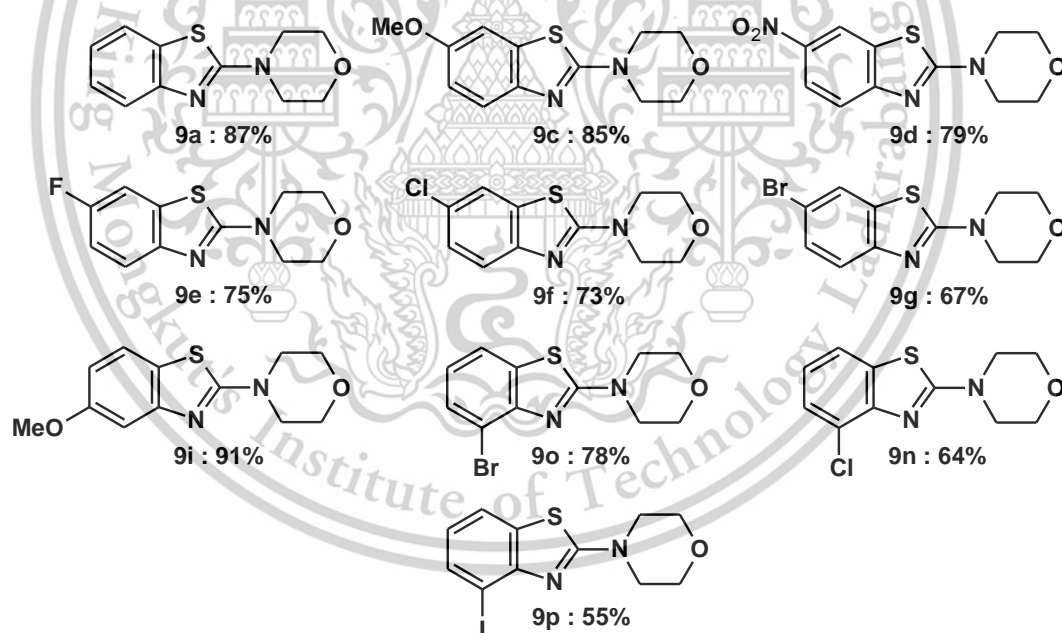
To investigate the mechanistic proposals and obtain insights into the ruthenium-catalyzed formation of 2-aminobenzothiazoles from *N*-arylthioureas, the density functional theory (DFT) method was utilized. A model of the most efficient catalyst identified by Sharma et al. ( $\text{RuCl}_3$ , 89%) [18] was first created to validate the current mechanistic proposal. An octahedral complex [60-62] consisting of  $\text{RuCl}_3$ , *N*-arylthiourea, and three water molecules was generated, consistent with Scheme 3.1. The peroxide oxidizing agent potassium monopersulfate (oxone) was modeled with hydrogen peroxide for reasons of computational efficiency [63-64].



**Scheme 3.1** Proposed mechanism leading to the preparation of 2-aminobenzothiazoles.

The study led to the design of the plausible mechanisms as shown in Scheme 4.1, where Pathway A (blue) had a mechanistic process comparable to that described by Sharma et al. in Scheme 3.1. Pathway B (green) showed a slightly different reaction sequence from Pathway A, and Pathway C (red) represented an alternative route for the generation of benzothiazole products. Additionally, the non-catalyzed reaction involving the substrate, hydrogen peroxide, and water was also examined for comparison.

After obtaining insight into the reaction mechanism, the correlation between the rate-determining barrier and the yields for 10 *N*-arylthioureas was explored to assess the validity of the new mechanistic proposal. As shown in Figure 3.1, 10 *N*-arylthioureas cover a range of electron-donating/neutral (MeO, H) and withdrawing groups (F, Cl, Br, I, and NO<sub>2</sub>) at different positions (*ortho*-, *meta*-, and *para*- positions) of the aryl thioureas. These generate the corresponding products with yields ranging from 55–91%.



**Figure 3.1** The yield for 10 *N*-arylthioureas which cover a range of electron-donating/neutral (MeO, H) and withdrawing groups (F, Cl, Br, I, and NO<sub>2</sub>) at the *ortho*-, *meta*- and *para*- positions of the aryl thioureas.

### Computational details

All calculations were performed using the Gaussian 16 program using the UB3PW91 functional [65], a commonly used method in Ru-based research [58, 66]. Geometry optimizations were carried out using the 6-31+G\*\* basis set for H, N, O, and S atoms and using the LANL2DZ for Ru ( $\Delta E$ ) [24, 67-69]. Single-point energies ( $\Delta E_{sp}$ ) were then calculated using the 6-311++G\*\* basis set for H, N, O, and S atoms, and def2-TZVP for Ru [70-71]. The existence of doublet and quartet spin states (M) was examined since it has been shown that benzothiazole synthesis can follow a free radical process [72-73]. Stationary points displaying spin contamination were excluded (i.e.,  $\langle S^2 \rangle \geq 5\%$  from the expected value).

Stationary points were validated through an analysis of their vibrational frequencies. Transition states exhibited a single vibration with a negative eigenvalue while minima showed only positive values. Free energies ( $\Delta G$ ) were calculated using the zero-point energies and thermal corrections were calculated at 298.15 K.

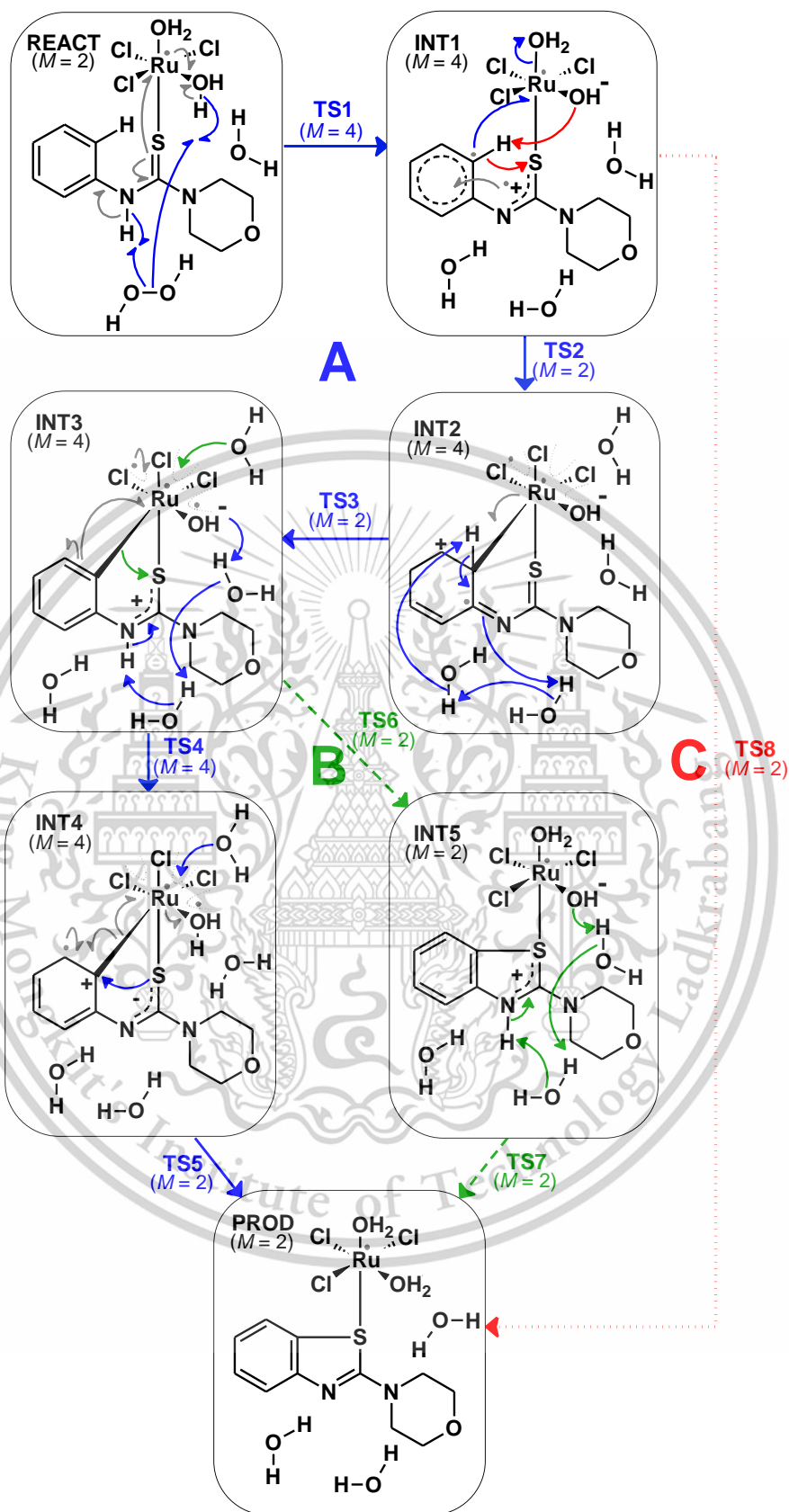
The Discovery Studio 2019 Client program (DSV) was used to create 3D structure analysis of stationary points and all 2D structures were drawn by the ChemSketch program.

## Chapter 4

# Results and discussion

The DFT computational method was used to shed further light on the mechanistic proposals associated with the ruthenium catalyzed formation of 2-aminobenzothiazoles from *N*-arylthioureas. The calculation results display three possible mechanistic routes (Pathway A, B and C). The chemical structures of stationary points obtained on three mechanistic pathways leading to 2-aminobenzothiazole are illustrated in Scheme 4.1. The corresponding energies are given in Table 4.1. The reliability of calculated energy values was verified by the strong correlation between the  $\Delta E$ ,  $\Delta E_{sp}$  and  $\Delta G$  values with  $R^2$  being 0.99 as shown in Figure S1, only the  $\Delta E$  values will be referenced henceforth. The energy profile of optimized structures is shown in Figure 4.1.

In Scheme 4.1, the key changes in charge and spin density are described throughout the chemical reaction. The use of single headed (homolytic) and double headed (heterolytic) arrows clarifies the complex alterations in bonding and the electron movement within the system. Ruthenium remains in the  $d^5$  (+3 oxidation state) throughout the reaction, however significant charge transfer occurs onto the different positions, including the *N*-arylthiourea atoms, the peroxide while the O–O bond breaks, or its coordinating ligands ( $H_2O$  and  $Cl$ ). The required reactions involve H atom or  $H^+$  proton transfers and oxidative electron transfers occur in a concerted system via different centers, which can be considered through proton coupled electron transfer (PCET) processes [72-73]. The movement of bonding electrons in Scheme 4.1 are colored to represent the three distinct reaction pathways that have been identified, while any internal electron transfers are indicated using gray arrows.



**Scheme 4.1** Illustration of the discrete steps involved in the production of 2-aminobenzothiazole from *N*-arylthiourea.

This material is reserved for educational use only, not allowed for commercial use.

Forbidden to modify the content, and cite the document when use.

**Table 4.1** The computed  $\Delta E$  and  $\Delta G$  energies of stationary points using the UB3PW91/6-31+G\*\*/LANL2DZ level. The  $\Delta E_{sp}$  correspond to the single point energy of stationary points using the UB3PW91/6-311++G\*\*/def2-TZVP level. Energies are reported in kcal/mol and relative to the reactant. Absolute barriers heights are in parenthesis.

ID	M	$\Delta E$	$\Delta G$	$\Delta E_{sp}$
REACT	2	0.0	0.0	0.0
TS1	4	16.2	10.0	10.4
INT1	4	-33.1	-34.5	-39.7
TS2	2	9.1 (42.2)	6.6 (41.1)	3.9 (43.6)
INT2	4	-18.5	-21.6	-25.1
TS3	2	-7.0 (11.5)	-9.5 (12.1)	-13.8 (11.4)
INT3	4	-24.9	-29.5	-34.9
TS4	4	-12.6 (12.3)	-20.3 (9.2)	-20.9 (14.0)
INT4	4	-25.3	-29.7	-32.2
TS5	2	-22.8 (2.5)	-25.8 (4.0)	-28.4 (3.8)
TS6	2	-14.1 (10.8)	-16.9 (12.6)	-21.4 (13.5)
INT5	2	-75.9	-71.2	-77.4
TS7	2	-71.9 (3.9)	-70.4 (0.8)	-72.4 (5.0)
TS8	2	-25.4 (7.7)	-26.7 (7.9)	-32.4 (7.3)
PROD	2	-77.2	-75.5	-79.3

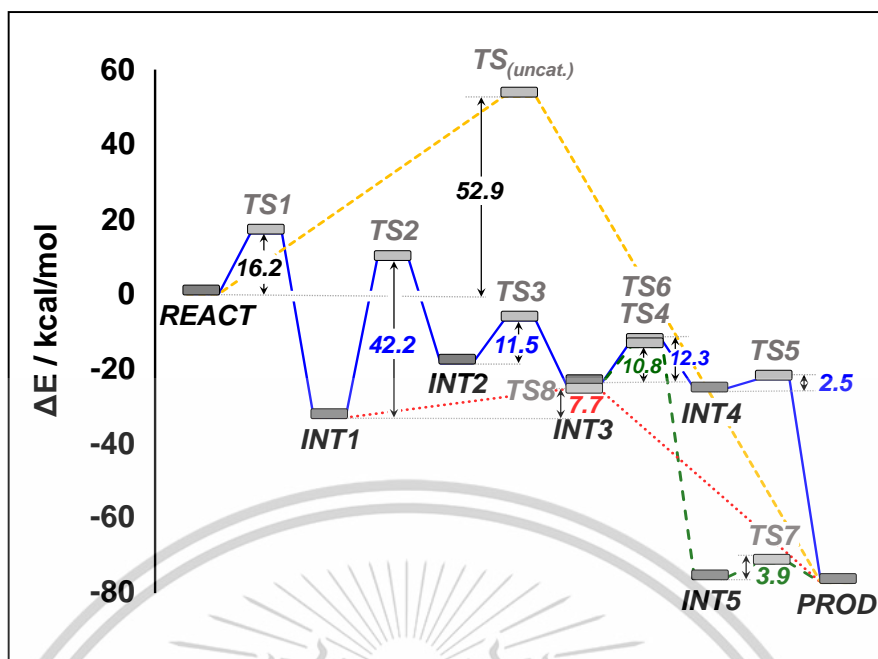


Figure 4.1 Computed reaction energy profile corresponding to the production of 2-aminobenzothiazole from *N*-arylthiourea.

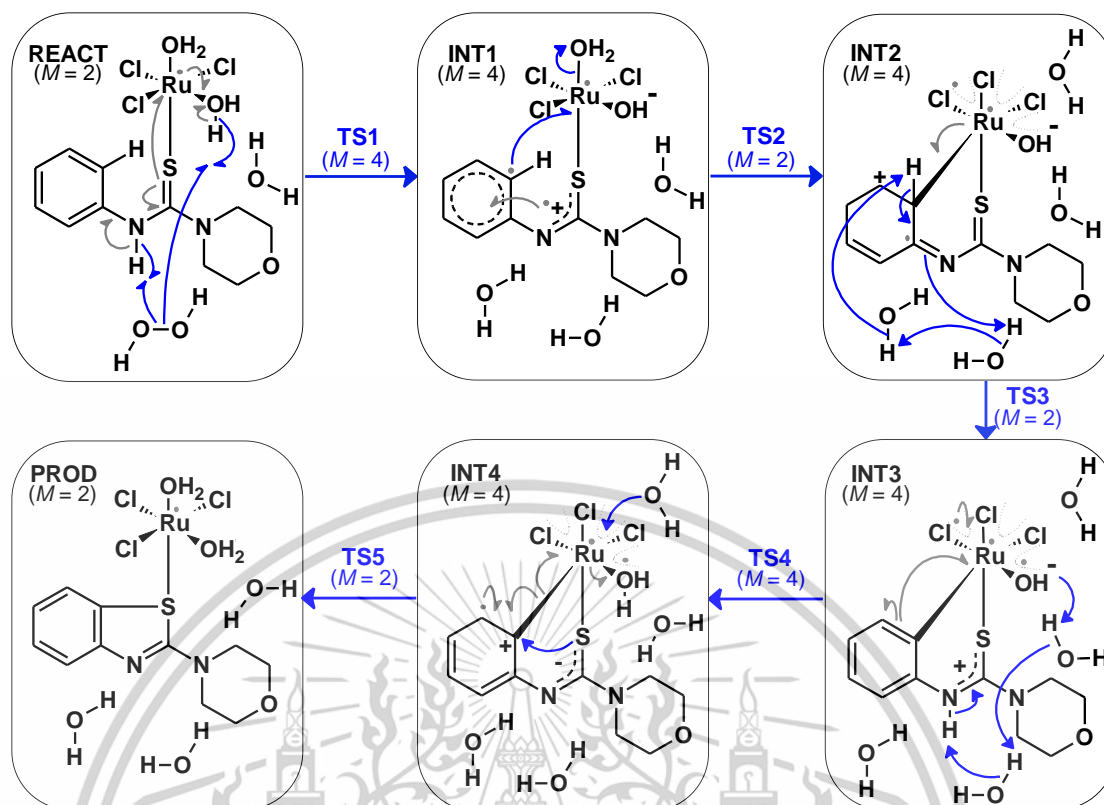
The mechanism for all three pathways initiates with **REACT**. The calculated structure (**REACT**) consists of an octahedral ruthenium complex formed by *N*-arylthiourea and  $\text{Ru}^{\text{III}}\text{Cl}_3(\text{H}_2\text{O})_2$ . This resulting intermediate (**REACT**) displays Ru-S distance of 2.39 Å, while the Ru-Cl and Ru-O distances are found to be  $\sim 2.3$  Å and  $\sim 2.2$  Å, respectively. The stationary point proceeds via a doublet spin state with the radical located on the ruthenium atom (Figure S2). Hydrogen peroxide ( $\text{H}_2\text{O}_2$ ) is also added in the starting model and a third water molecule, which was a ligand of the ruthenium complex, has been displaced by the *N*-arylthiourea on its association with ruthenium. Further investigation revealed that the difference in energy between the Ru-water complex and the Ru-*N*-arylthiourea complex is 3.4 kcal/mol in favor of the former.

#### 4.1 Pathway A

Mechanistic pathway A in Scheme 4.2, which has a mechanistic process equivalent to that described by Sharma et al in Scheme 3.1, is performed to validate the mechanistic proposal. This process involves the generation of an electrophilic *ortho* phenyl carbon via Ru-C bond formation and reduction of hydrogen peroxide.

This material is reserved for educational use only, not allowed for commercial use.

Forbidden to modify the content, and cite the document when use.



Scheme 4.2 The illustration of the production of 2-aminobenzothiazole from *N*-arylthiourea through mechanistic pathway A (blue line).

In the first step, the reactant (**REACT**) is simultaneously deprotonated by  $\text{H}_2\text{O}_2$  of both the thiourea nitrogen and a coordinated water molecule in ruthenium complex. This leads to the bond breaking of the peroxide bond giving rise to the intermediate (**INT1**).

In the transition state (**TS1**), the peroxide O–O bond distance increases from 1.44 Å in the **REACT** to 2.15 Å in **TS1**, and the two transferring protons have O---H distances of ~1.3 Å indicating a PCET event where two electrons have transferred prior as shown in Figure 4.2. **TS1** preferentially applies in the quartet spin state (3 unpaired electrons) and analysis of Natural bond orbital (NBO) indicates a homolytic process with the evolving radicals being confined to the ruthenium atom and both peroxide oxygen atoms at the transition state (Figure S2). **INT1** also favors a quartet spin state with the radical electrons located on the ruthenium atom, the substrate phenyl ring and the thiourea moiety (Scheme 4.2). The barrier to reaction (**TS1**) is found to be 16.2 kcal/mol while the intermediate (**INT1**) shows lower energy than the **REACT** (-33.1 kcal/mol) as shown in Table 4.1.

This material is reserved for educational use only, not allowed for commercial use.

Forbidden to modify the content, and cite the document when use.

In the process of **TS2**, Ru–C bond formation is required, which leads to the removal of water molecules from the ruthenium complex. **TS2** sees the Ru–C distance of the intermediate (**INT1**) shorten from 4.16 Å to 2.41 Å at the transition state (**TS2**). Simultaneously, the Ru–OH<sub>2</sub> bond elongates from 2.20 Å in **INT1** to 2.29 Å in **TS2** (Figure 4.2). **TS2** proceeds through doublet spin state with an energy barrier of 42.2 kcal/mol (Table 4.1), while the barrier energy value reported by Sharma et al. [18] for Ru–C bond formation was 26.5 kcal/mol. However, the results cannot be directly compared because different model system is used. The proton transfer step from the *ortho* carbon can occur in the latter step. Due to the large distance between the *ortho* carbon hydrogen and the ruthenium complex to 4.16 Å makes direct proton transfer impossible in conjunction with Ru–C bond formation.

**INT2** proceeds via the quartet spin state with an intermediate energy of -18.5 kcal/mol relative to **REACT** and 14.6 kcal/mol less stable than **INT1** (Table 4.1). This structure is observed to be consistent with structure C reported by Sharma et al. [18] in Scheme 3.1. NBO analysis displays the two radicals exist on the ruthenium complex, which can describe that the previous transition state had one radical on aromatic carbon in **INT1** delocalized to the ruthenium complex. And one radical delocalized within the  $\pi$  molecular orbitals (MO) of the thiourea substrate (Scheme 4.2).

**TS3** involves the proton attached to the *ortho* carbon of six-membered ring is transferred by the urea nitrogen. This process is carried out through proton shuttling from the surrounding two water molecules, which are generated from the reduction of peroxide and liberated on Ru–C bond formation. The C–H bond distance is elongated from 1.09 Å in **INT2** to 2.87 Å in **TS3**. Then the transfer of proton from isolated water molecule back to the urea nitrogen. The distance between N–H bond is found to be 1.57 Å in **TS3** (Figure 4.2), suggesting proton transfer after C–H bond breaking. It should be noted that proton shuttling event is performed using a doublet spin state and the aromatic ring is re-established through further electron rearrangement, i.e. PCET. The energy demand to overcome the transition barrier (**TS3**) is 11.5 kcal/mol (Table 4.1), relatively low, as expected in the reaction involving proton transfer.

**INT3** requires proton transfer and ring closure steps to form the product. The stationary point adopts the quartet state with radicals located over the ruthenium

complex. The resulting intermediate (**INT3**) has an energy relative to the reactant of -24.9 kcal/mol and being 6.4 kcal/mol more stable than **INT2** (Table 4.1).

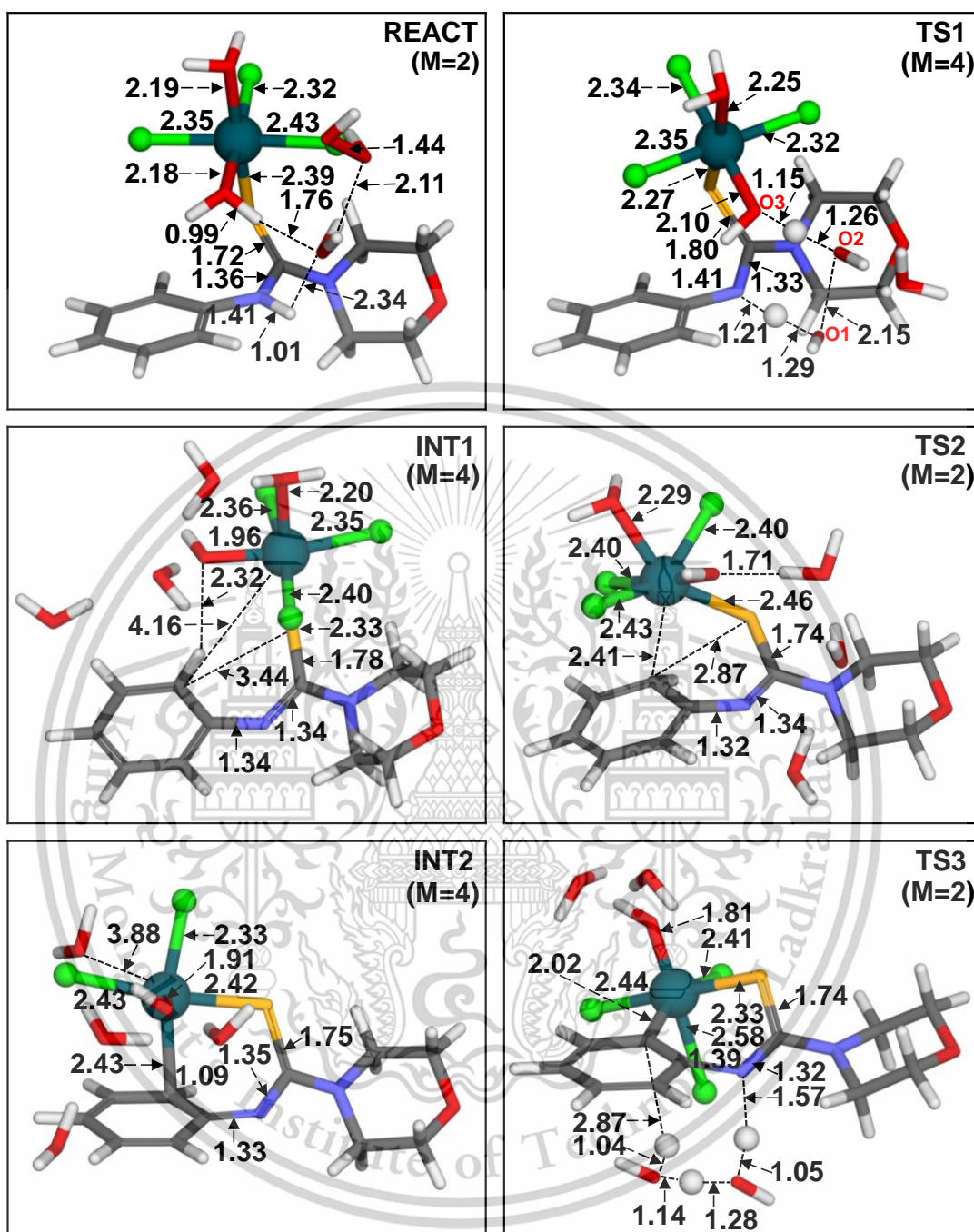
After **INT3** is formed, the reaction can proceed via two routes. Pathway A leads to **INT4** and **TS5** to form **PROD** while Pathway B proceeds through **INT5** to form **PROD** via **TS6** and **TS7**, respectively.

For **TS4**, the investigate focuses on proton transfer to give **INT4** lead to ring closure as the final step, as proposed by Sharma et al. [18] (Scheme 4.2). At the transition state, a proton is shuttled from the thiourea nitrogen to the Ru-bound hydroxide via two water molecules. It is found that the existence of hydronium ion in the transition state facilitates proton transfer. The corresponding distances are observed at N---H distance of 1.36 Å and O---H distance of 1.38 Å as shown in Figure 4.2. **TS4** proceeds preferentially in the quartet state with a barrier to reaction of 12.3 kcal/mol (Table 4.1).

**INT4** can be achieved in the quartet spin state with two radicals located on the ruthenium complex. Analysis of the Mulliken charge shows that there is a positive charge on the *ortho* carbon of the six-membered ring along with a delocalized radical within the substrate  $\pi$  system. This stationary point corresponds to a highly electrophilic carbon reported by Sharma et al in structure D (Scheme 3.1). **INT4** energy is found to be -25.3 kcal/mol relative to **REACT** and 0.4 kcal/mol lower in energy than **INT3** (Table 4.1).

**TS5** is the final step in Pathway A. This transition state involves the five-membered ring closure via the C-S cross-coupling and re-coordination of a water molecule with ruthenium to give an octahedral configuration (Scheme 4.2). The results of the Mulliken charge display the positive charge on *ortho* carbon in six-membered ring and the negative charge on thiourea correspond to the C-S bond formation, which leads to the formation of **PROD**. The C---S electrophile-nucleophile distance reduces from 3.06 Å in **INT4** to 2.57 Å in **TS5** (Figure 4.2). **TS5** proceeds via a doublet spin state with a relatively low barrier of 2.5 kcal/mol (Table 4.1).

**PROD** from this calculation is in the form of 2-aminobenzothiazole bonded with ruthenium complex catalyst and the structure is -77.2 kcal/mol lower than **REACT** (Table 4.1). The octahedral Ru-complex is performed using a doublet spin state with the radical located on the ruthenium atom.



This material is reserved for educational use only, not allowed for commercial use.

Forbidden to modify the content, and cite the document when use.

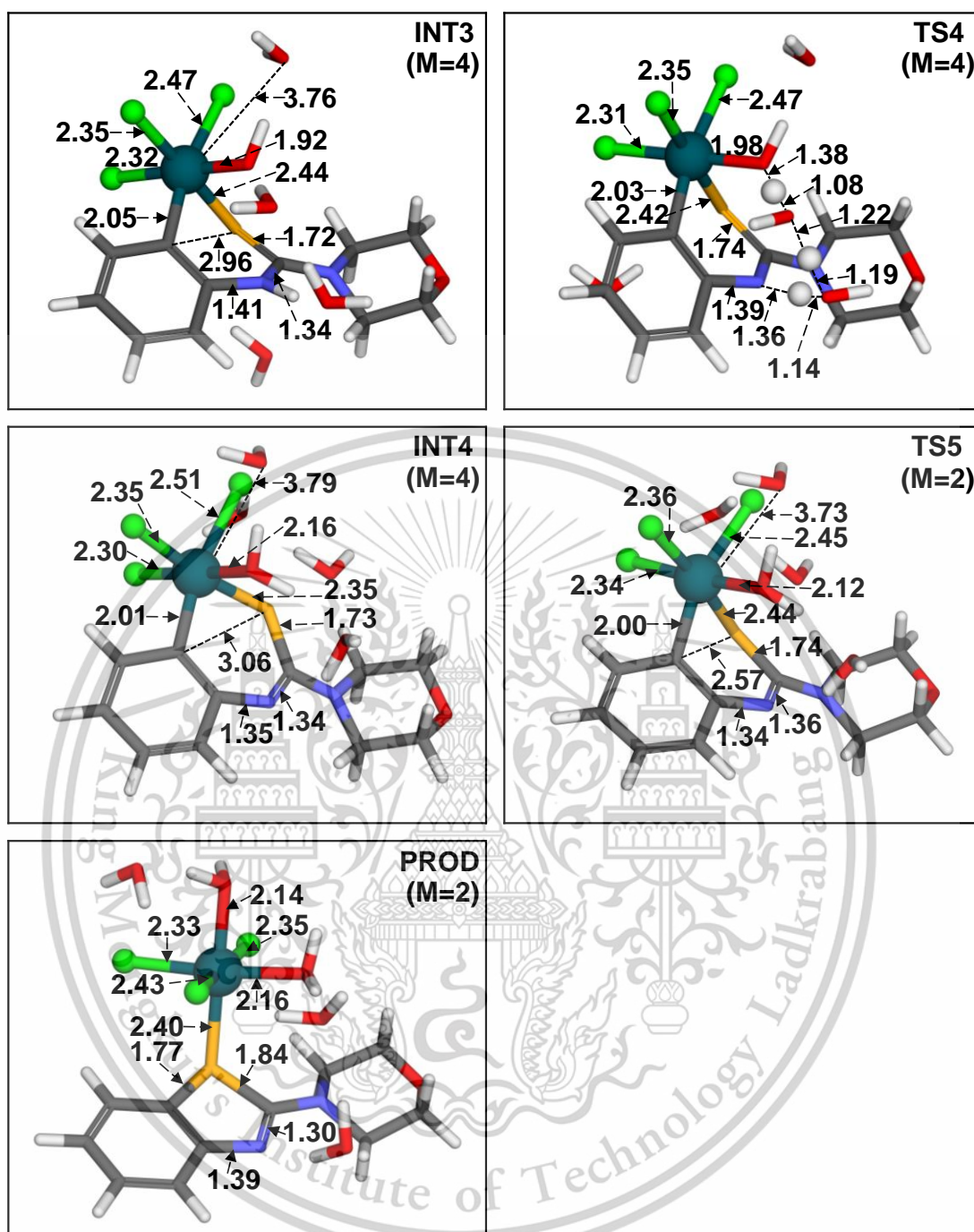
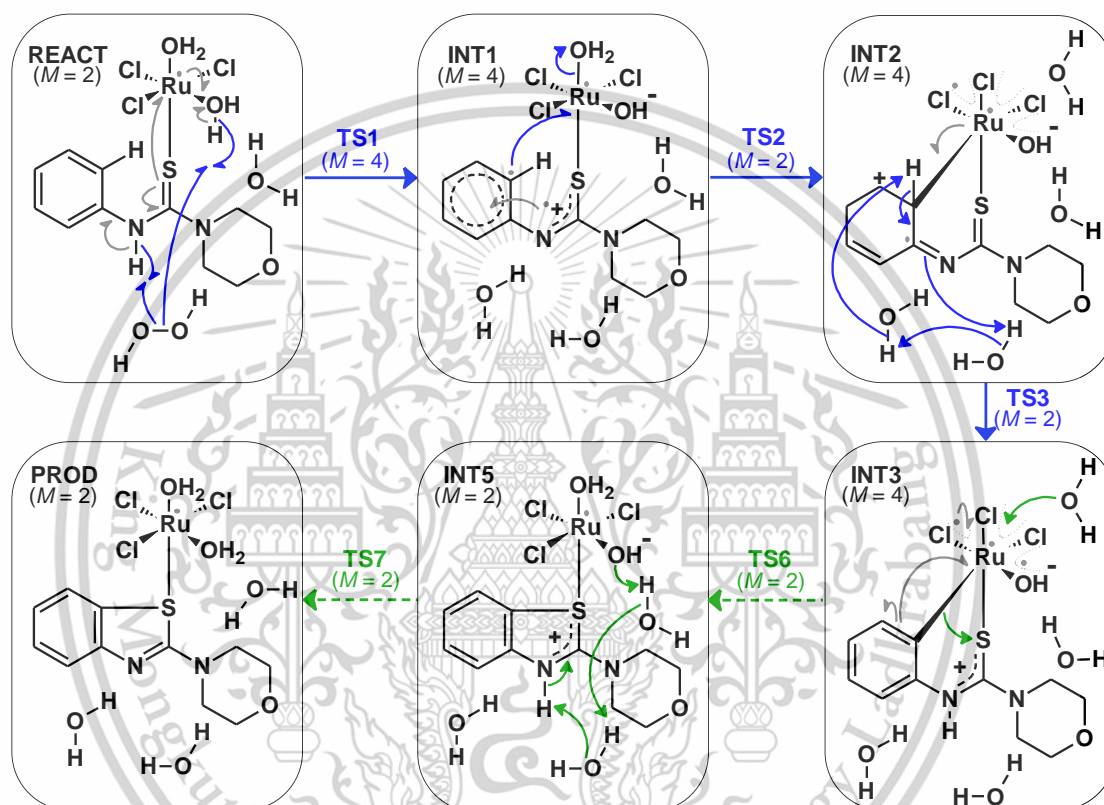


Figure 4.2 Optimized geometries obtained in the production of 2-aminobenzothiazole from *N*-arylthiourea in mechanistic pathway A (blue line). Key distances are illustrated in Å.

## 4.2 Pathway B

As mentioned earlier, **INT3** can undergo two catalytic routes, including **INT3** to **INT4** (Pathway A) and **INT3** to **INT5** (Pathway B). Both routes can yield 2-aminobenzothiazole as a product. For **INT5** to be formed from **INT3** via **TS6**, it is worth noting that in this step, the C–S coupling associated with the direct five-membered ring closure can occur prior to the proton transfer step.



**Scheme 4.3** The illustration of the production of 2-aminobenzothiazole from *N*-arylthiourea through mechanistic pathway B (green line).

For **TS6**, the C–S bond distance is found to be 2.75 Å in **TS6** reduced from 2.96 Å in **INT3** and is longer than **TS5**, which has a length of 2.57 Å (Figure 4.3). As with **TS5**, the structure of **TS6** preferentially adopts a doublet state. The results from Mulliken charge analysis suggest that there is a reduced electrophilicity of the six-membered ring ( $C_{ortho}$  charges of 0.606 (**TS5**) and 0.354 (**TS6**), Figure S3), resulting in an energy barrier for **TS6** of 10.8 kcal/mol (Table 4.1).

**INT5** sees the complete C–S cross-coupling to form a five-membered ring and the water ligand coordinates with the ruthenium complex (Scheme 4.3). The C–S bond length is shortened from 2.75 Å to 1.78 Å in **TS6** and **INT5**, respectively (Figure 4.3). The stationary point exists in the doublet spin state and has an energy of -75.9 kcal/mol lower than **REACT** (Table 4.1) due to the re-aromatization of the phenyl ring leads to highly exothermic activity.

For the reaction to be complete, **TS7** proceeds with a proton shuttle from the thiourea nitrogen to the Ru-bound hydroxide through two water molecules (Scheme 4.3). The proton shuttling is displayed in Figure 4.3. The N---H distance is found to be 1.04 Å in **INT5** and is elongated to 1.25 Å in **TS7**. The O---H distance is shortened from 1.68 Å in **INT5** to 1.48 Å in **TS7**. This step has a very low energy barrier of 3.9 kcal/mol (Table 4.1).

As illustrated in Figure 4.1, the rate-determining step for both Pathway A (blue) and Pathway B (green) is observed to be **TS2**, which corresponds to Ru–C bond formation. Pathway B is slightly more favored than Pathway A because **TS6** is lower than **TS4** by 1.5 kcal/mol. However, based on the single point energies, the free energy barrier of **TS4** is lower than that of **TS6** by -3.4 kcal/mol, suggesting that both pathways can potentially be completed.

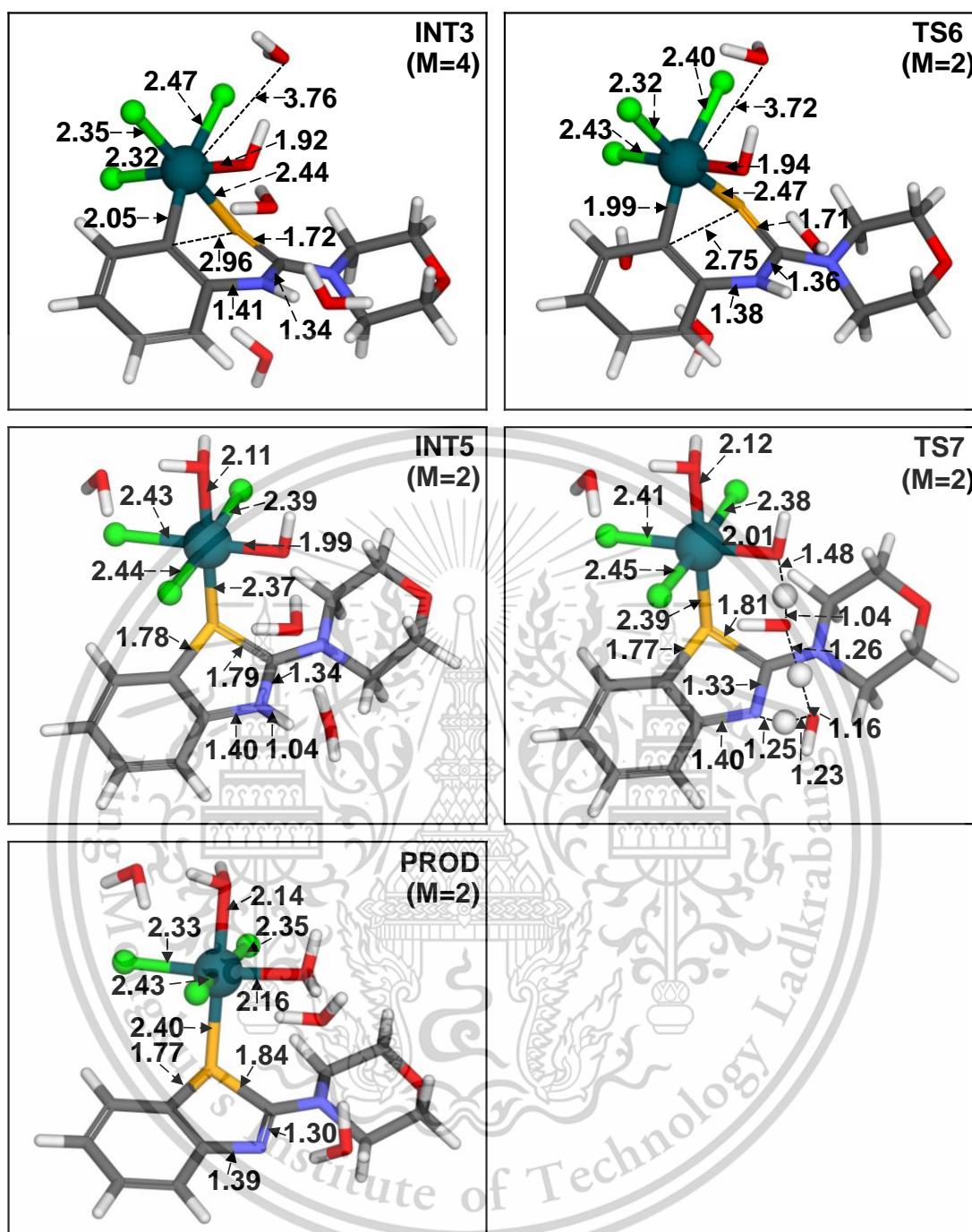
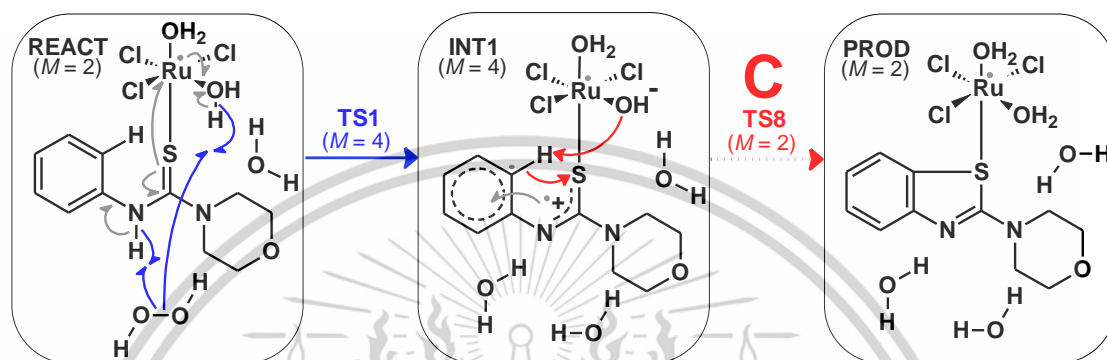


Figure 4.3 Optimized geometries obtained in the production of 2-aminobenzothiazole from *N*-arylthiourea in mechanistic pathway B (green line). Key distances are illustrated in Å. (For REACT, TS1, INT1, TS2, INT2 and TS3 can see at Figure 4.2).

### 4.3 Pathway C

A third mechanistic possibility was explored, where the direct formation of the Ru–C bond does not contribute to increasing the electrophilicity of the substrate. Indeed, this step is the rate-determining step in both Pathways A and B, having an energy barrier of 42.2 kcal/mol (Table 4.1 & Figure 4.1).



**Scheme 4.4** The illustration of the production of 2-aminobenzothiazole from *N*-aryltiourea through mechanistic pathway C (red line).

An alternative route (red) begins from INT1 via TS8 (Scheme 4.4) with a modest barrier of 16.2 kcal/mol. The transition state involves the *ortho* carbon proton is transferred to the Ru-bound hydroxide and C–S bond formation can occur. In Figure 4.4, the C–S distance decreases from 3.44 Å in INT1 to 2.47 Å in TS8, which is notably shorter than the corresponding distances in the other ring closure transition states (TS5 and TS6) at 2.57 Å and 2.75 Å, respectively. The proton coupled electron transfer (PCET) occurs after the transition state has been traversed as can be seen from the short C–H bond distance of 1.09 Å and long O–H interaction distance of 1.98 Å. The energy barrier to the reaction in this doublet spin transition state was found to be 7.7 kcal/mol (Table 4.1).

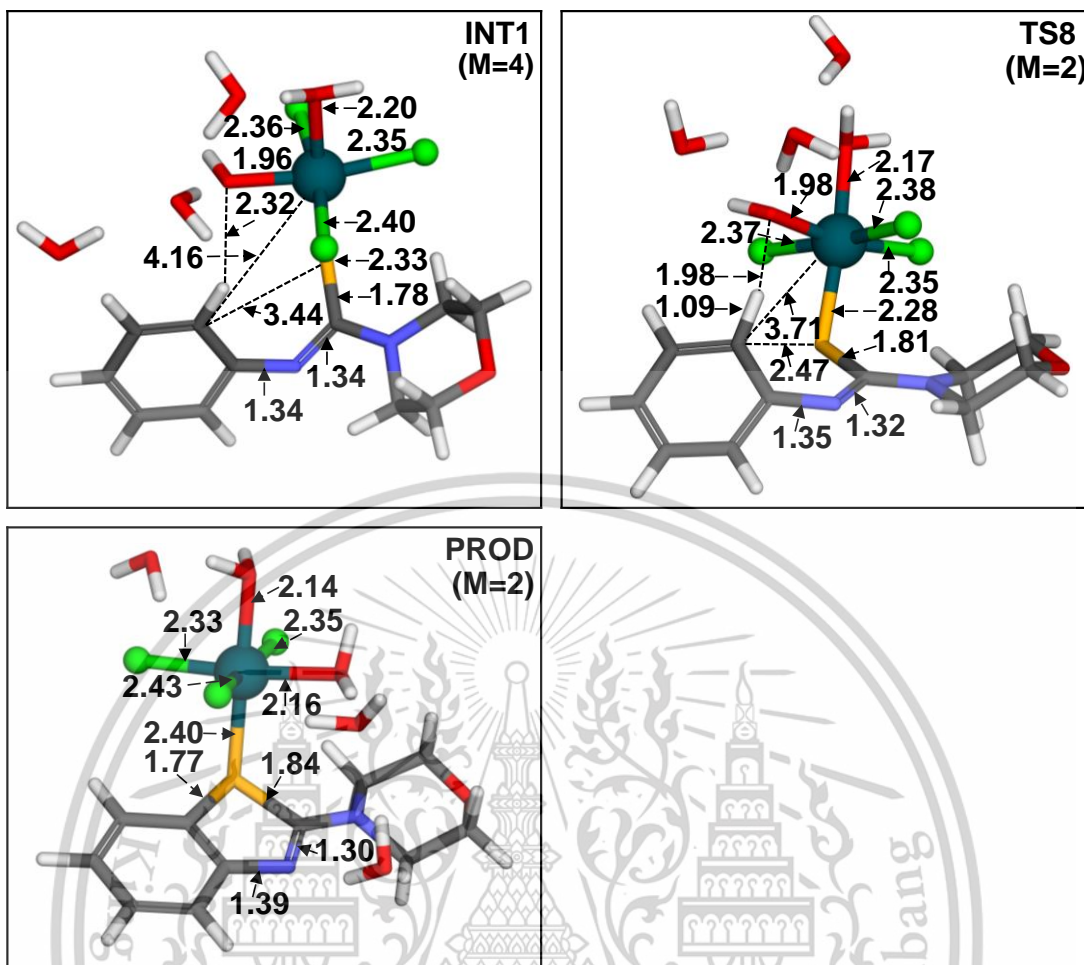


Figure 4.4 Optimized geometries obtained in the production of 2-aminobenzothiazole from *N*-aryltiourea in mechanistic pathway C (red line). Key distances are illustrated in Å. (For REACT and TS1 can see at Figure 4.2).

#### 4.4 Probable reaction mechanism

Three possible mechanistic pathways have been investigated for the conversion of *N*-aryltioureas to 2-aminobenzothiazoles using a  $\text{RuCl}_3$ -based catalytic system. Pathway A and Pathway B involve the direct formation of Ru–C bond to increase the electrophilicity of the *ortho* carbon of the aryl ring, as originally proposed by Sharma et al., while pathway C involves only charge transfer effects. The rate-determining step for both pathways A and B is **TS2**. However, for pathway C it is **TS8**.

**TS8** is considerably lower in energy than the alternative **TS2** which is also derived from **INT1**. Indeed, **TS2** is the rate-determining step for Pathways A and B, suggesting that a mechanism involving direct Ru–C bond is implausible. Instead, it is likely that

Ru increases the electrophilicity of the phenyl *ortho* carbon and the nucleophilicity of the thiolate via electron/charge transfer only. This means that the irreversible oxidative step (**TS1**, 16.2 kcal/mol) is the rate-determining step. Indeed, once **INT1** is formed, the reverse barrier to reaction is 49.3 kcal/mol. Thus, the subsequent traversal of **TS8** to form the benzothiazole product is facile. In addition, while Sharma et al. [18] found that the radical scavenging agent TEMPO does not affect the outcome of the reaction, given the low barrier to reaction for the quartet **INT1** state, it is plausible that insufficient time exists for it to undergo reaction with the radical inhibitor given the low barrier to forward reaction.

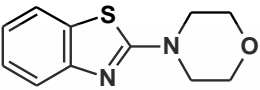
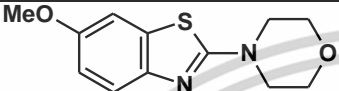
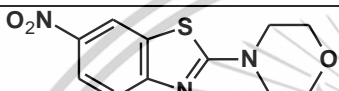
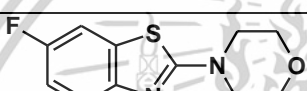
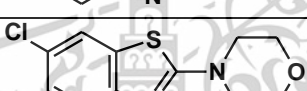
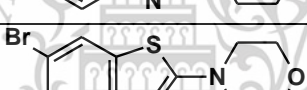
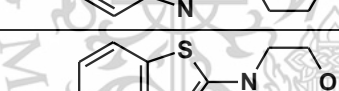
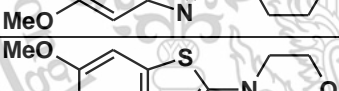
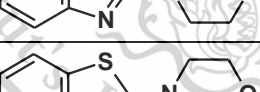

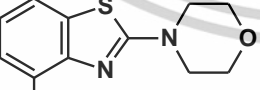
Another important consideration is that KIE ( $k_H/k_D$ ) studies were performed using a substrate with a deuterated *ortho* aryl carbon. However, no KIE was observed confirming that the transfer of *ortho* aryl carbon proton (i.e., **TS8** or **TS3**) cannot be involved in the rate-determining step. Indeed, this was a key element leading to Sharma et al. [18] proposing their original mechanism involving a direct Ru–C bond formation (i.e. via **TS2**).

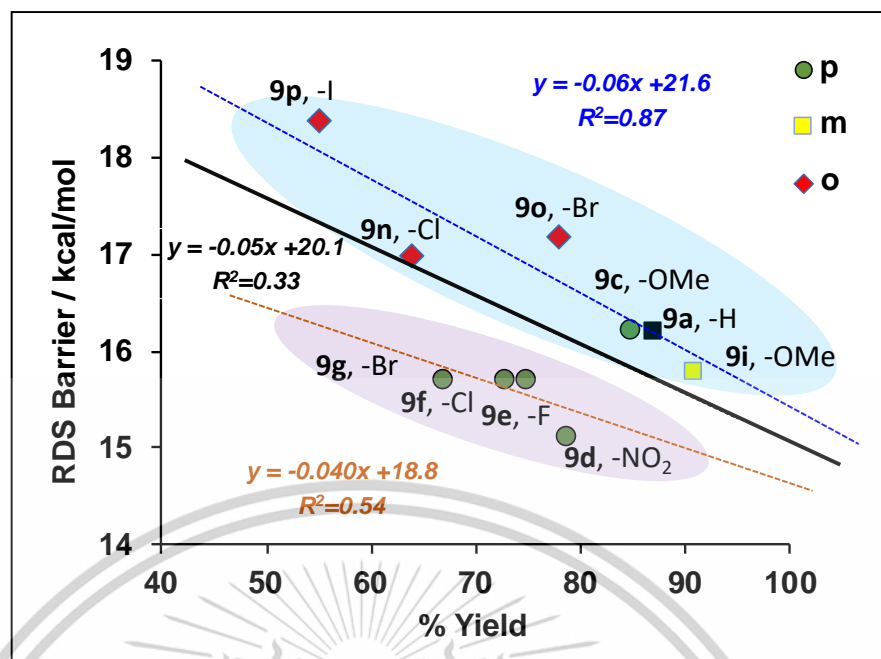
The findings are broadly in agreement with the proposals of Sharma et al. [18], yet it appears the role of ruthenium is to increase the electrophilicity of the aryl ring not through direct C–Ru bond formation, but rather through charge transfer effects. It is found that the oxidation of the peroxide bond (**TS1**) followed by rapid proton transfer and ring closure (**TS8**) is (a) consistent with the KIE and (b) energetically much more favorable than the former.

#### 4.5 Correlation of yield vs. RDS barrier

To assess the validity of the new mechanistic proposal, the correlation between the predicted rate-determining barrier (**TS1**) and the yield for 10 *N*-arylthioureas (9c–9g, 9i, 9n–9p) which display yields ranging from 91% to 55% had been investigated (Table 4.2). These cover a range of electron-donating/neutral (MeO, H) and withdrawing groups (F, Cl, Br, I, and NO<sub>2</sub>). The substituents also cover the *ortho*-, *meta*-, and *para*-positions of the aryl thioureas.

**Table 4.2** Computed energies obtained from the examination of the influence of electron-donating and electron-withdrawing groups substituent on the *ortho*-, *meta*-, and *para*-positions. Energies are relative to the reactant and reported in kcal/mol.

ID	Structure	% yield	TS1 (M=4)	PROD (M=2)
9a		87	16.2	-77.2
9c		85	16.2	-76.4
9d		79	15.1	-78.0
9e		75	15.7	-77.0
9f		73	15.7	-77.0
9g		67	15.7	-77.2
9i		91	15.8	-77.0
9i*		-	16.2	-76.4
9o		78	17.2	-77.1
9n		64	17.0	-77.0
9p		55	18.4	-78.4



**Figure 4.5** A comparison of TS1 ( $M = 4$ ) energy barriers and %yield, obtained for 9a and the substituents on the *ortho*-, *meta*-, and *para*-positions.

A plot of the **TS1** energy barriers versus the reported benzothiazole reaction yields is reported in Figure 4.5. A relatively weak correlation is observed for all 10 molecules as can be seen by the  $R^2$  of 0.33. The observation can be explained by the electron-donating substituents providing greater stabilization of the evolving positive charge on the aryl ring at **TS1**, leading to an increased yield. It should be noted that the correlation with the energy barriers of **TS2** was also assessed, however, no correlation was found ( $R^2 = 0.0$ ).

While the overall correlation between the %yields and **TS1** barrier is relatively weak, it is observed that the correlation markedly improves when the data are broken down by the substituent type and/or location. When exemplars with *para*-substituted electron-withdrawing substituents are excluded,  $R^2 = 0.87$  is observed (Figure 4.5). The latter set (9d, 9e, 9f, and 9g) is found to display much lower yields than would be expected based on their generally low barriers. In addition, the correlation within the excluded group is also much improved ( $R^2 = 0.54$ ).

The discrepancy between the two identified groups would suggest the model employed here does not describe some key experimental aspects of the real system. Indeed, the sterically less hindered *para*-substituted halides (9e, 9f, and 9g) potentially

undergo side reactions with catalytic metals such as ruthenium and palladium resulting in their lower than predicted yields [61, 74-76]. Additionally, the lower than predicted yields for 9d could be due to an effect noted by Sharma et al. [18] that the nitro group can potentially coordinate with Ru directly, thus leading to reduced reactivity.

Finally, it is interesting to note that the *meta*-methoxy substituent of 9i can potentially result in two isomers, denoted 9i and 9i\* in Table 4.2. Our calculations clearly show that 9i is kinetically and thermodynamically preferred as is expected given 9i\* is not reported under experimental conditions.



## Chapter 5

# Conclusions

This study presents a detailed DFT study exploring the mechanism of formation of a novel class of benzothiazoles via intramolecular C–S bond formation catalyzed via an electrophilic ruthenation pathway.

The results are in general agreement with Sharma et al. [18] that ruthenium acts to increase the electrophilicity of the aryl ring of the *N*-arylthioureas. However, our results suggest this is limited to charge transfer effects and does not necessitate Ru–C bond formation. It is found that the initial oxidative step (**TS1**) is rate-determining and that this is consistent with the observed kinetic isotope effects. Additionally, analysis of the relationship between the experimentally reported benzothiazole reaction yields and our predicted RDS barriers shows a good correlation giving us further confidence in our findings.

In summary, the results reported here are in good agreement with the experimental data reported on this reaction, showing the value of such calculations in synthetic organic chemistry. It shows that such calculations could prove useful to rapidly explore the scope of such reactions, predicting reaction selectivity or the potential outcomes with new, untested reagents.

## Suggestions for model design

From this study, we found that electron-donating and electron-withdrawing substituents at the *ortho*-, *meta*-, and *para*-positions of *N*-arylthioureas significantly affect the reactivity. The electron-donating substituent (OMe, 9i) at the *meta*-position was observed to increase the electron density in the neighboring positions, giving the *para*-positions of the substituent higher electron density which led to the formation of a C–S bond followed by proton transfer. These results are consistent with the high yield of 91% (9i) and the low energy required for the reaction being 15.8 kcal/mol. The properties of electron density are useful for predicting the selectivity of reactions. In the future, to achieve a higher yield of derivatives, it is possible to select substituents with stronger electron-donating properties such as -OH and -NH<sub>2</sub>. However, when the electron-withdrawing group is substituted at the *meta*-position, this will result in lower electron density at the *para*-position of the substituent. Therefore, *ortho* carbon have less electrophilicity, leading to reduced C–S bond formation.

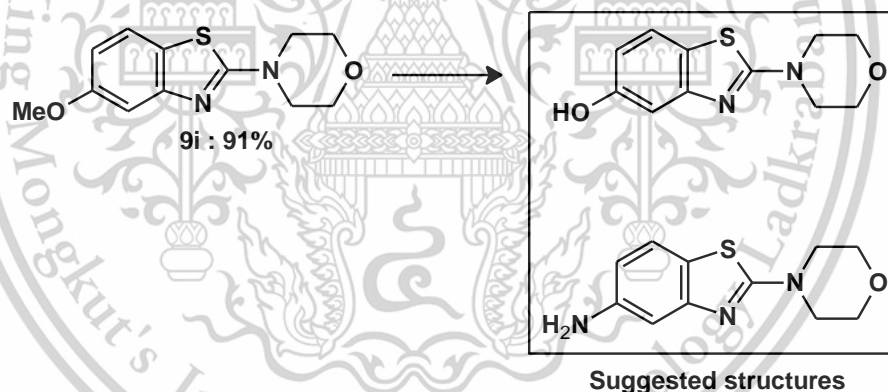


Figure 5.1 Drugs designed for chemical synthesis to improve reactivity for high yield.

## References

1. Sharma, P. C.; Sinhmar, A.; Sharma, A.; Rajak, H.; Pathak, D. P., Medicinal significance of benzothiazole scaffold: an insight view. *Journal of Enzyme Inhibition and Medicinal Chemistry* 2012, 28 (2), 240-266.
2. Singh, M.; Singh, S. K., Benzothiazoles: how relevant in cancer drug design strategy? *Anticancer Agents Med Chem* 2014, 14 (1), 127-46.
3. Kamal, A.; Syed, M. A. H.; Mohammed, S. M., Therapeutic potential of benzothiazole a patent review (2010-2014). *Expert Opinion on Therapeutic Patents* 2015, 25 (3), 335-349.
4. Borchers, A.; Pieler, T., Programming pluripotent precursor cells derived from *Xenopus* embryos to generate specific tissues and organs. *Genes (Basel)* 2010, 1 (3), 413-26.
5. Irfan, A.; Batool, F.; Zahra Naqvi, S. A.; Islam, A.; Osman, S. M.; Nocentini, A.; Alissa, S. A.; Supuran, C. T., Benzothiazole derivatives as anticancer agents. *Journal of Enzyme Inhibition and Medicinal Chemistry* 2019, 35 (1), 265-279.
6. Asiri, Y. I.; Alsayari, A.; Muhsinah, A. B.; Mabkhot, Y. N.; Hassan, M. Z., Benzothiazoles as potential antiviral agents. *J Pharm Pharmacol* 2020, 72 (11), 1459-1480.
7. Chen, C.; Chen, Y.-J., Liquid-phase synthesis of 2-substituted benzimidazoles, benzoxazoles and benzothiazoles. *Tetrahedron Letters* 2004, 45 (1), 113-115.
8. Mali, J. R.; Jawale, D. V.; Londhe, B. S.; Mane, R. A., An efficient green protocol for the synthesis of 2-aryl substituted benzothiazoles. *Green Chemistry Letters and Reviews* 2010, 3 (3), 209-212.
9. Yella, R.; Murru, S.; Ali, A. R.; Patel, B. K., Arylthioureas with bromine or its equivalents gives no 'Hugerschoff' reaction product. *Organic & Biomolecular Chemistry* 2010, 8 (15), 3389.
10. Laitonjam, W. S.; Nahakpam, L., Mechanistic Study on the Formation of Compounds from Thioureas. 2018.
11. Sahoo, S. K.; Banerjee, A.; Chakraborty, S.; Patel, B. K., Regioselective Intramolecular Arylthiolations by Ligand Free Cu and Pd Catalyzed Reaction. *ACS Catalysis* 2012, 2 (4), 544-551.

This material is reserved for educational use only, not allowed for commercial use.

Forbidden to modify the content, and cite the document when use.

12. Cheng, Y.; Peng, Q.; Fan, W.; Li, P., Room-temperature ligand-free Pd/C-catalyzed C-S bond formation: synthesis of 2-substituted benzothiazoles. *J Org Chem* 2014, 79 (12), 5812-9.
13. Hegedus, L. L.; Pereira, C. J., REACTION ENGINEERING FOR CATALYST DESIGN. *Chemical Engineering Science* 1990, 45 (8), 2027-2044.
14. Shi, W.; Liu, C.; Lei, A., Transition-metal catalyzed oxidative cross-coupling reactions to form C-C bonds involving organometallic reagents as nucleophiles. *Chemical Society Reviews* 2011, 40 (5), 2761.
15. Liu, C.; Zhang, H.; Shi, W.; Lei, A., Bond Formations between Two Nucleophiles: Transition Metal Catalyzed Oxidative Cross-Coupling Reactions. *Chemical Reviews* 2011, 111 (3), 1780-1824.
16. Louillat, M.-L.; Patureau, F. W., Oxidative C-H amination reactions. *Chem. Soc. Rev.* 2014, 43 (3), 901-910.
17. Shen, C.; Zhang, P.; Sun, Q.; Bai, S.; Hor, T. S.; Liu, X., Recent advances in C-S bond formation via C-H bond functionalization and decarboxylation. *Chem Soc Rev* 2015, 44 (1), 291-314.
18. Sharma, S.; Pathare, R. S.; Maurya, A. K.; Gopal, K.; Roy, T. K.; Sawant, D. M.; Pardasani, R. T., Ruthenium Catalyzed Intramolecular C-S Coupling Reactions: Synthetic Scope and Mechanistic Insight. *Organic Letters* 2016, 18 (3), 356-359.
19. Romero, A. H., Fused Heteroaromatic Rings via Metal-Mediated/Catalyzed Intramolecular C-H Activation: A Comprehensive Review. *Top Curr Chem (Cham)* 2019, 377 (4), 21.
20. Al Mamari, H. H.; Štefane, B.; Žugelj, H. B., Metal-catalyzed C-H bond functionalization of phenol derivatives. *Tetrahedron* 2020, 76 (9), 130925.
21. Henry, M. C.; Abbinante, V. M.; Sutherland, A., Iron-Catalyzed Regioselective Synthesis of 2-Arylbenzoxazoles and 2-Arylbenzothiazoles via Alternative Reaction Pathways. *European Journal of Organic Chemistry* 2020, 2020 (19), 2819-2826.
22. Li, H.; Hall, M. B., Mechanism of the formation of carboxylate from alcohols and water catalyzed by a bipyridine-based ruthenium complex: a computational study. *J Am Chem Soc* 2014, 136 (1), 383-95.

23. Manca, G.; Gallo, E.; Intrieri, D.; Mealli, C., DFT Mechanistic Proposal of the Ruthenium Porphyrin-Catalyzed Allylic Amination by Organic Azides. *ACS Catalysis* 2014, 4 (3), 823-832.
24. Zhou, Z.; Chen, S.; Hong, Y.; Winterling, E.; Tan, Y.; Hemming, M.; Harms, K.; Houk, K. N.; Meggers, E., Non-C(2)-Symmetric Chiral-at-Ruthenium Catalyst for Highly Efficient Enantioselective Intramolecular C(sp<sup>3</sup>)-H Amidation. *J Am Chem Soc* 2019, 141 (48), 19048-19057.
25. Djuidje, E. N.; Barbari, R.; A., B.; Durini, E.; Sciabica, S.; Balzarini, J.; Liekens, S.; Vertuani, S.; Manfredini, S., Benzothiazole Derivatives as Multifunctional Antioxidant Agents for Skin Damage: Structure–Activity Relationship of a Scaffold Bearing a Five-Membered Ring System. *Antioxidants (Basel)* 2022, 11 (2), 407.
26. Batista, R. M. F.; Costa, S. P. G.; Raposo, M. M. M., Synthesis of new fluorescent 2-(2',2''-bithienyl)-1,3-benzothiazoles. *Tetrahedron Letters* 2004, 45 (13), 2825-2828.
27. Praveen, C.; Nandakumar, A.; Dheenkumar, P.; Muralidharan, D.; Perumal, P. T., Microwave-assisted one-pot synthesis of benzothiazole and benzoxazole libraries as analgesic agents. *Journal of Chemical Sciences* 2012, 124 (3), 609–624.
28. Ye, L.-m.; Chen, J.; Mao, P.; Mao, Z.-f.; Zhang, X.-j.; Yan, M., Visible-light-promoted synthesis of benzothiazoles from 2-aminothiophenols and aldehydes. *Tetrahedron Letters* 2017, 58 (9), 874-876.
29. Merroun, Y.; Chehab, S.; Ghailane, T.; Akhazzane, M.; Souizi, A.; Ghailane, R., Preparation of tin-modified mono-ammonium phosphate fertilizer and its application as heterogeneous catalyst in the benzimidazoles and benzothiazoles synthesis. *Reaction Kinetics, Mechanisms and Catalysis* 2018, 126 (1), 249-264.
30. Bhat, R.; Karhale, S.; Arde, S.; Helavi, V., Acacia concinna pod catalyzed synthesis of 2-arylbenzothia/(oxa)zole derivatives. *Iranian Journal of Catalysis* 2019, 9 (2), 173-179.
31. Mayo, M. S.; Yu, X.; Zhou, X.; Feng, X.; Yamamoto, Y.; Bao, M., Convenient Synthesis of Benzothiazoles and Benzimidazoles through Brønsted Acid Catalyzed Cyclization of 2-Amino Thiophenols/Anilines with  $\beta$ -Diketones. *American Chemical Society (Organic Letters)* 2014, 16 (3), 764–767.

32. Loukrakpam, D. C.; Phukan, P., TsNBr<sub>2</sub> Mediated Synthesis of 2-Acylbenzothiazoles and Quinoxalines from Aryl Methyl Ketones under Metal Free Condition. *ChemistrySelect* 2019, 4 (11), 3180-3184.
33. Dar, A. A.; Shadab, M.; Khan, S.; Ali, N.; Khan, A. T., One-Pot Synthesis and Evaluation of Antileishmanial Activities of Functionalized S-Alkyl/Aryl Benzothiazole-2-carbothioate Scaffold. *J Org Chem* 2016, 81 (8), 3149-60.
34. Luo, B.; Li, D.; Zhang, A. L.; Gao, J. M., Synthesis, Antifungal Activities and Molecular Docking Studies of Benzoxazole and Benzothiazole Derivatives. *Molecules* 2018, 23 (10).
35. Sharghi, H.; Asemani, O., Methanesulfonic Acid/SiO<sub>2</sub> as an Efficient Combination for the Synthesis of 2-Substituted Aromatic and Aliphatic Benzothiazoles from Carboxylic Acids. *Synthetic Communications* 2009, 39 (5), 860-867.
36. Coelho, F. L.; Campo, L. F., Synthesis of 2-arylbenzothiazoles via direct condensation between in situ generated 2-aminothiophenol from disulfide cleavage and carboxylic acids. *Tetrahedron Letters* 2017, 58 (24), 2330-2333.
37. Xu, Z. M.; Li, H. X.; Young, D. J.; Zhu, D. L.; Li, H. Y.; Lang, J. P., Exogenous Photosensitizer-, Metal-, and Base-Free Visible-Light-Promoted C-H Thiolation via Reverse Hydrogen Atom Transfer. *Org Lett* 2019, 21 (1), 237-241.
38. Chun, S.; Yang, S.; Chung, Y. K., Synthesis of benzothiazoles from 2-aminobenzenethiols in the presence of a reusable polythiazolium precatalyst under atmospheric pressure of carbon dioxide. *Tetrahedron* 2017, 73 (25), 3438-3442.
39. Magano, J.; Dunetz, J. R., Large-scale applications of transition metal-catalyzed couplings for the synthesis of pharmaceuticals. *Chem Rev* 2011, 111 (3), 2177-250.
40. Banerjee, A.; Santra, S. K.; Rout, S. K.; Patel, B. K., A ligand free copper(II) catalyst is as effective as a ligand assisted Pd(II) catalyst towards intramolecular C-S bond formation via C-H functionalization. *Tetrahedron* 2013, 69 (43), 9096-9104.
41. Ueda, S.; Nagasawa, H., Copper-Catalyzed Synthesis of Benzoxazoles via a Regioselective C-H Functionalization/C-O Bond Formation under an Air Atmosphere. *The Journal of Organic Chemistry* 2009, 74 (11), 4272-4277.

42. King, A. E.; Huffman, L. M.; Casitas, A.; Costas, M.; Ribas, X.; Stahl, S. S., Copper-Catalyzed Aerobic Oxidative Functionalization of an Arene C-H Bond: Evidence for an Aryl-Copper(III) Intermediate. *Journal of the American Chemical Society* 2010, *132* (34), 12068–12073.
43. Bagayoko, D., Understanding density functional theory (DFT) and completing it in practice. *AIP ADVANCES* 2014, *4*, 127104.
44. Leach, A. R., *Molecular modelling principles and applications*. Henry Ling Ltd: England, 2001.
45. Cramer, C. J., *Essentials of Computational Chemistry Theories and Models*. John Wiley & Sons Ltd: England, 2004.
46. Jensen, F., *Introduction to Computational Chemistry*. John Wiley & Sons Ltd: England, 2007.
47. Electronic wave functions - I. A general method of calculation for the stationary states of any molecular system. *Proceedings of the Royal Society of London. Series A. Mathematical and Physical Sciences* 1997, *200* (1063), 542-554.
48. Krylov, A. I., *The Quantum Chemistry of Open-Shell Species*. First Edition ed.; John Wiley & Sons, Inc.: 2017; Vol. 30.
49. Jacob, C. R.; Reiher, M., Spin in density-functional theory. *International Journal of Quantum Chemistry* 2012, *112* (23), 3661-3684.
50. Savarese, M.; Bremond, E.; Ciofini, I.; Adamo, C., Electron Spin Densities and Density Functional Approximations: Open-Shell Polycyclic Aromatic Hydrocarbons as Case Study. *J Chem Theory Comput* 2020, *16* (6), 3567-3577.
51. Nandi, P. K.; Kar, T.; Sannigrahi, A. B., Effect of spin contamination in UHF wavefunctions on charge density-based local quantities. *Journal of Molecular Structure (Theochem)* 1996, *362*, 69-75.
52. Menon, A. S.; Radom, L., Consequences of Spin Contamination in Unrestricted Calculations on Open-Shell Species: Effect of Hartree-Fock and Møller-Plesset Contributions in Hybrid and Double-Hybrid Density Functional Theory Approaches. *The Journal of Physical Chemistry A* 2008, *112* (50), 13225–13230.
53. Ang, L. S.; Sulaiman, S.; Mohamed-Ibrahim, M. I., Effects of Spin Contamination on the Stability and Spin Density of Wavefunction of Graphene: Comparison

- between First Principle and Density Functional Methods. *Sains Malaysiana* 2012, 41 (4), 445-452.
54. Simmons, E. M.; Hartwig, J. F., On the interpretation of deuterium kinetic isotope effects in C-H bond functionalizations by transition-metal complexes. *Angew Chem Int Ed Engl* 2012, 51 (13), 3066-72.
55. Gómez-Gallego, M.; Sierra, M. A., Kinetic Isotope Effects in the Study of Organometallic Reaction Mechanisms. *Chemical Reviews* 2011, 111 (8), 4857-4963.
56. Tunge, J. A.; Foresee, L. N., Mechanistic Studies of Fujiwara Hydroarylation. C-H Activation versus Electrophilic Aromatic Substitution. *Organometallics* 2005, 24 (26), 6440-6444.
57. Gao, M.-Y.; Li, J.-H.; Zhang, S.-B.; Chen, L.-J.; Li, Y.-S.; Dong, Z.-B., A Mild Synthesis of 2-Substituted Benzothiazoles via Nickel-Catalyzed Intramolecular Oxidative C-H Functionalization. *The Journal of Organic Chemistry* 2019, 85 (2), 493-500.
58. Moto Ongagna, J.; Tamafo Fouegue, A. D.; Ateba Amana, B.; Mouzong D'ambassa, G.; Zobo Mfomo, J.; Mbaze Meva, A. L.; Bikele Mama, D., B3LYP, M06 and B3PW91 DFT assignment of nd(8) metal-bis-(N-heterocyclic carbene) complexes. *J Mol Model* 2020, 26 (9), 246.
59. Broudic, N.; Pacheco-Benichou, A.; Fruit, C.; Besson, T., Synthesis of 2-Cyanobenzothiazoles via Pd-Catalyzed/Cu-Assisted C-H Functionalization/Intramolecular C-S Bond Formation from N-Arylcyanothioformamides. *Molecules* 2022, 27 (23).
60. Sousa, L. M.; Araújo, D. M. S.; Oliveira, K. M.; De Oliveira, L. P.; Maia, P. I. S.; Deflon, V. M.; Batista, A. A.; Machado, A. E. H.; Guerra, W.; Von Poelhsitz, G., Synthesis, spectroscopic characterization and computational study of Ru(II)/DMSO complexes with monocoordinated carbazate ligands. *Journal of Coordination Chemistry* 2020, 73 (10), 1605-1618.

61. Ghosh, M. K.; Mandal, S.; Islam, A.; Mohapatra, S.; Chattopadhyay, S., Ruthenium-Carbon(Aryl) Bond Cleavage and Change in the Ligand Coordination Mode in a Four-Membered Ortho-Metalated Ruthenium(II) Organometallics Promoted by Thiolato Ligands. *ChemistrySelect* 2017, 2 (23), 6710-6716.
62. Ben Said, R.; Hussein, K.; Tangour, B.; Sabo-Etienne, S.; Barthelat, J.-C., A density functional theory study of dinitrogen bonding in ruthenium complexes. *Journal of Organometallic Chemistry* 2003, 673 (1-2), 56-66.
63. Gao, Y.; Zhu, Y.; Chen, Z.; Zeng, Q.; Hu, C., Insights into the difference in metal-free activation of peroxymonosulfate and peroxydisulfate. *Chemical Engineering Journal* 2020, 394, 123936.
64. Flanagan, J.; Griffith, W. P.; Skapski, A. C., The active principle of Caro's acid, HSO<sub>5</sub> : X-ray crystal structure of KHSO<sub>5</sub>·H<sub>2</sub>O. *J. Chem. Soc., Chem. Commun.* 1984, (23), 1574-1575.
65. Becke, A. D., Density-functional thermochemistry. III. The role of exact exchange. *The Journal of Chemical Physics* 1993, 98 (7), 5648-5652.
66. Grellier, M.; Ayed, T.; Barthelat, J.; Albinati, A.; Mason, S.; Vendier, L.; Coppel, Y.; Sabo-Etienne, S., Versatile Coordination of 2-Pyridinetetramethyldisilazane at Ruthenium: Ru(II) vs Ru(IV) As Evidenced by NMR, X-ray, Neutron, and DFT Studies. *Journal of the American Chemical Society* 2009, 131 (22), 7633-7640.
67. Zhang, T.; Li, T.; Wu, X.; Li, J., Theoretical Study of Ruthenium(0)-Catalyzed Transfer Hydrogenative Cycloaddition of Cyclohexadiene and Norbornadiene with 1,2-Diols to Form Bridged Carbocycles. *J Org Chem* 2019, 84 (6), 3377-3387.
68. Tutkowski, B.; Meggers, E.; Wiest, O., Understanding Rate Acceleration and Stereinduction of an Asymmetric Giese Reaction Mediated by a Chiral Rhodium Catalyst. *J Am Chem Soc* 2017, 139 (24), 8062-8065.
69. Song, A.; Lee, J. C.; Parker, K. A.; Sampson, N. S., Scope of the Ring-Opening Metathesis Polymerization (ROMP) Reaction of 1-Substituted Cyclobutenes. *Journal of the American Chemical Society* 2010, 132 (30), 10513-10520.
70. Hückmann, L.; Álvarez-Barcia, S.; Fuhrer, M.; Plietker, B.; Kästner, J., Ruthenium-Catalyzed Secondary Amine Formation Studied by Density Functional Theory. *ChemCatChem* 2021, 13 (5), 1383-1388.

71. Weigend, F.; Ahlrichs, R., Balanced basis sets of split valence, triple zeta valence and quadruple zeta valence quality for H to Rn: Design and assessment of accuracy. *Phys Chem Chem Phys* 2005, 7 (18), 3297-305.
72. Zhang, G.; Liu, C.; Yi, H.; Meng, Q.; Bian, C.; Chen, H.; Jian, J.; Wu, L.; Lei, A., External Oxidant-Free Oxidative Cross-Coupling: A Photoredox Cobalt-Catalyzed Aromatic C-H Thiolation for Constructing C-S Bonds. *Journal of the American Chemical Society* 2015, 137 (29), 9273–9280.
73. Cheng, Y.; Yang, J.; Qu, Y.; Li, P., Aerobic Visible-Light Photoredox Radical C-H Functionalization: Catalytic Synthesis of 2-Substituted Benzothiazoles. *Organic Letters* 2012, 14 (1), 98–101.
74. Moloto, B. P.; Vermeeren, P.; Dalla Tiezza, M.; Esterhuysen, C.; Bickelhaupt, F. M.; Hamlin, T. A., Palladium-Catalyzed Activation of Carbon–Halogen Bonds: Electrostatics-Controlled Reactivity. *European Journal of Organic Chemistry* 2022, 2022 (26).
75. Lei, M.; Tang, Y.; Wang, H.; Zhu, L.; Zhang, G.; Zhou, Y.; Tang, H., A catalytic strategy for rapid cleavage of C-Cl bond under mild conditions: Effects of active hydrogen induced by Pd nanoparticles on the complete dechlorination of chlorobenzenes. *Chemical Engineering Journal* 2021, 419, 129510.
76. Kondo, Y.; Inamoto, K.; Nozawa, K., Palladium-Catalyzed C-H Cyclization in Water: A Milder Route to 2-Arylbenthiazoles. *Synlett* 2012, 23 (11), 1678-1682.



This material is reserved for educational use only, not allowed for commercial use.

Forbidden to modify the content, and cite the document when use.

## Appendix A: Supporting information

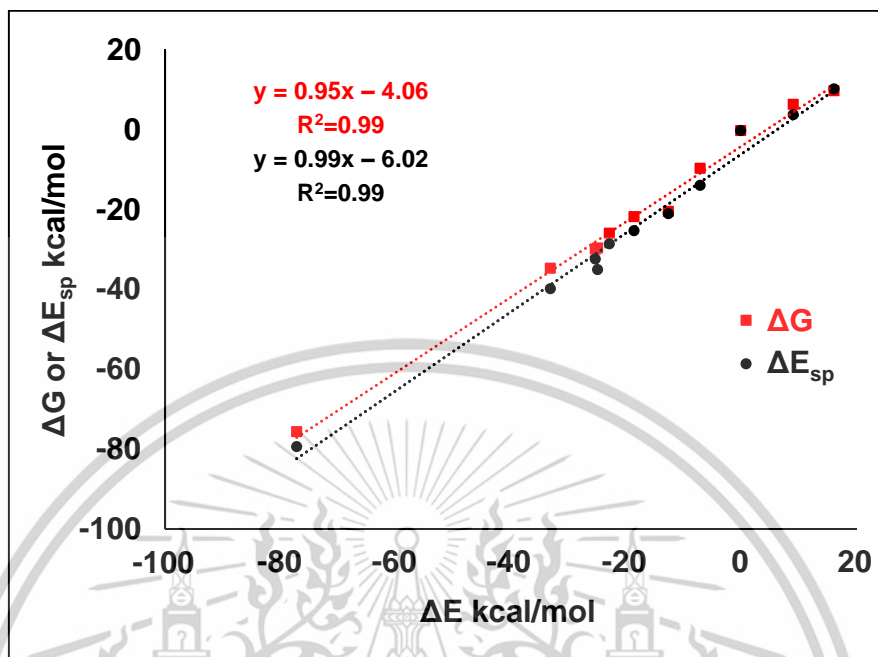
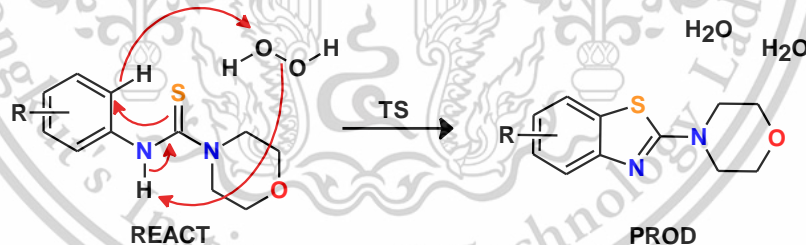


Figure S1. Correlation between the calculated  $\Delta E$ ,  $\Delta G$  (red square) and  $\Delta E_{sp}$  (black dot) for stationary points in this study.



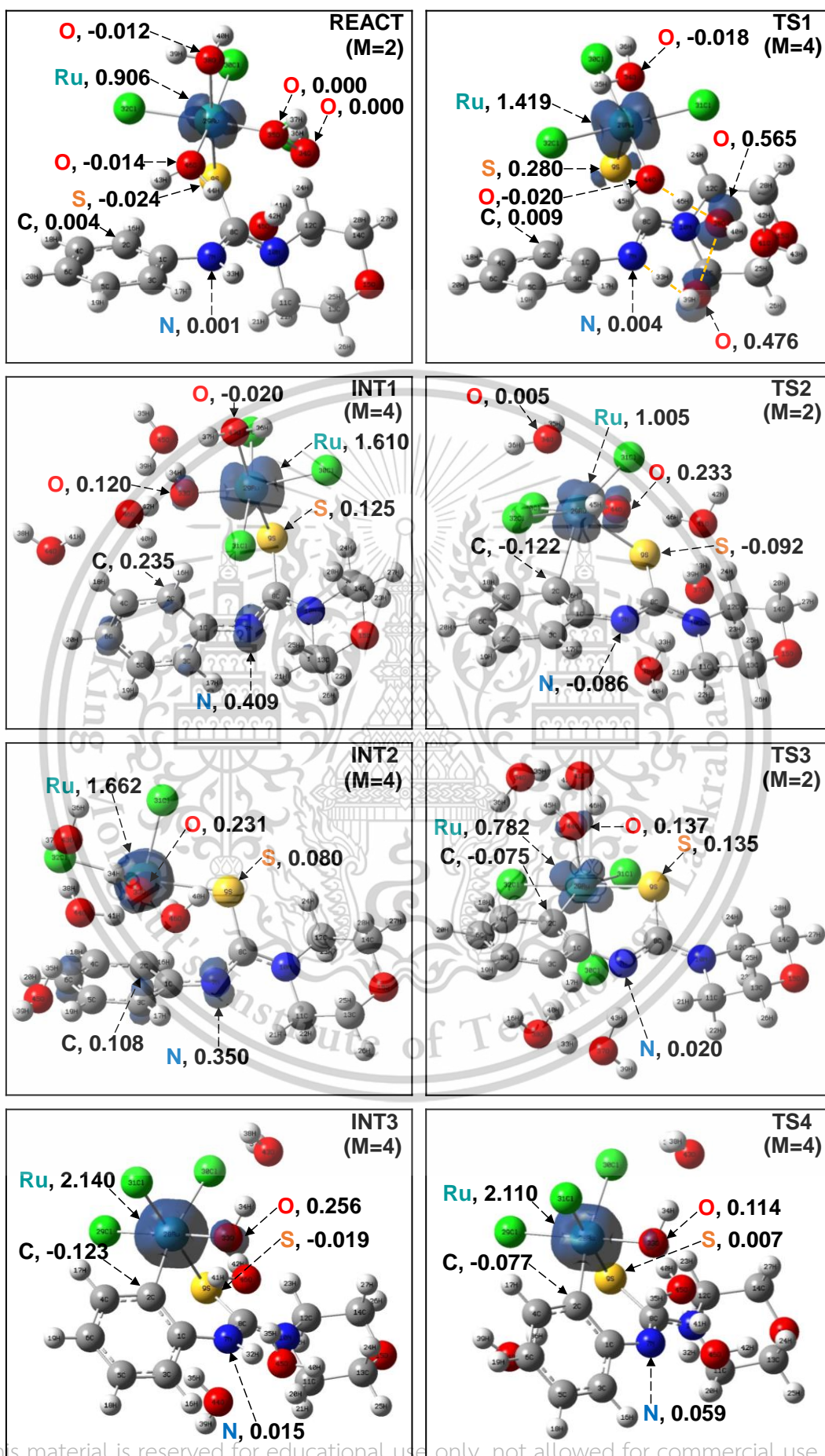
Scheme S1. Uncatalyzed reaction pathway (yellow pathway).

Table S1. The values of  $\langle S^2 \rangle$  before and after annihilation of spin contamination.

	Multiplicity=2			Multiplicity=4		
	$\langle S^2 \rangle$ before	$\langle S^2 \rangle$ after	%error	$\langle S^2 \rangle$ before	$\langle S^2 \rangle$ after	%error
REACT	0.7549	0.7500	0.00	3.7682	3.7501	0.00
TS1	1.7646	0.8107	8.09	3.7678	3.7501	0.00
INT1	1.7856	0.8876	18.35	3.7887	3.7507	0.02
TS2	0.8367	0.7527	0.36	-	-	-
INT2	1.7580	0.8858	18.11	3.7949	3.7509	0.02
TS3	0.7762	0.7502	0.03	-	-	-
INT3	1.2885	0.7662	2.16	3.7713	3.7502	0.01
TS4	0.9926	0.7563	0.84	3.7714	3.7502	0.01
INT4	1.3544	0.8062	7.49	3.7765	3.7503	0.01
TS5	1.3842	0.7856	4.75	-	-	-
TS6	0.8332	0.7513	0.17	-	-	-
INT5	0.7539	0.7500	0.00	3.7630	3.7501	0.00
TS7	0.7539	0.7500	0.00	3.7633	3.7501	0.00
TS8	1.2756	0.7689	2.52	3.7932	3.7508	0.02
PROD	0.7541	0.7500	0.00	3.7653	3.7501	0.00

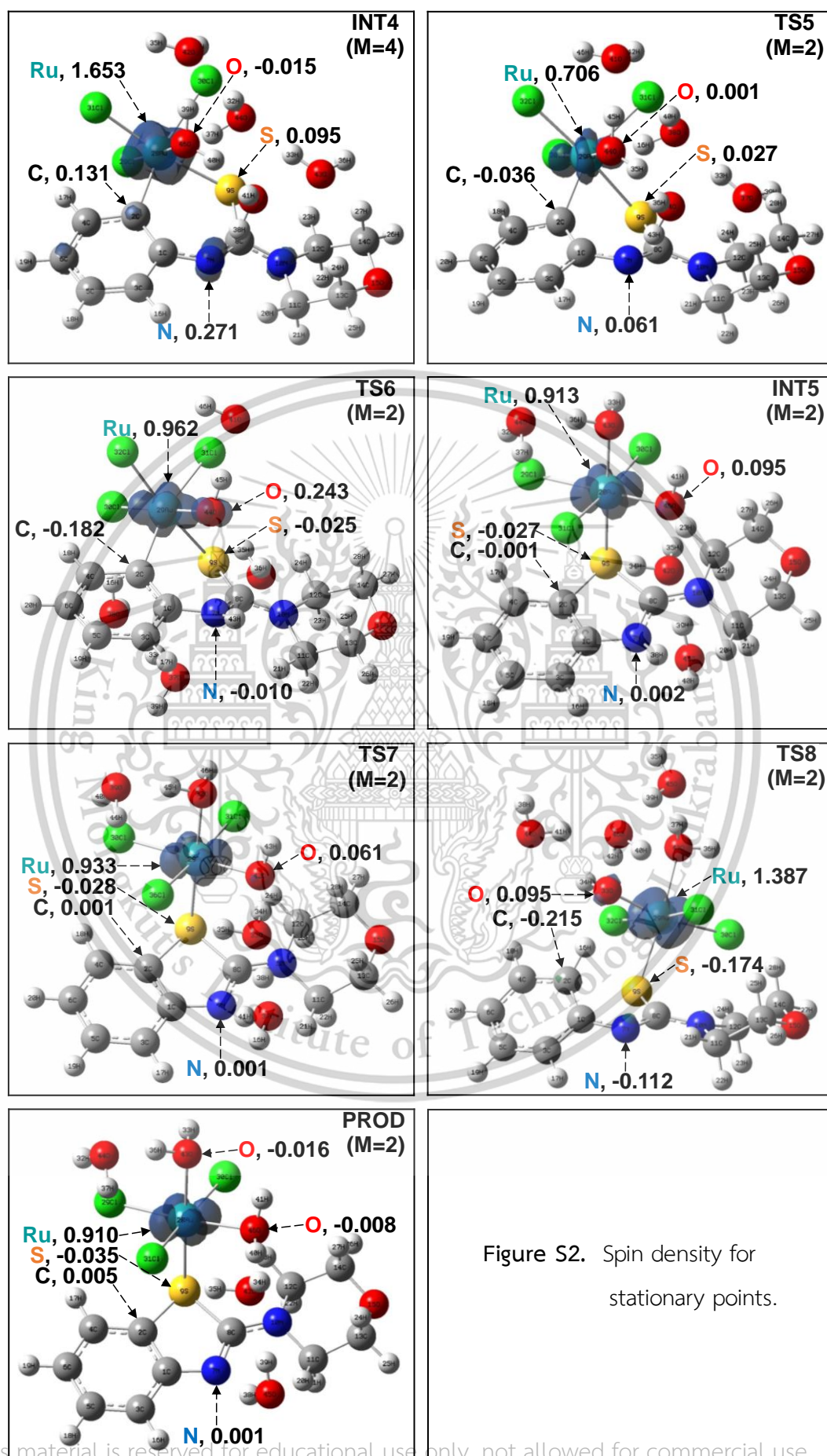
**Table S2.** Computed  $\Delta E$ ,  $\Delta G$  and  $\Delta E_{sp}$  energies of reactant, transition state structures, intermediates and product. Energies are in kcal/mol and relative to REACT. Values given in parenthesis are the barriers relative to their corresponding minima.

	Multiplicity 2			Multiplicity 4		
	$\Delta E$	$\Delta G$	$\Delta E_{sp}$	$\Delta E$	$\Delta G$	$\Delta E_{sp}$
<b>REACT</b>	0.0	0.0	0.0	-	-	-
<b>TS1</b>	-	-	-	16.2 (16.2)	10.0 (10.0)	10.4 (10.4)
<b>INT1</b>	-	-	-	-33.1	-34.5	-39.7
<b>TS2</b>	9.1 (42.2)	6.6 (41.1)	3.9 (43.6)	-	-	-
<b>INT2</b>	-	-	-	-18.5	-21.6	-25.1
<b>TS3</b>	-7.0 (11.5)	-9.5 (12.1)	-13.8 (11.4)	-	-	-
<b>INT3</b>	-16.7	-21.1	-24.8	-24.9	-29.5	-34.9
<b>TS4</b>	-7.8 (17.1)	-15.1 (14.4)	-13.6 (21.3)	-12.6 (12.3)	-20.3 (9.2)	-20.9 (14.0)
<b>INT4</b>	-	-	-	-25.3	-29.7	-32.2
<b>TS5</b>	-22.8 (2.5)	-25.8 (4.0)	-28.4 (3.8)	-	-	-
<b>TS6</b>	-14.1 (10.8)	-16.9 (12.6)	-21.4 (13.5)	-	-	-
<b>INT5</b>	-75.9	-71.2	-77.4	-63.1	-65.5	-64.7
<b>TS7</b>	-71.9 (3.9)	-70.4 (0.8)	-72.4 (5.0)	-59.8 (16.0)	-65.1 (6.1)	-60.7 (16.7)
<b>TS8</b>	-25.4 (7.7)	-26.7 (7.9)	-32.4 (7.3)	-20.6 (12.5)	-21.3 (13.2)	-27.7 (11.9)
<b>PROD</b>	-77.2	-75.5	-79.3	-57.8	-60.9	-59.8



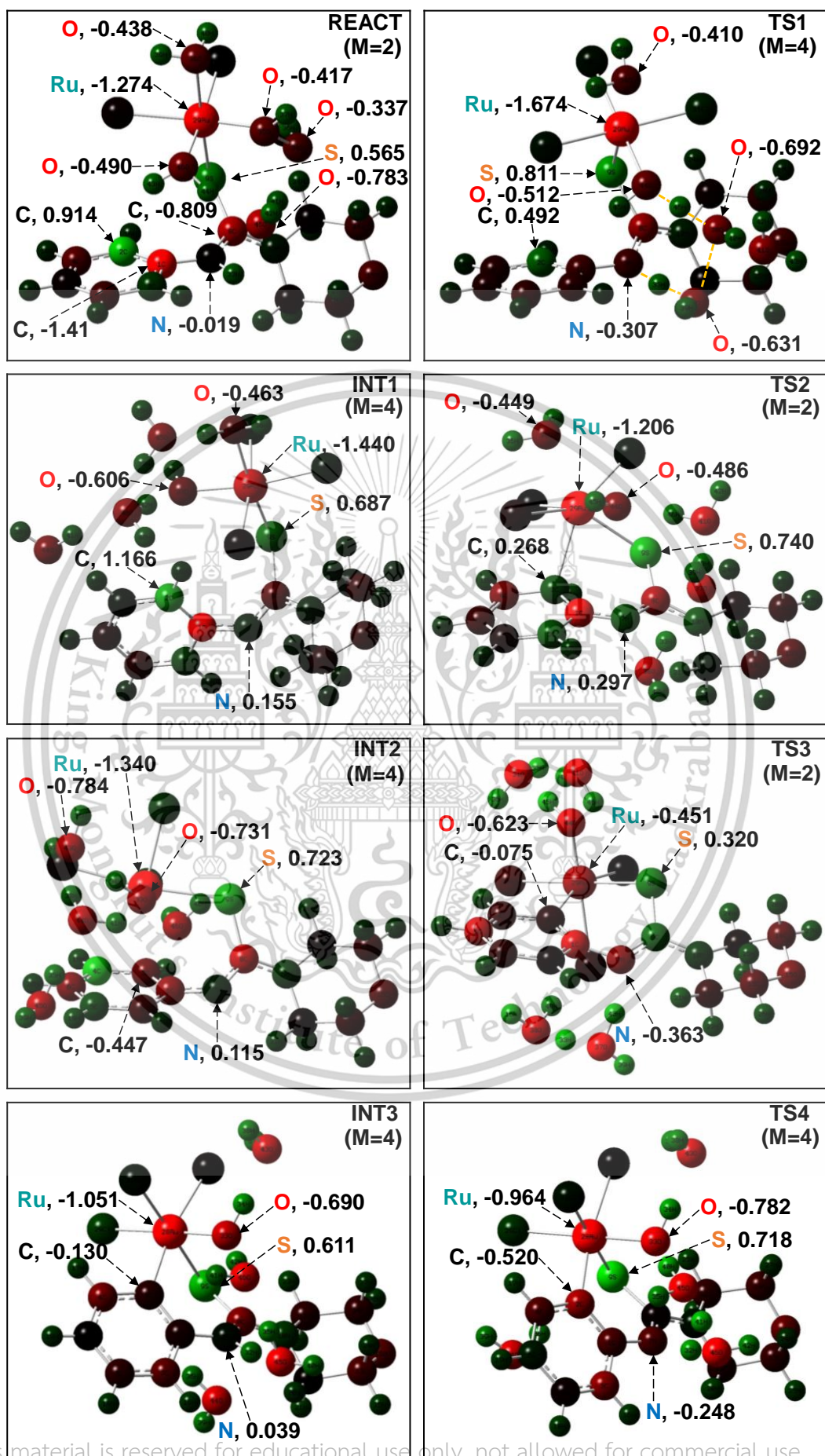
This material is reserved for educational use only, not allowed for commercial use.

Forbidden to modify the content, and cite the document when use.



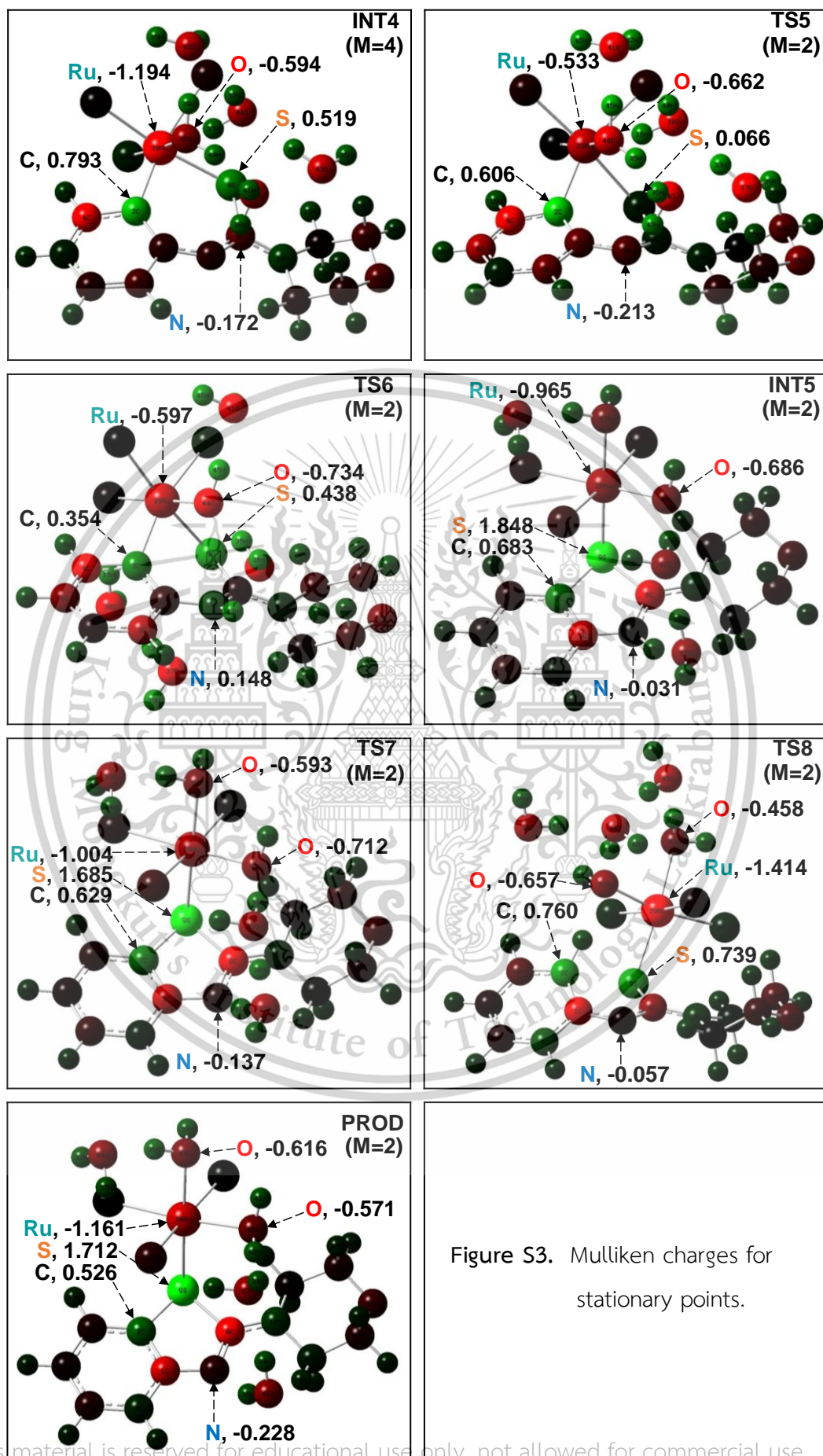
This material is reserved for educational use only, not allowed for commercial use.

Forbidden to modify the content, and cite the document when use.



This material is reserved for educational use only, not allowed for commercial use.

Forbidden to modify the content, and cite the document when use.



This material is reserved for educational use only, not allowed for commercial use.

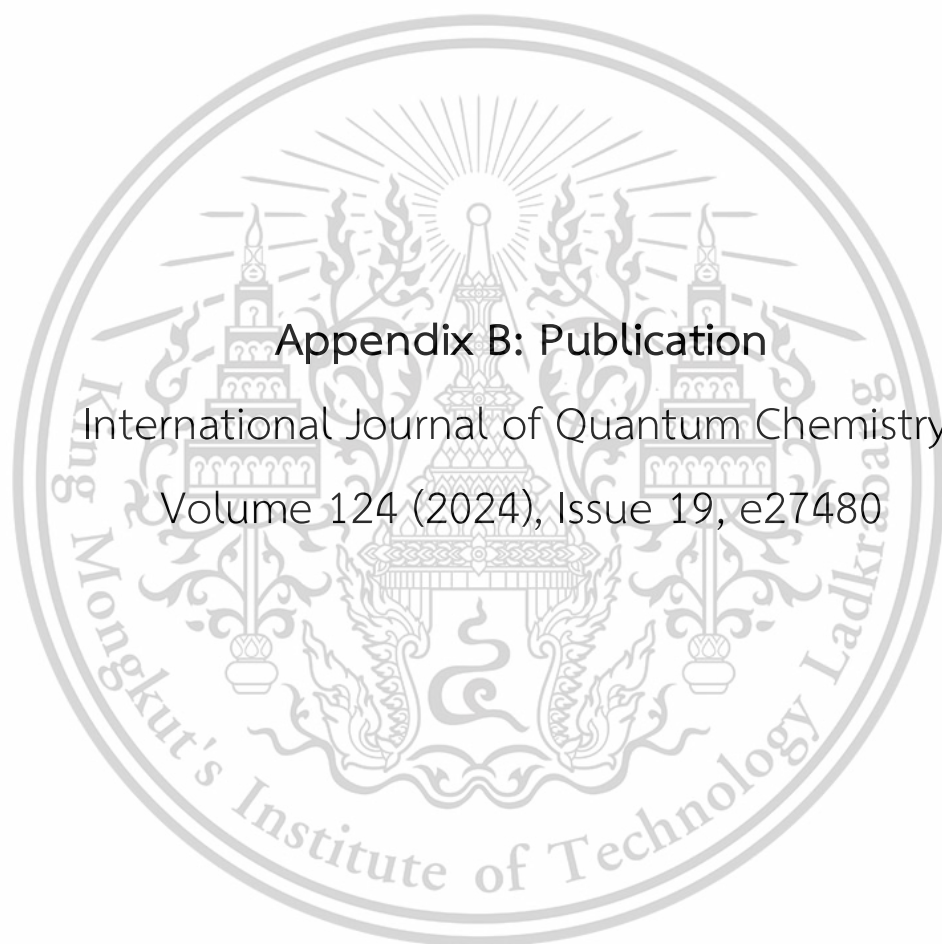
Forbidden to modify the content, and cite the document when use.

**Table S3.** Computed  $\Delta E$ ,  $\Delta G$  and  $\Delta E_{sp}$  energies obtained from the examination of the influence of electron-donating and electron-withdrawing groups substituent on the *ortho*-, *meta*-, *para*- positions. Energies are relative to the reactant and reported in kcal/mol. Values given in parenthesis are the barriers relative to their corresponding minima.

Structure	% Yield	TS1 M=4			INT1 M=4			TS2 M=2			TS8 M=2			PROD M=2		
		$\Delta E$	$\Delta G$	$\Delta E_{sp}$	$\Delta E$	$\Delta G$	$\Delta E_{sp}$	$\Delta E$	$\Delta G$	$\Delta E_{sp}$	$\Delta E$	$\Delta G$	$\Delta E_{sp}$	$\Delta E$	$\Delta G$	$\Delta E_{sp}$
9a	87	16.2 (16.2)	10.0 (10.0)	10.4 (10.4)	-33.1	-34.5	-39.7	9.1 (42.2)	6.6 (41.1)	3.9 (43.6)	-25.4 (7.7)	-26.7 (7.9)	-32.4 (7.3)	-77.2	-75.5	-79.3
9c	85	16.3 (16.3)	10.0 (10.0)	10.5 (10.5)	-41.1	-41.1	-47.5	5.9 (47.0)	5.2 (46.3)	0.8 (48.3)	-28.2 (13.0)	-27.8 (13.3)	-34.4 (13.0)	-76.4	-74.8	-78.7
9d	79	15.1 (15.1)	8.3 (8.3)	9.2 (9.2)	-28.6	-31.0	-35.6	9.7 (38.3)	7.1 (38.1)	4.3 (39.9)	-21.6 (7.0)	-22.0 (9.0)	-28.8 (6.8)	-78.0	-76.7	-80.1
9e	75	15.7 (15.7)	9.5 (9.5)	9.9 (9.9)	-35.1	-35.9	-41.7	8.6 (43.7)	6.8 (42.8)	3.4 (45.0)	-24.3 (10.7)	-24.2 (11.7)	-31.1 (10.6)	-77.0	-75.3	-79.1
9f	73	15.7 (15.7)	9.2 (9.2)	9.9 (9.9)	-34.3	-35.5	-40.9	8.1 (42.3)	6.4 (41.9)	2.7 (43.6)	-24.0 (10.3)	-24.2 (11.3)	-30.8 (10.1)	-77.0	-75.6	-79.2

Table S3. (continued)

Structure	% Yield	TS1 M=4			INT1 M=4			TS2 M=2			TS8 M=2			PROD M=2		
		$\Delta E$	$\Delta G$	$\Delta E_{sp}$	$\Delta E$	$\Delta G$	$\Delta E_{sp}$	$\Delta E$	$\Delta G$	$\Delta E_{sp}$	$\Delta E$	$\Delta G$	$\Delta E_{sp}$	$\Delta E$	$\Delta G$	$\Delta E_{sp}$
9g	67	15.7 (15.7)	9.2 (9.2)	10.0 (10.0)	-34.0	-35.3	-40.7	8.1 (42.1)	6.6 (41.9)	3.0 (43.7)	-23.8 (10.1)	-24.1 (11.1)	-30.7 (10.0)	-77.2	-75.8	-79.2
9i	91	15.8 (15.8)	9.5 (9.5)	10.1 (10.1)	-32.5	-34.1	-39.2	4.0 (36.5)	1.9 (36.0)	-1.1 (38.1)	-26.4 (6.2)	-26.6 (7.4)	-33.8 (5.4)	-77.0	-75.2	-79.1
9o	78	17.2 (17.2)	14.4 (14.4)	12.1 (12.1)	-32.7	-34.0	-39.5	8.8 (41.5)	7.5 (41.6)	3.5 (42.9)	-22.7 (10.0)	-22.9 (11.1)	-29.9 (9.6)	-77.1	-75.7	-79.2
9n	64	17.0 (17.0)	14.0 (14.0)	11.3 (11.3)	-32.8	-34.6	-39.3	8.8 (41.6)	7.1 (41.7)	3.6 (43.0)	-22.8 (10.1)	-23.2 (11.4)	-29.6 (9.8)	-77.0	-76.1	-78.9
9p	55	18.4 (18.4)	15.5 (15.5)	12.8 (12.8)	-34.1	-35.5	-40.5	7.3 (41.4)	6.4 (41.9)	2.4 (42.9)	-24.4 (9.8)	-24.5 (11.0)	-31.1 (9.4)	-78.4	-77.1	-80.1



## Appendix B: Publication

International Journal of Quantum Chemistry,  
Volume 124 (2024), Issue 19, e27480

This material is reserved for educational use only, not allowed for commercial use.

Forbidden to modify the content, and cite the document when use.

## RESEARCH ARTICLE

# Computational Investigation of the Ru-Mediated Preparation of Benzothiazoles From *N*-Arylthioureas: Elucidation of the Reaction Mechanism and the Origin of Differing Substrate Reactivity

Pacharaporn Krawmanee<sup>1</sup> | M. Paul Gleeson<sup>2</sup>  | Duangkamol Gleeson<sup>1</sup> 

<sup>1</sup>Applied Computational Chemistry Research Unit & Department of Chemistry, School of Science, King Mongkut's Institute of Technology Ladkrabang, Bangkok, Thailand | <sup>2</sup>Department of Biomedical Engineering, School of Engineering, King Mongkut's Institute of Technology Ladkrabang, Bangkok, Thailand

Correspondence: Duangkamol Gleeson (duangkamol.g@kmitl.ac.th)

Received: 14 June 2024 | Revised: 27 August 2024 | Accepted: 29 August 2024

Funding: This work was supported by King Mongkut's Institute of Technology Ladkrabang (KMITL) (KRIS-KREF046402&RA/TA-2562-M017), and Thailand Science Research and Innovation (TSRI) (FRB60065/0258-RE-KRIS/FP66/08).

Keywords: benzothiazoles | DFT | mechanism | *N*-arylthiourea | ruthenium catalyst

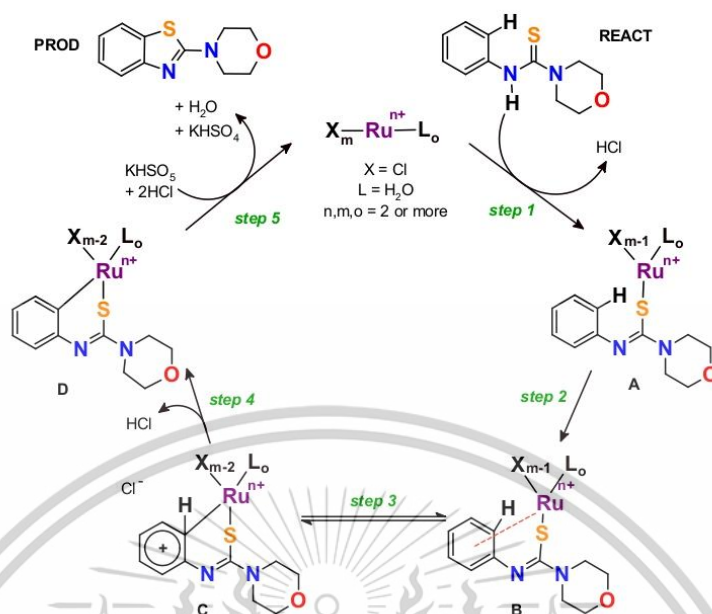
## ABSTRACT

Synthesis of novel benzothiazoles via intramolecular C—S bond formation reactions is increasingly being explored since they have been found in a wide range of natural products and pharmaceutical agents. Sharma et al. reported the ruthenium-catalyzed preparation of novel benzothiazole derivatives from *N*-arylthiourea precursors, with a range of reaction yields and selectivity being observed. We have employed a density functional theory-based computational model to investigate the reaction mechanism leading to the benzothiazole product and help uncover the origin of the differing experimental yields and substrate specificities. We proposed a modified mechanistic scheme where the rate-determining step to be the synchronized breaking of the peroxide bond of the oxidizing agent with the concomitant proton-coupled electron transfer from the haloarene urea and a Ru-bound water molecule, not electrophilic Ru—C bond activation. Evidence for this being the rate-determining step is (a) the barrier is consistent with a lack of kinetic isotope effects associated with the *ortho*-H atom and (b) the computed rate-determining barriers for 10 *N*-arylthiourea substrates show good correlation with the observed yield.

## 1 | Introduction

Benzothiazole is a privileged heterocyclic scaffold with considerable interest based on observed anticancer, antimicrobial, anti-inflammatory, anti-viral, and other activities. [1–6] As such, there has been significant effort in exploring new ways to prepare molecules of this class. [7–10] This includes intramolecular electrophilic substitution of thiobenzanilides, condensation of 2-aminothiophenols with carboxylic acids or intramolecular

C—S bond formation with *ortho*-haloarenes. [11, 12] Progress toward the development of transition metal-catalyzed reactions for the construction of C—S bonds has been challenging compared to other carbon–heteroatom coupling types (C—C or C—N) [13–16] due to difficulties related to efficiency and selectivity. However, these problems have largely been overcome through the identification of new transition metal catalysts in conjunction with C—H bond functionalization [17–21].



**SCHEME 1** | Ru-catalyzed preparation of 2-aminobenzothiazoles. Adapted with permission from Sharma et al. [17], Copyright 2024 American Chemical Society.

Sharma et al. [17] reported an efficient route to the preparation of 2-aminobenzothiazoles from *N*-arylthioureas utilizing a Ru-catalyzed intramolecular C—S coupling reaction with oxone acting as the reducing agent (Scheme 1). Screening with a diverse set of *N*-arylthioureas showed the reaction had a broad scope, with electron-donating substituents generally showing greater reactivity. They proposed a five-step mechanism based on kinetic isotope effect (KIE) data that showed the more conventional direct C—H bond activation was not rate determining (step 4). They proposed an electrophilic Ru-mediated rate-determining step consistent with the KIE data where the *ortho* carbon transitions from  $sp^2$  to  $sp^3$  (step 3), but does not involve C—H bond activation. Limited DFT calculations exploring the reaction (steps 3 and 4) were undertaken, predicting the rate-determining barrier to be 26.5 kcal/mol.

Computational methods have proven extremely useful in elucidating experimental phenomenon associated with Ru-based catalytic systems. [22–25] Therefore, we have applied such methods to shed further light on the mechanistic proposals associated with the ruthenium-catalyzed formation of benzothiazoles from *N*-arylthioureas. We expand on the DFT reported by Sharma et al. [17] by employing a larger octahedral  $RuCl_3$ -based DFT model, [22–24] as opposed to the tetrahedral configuration in the former, and also include the required oxidizing agent. This more complete model can therefore be employed to investigate the five distinct steps in the proposed mechanism in Scheme 1, as well as other possibilities. Critically, we also consider the effect of spin on the Ru (II/III) system on the structures and energetics [24].

The goals of this work are to (a) validate the current mechanistic proposal or revise it (b) confirm the rate-determining step, and (c) determine whether the proposed mechanism can account for the experimental yields of the diverse substrates, which range from 55% to 91%. Such understanding should help in the design of future catalysts for the production of future, novel benzothiazole derivatives.

## 2 | Computational Methods

A model of the most effective catalyst identified by Sharma et al. ( $RuCl_3$ , 89%), [17] was first created. An octahedral complex [26–28] consisting of  $RuCl_3$ , *N*-arylthiourea, and three water molecules was generated, consistent with Scheme 1. The peroxide oxidizing agent potassium monopersulfate (oxone) was modeled with hydrogen peroxide for reasons of computational efficiency. [29, 30] A second model, noncatalyzed reaction, consisting of the substrate, hydrogen peroxide, and water was also studied for comparison.

All calculations were performed using the Gaussian 16 program [31] using the UB3PW91 functional, [32] a common method employed in Ru-based studies. [33, 34] Geometry optimizations were conducted using the 6-31+G\*\* basis set for H, N, O, and S atoms and using the LANL2DZ for Ru ( $\Delta E$ ). [22, 35–37] Single-point energies ( $\Delta E_{sp}$ ) were then determined using 6-311++G\*\* basis set for H, N, O, and S atoms, and def2-TZVP for Ru. [38, 39] The existence of doublet and quartet spin states (M) was investigated since it has been shown that benzothiazole

synthesis can follow a free radical process (Table S1). [40, 41] Stationary points displaying spin contamination were excluded (i.e.,  $\langle S^2 \rangle \geq 5\%$  from the expected value).

Stationary points were confirmed from an analysis of their vibrational frequencies. Transition states displayed a single vibration with a negative eigenvalue while minima showed only positive values. Free energies ( $\Delta G$ ) were calculated using the zero-point energies and thermal corrections were calculated at 298.15 K. Finally, single-point energies using a polarizable continuous solvent model consisting of dichloroethane were also determined ( $\Delta E_{SP}$  PCM).

### 3 | Results

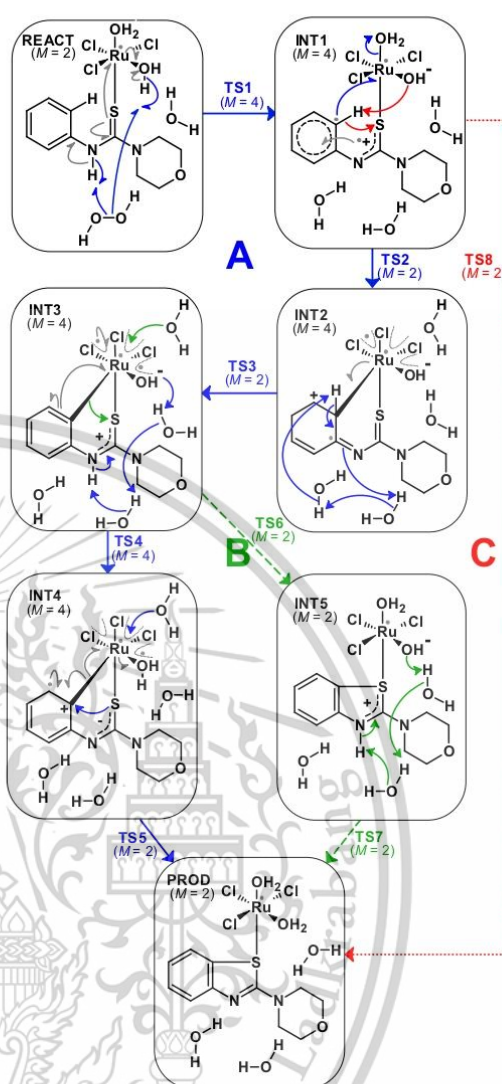
The chemical structures of stationary points obtained on the mechanistic pathway leading to *N*-phenylmorpholine-4-carbothioamide are illustrated in Scheme 2 and Figure 1. The corresponding energies are given in Table 1. Since a strong correlation ( $r^2 \geq 0.99$ ) between the  $\Delta E$ ,  $\Delta E_{sp}$ , and  $\Delta G$  values was observed. The effect of the solvent on the energetics was also found to be negligible (Figure S1). We henceforth refer to the  $\Delta E$  values only. The Mulliken charges and spin densities are reported in Figures S2 and S3, respectively.

The starting structure (REACT) in our calculations consists of an octahedral Ru complex formed by *N*-arylthiourea and  $Ru^{(III)}Cl_3(H_2O)_2$  in a doublet spin state ground state (Scheme 2). A stable quartet state was not observed. The Ru—S distance is found to be 2.39 Å, while the Ru—Cl and Ru—O are found to be  $\sim 2.3$  and  $\sim 2.2$  Å, respectively (Figure 1). Analysis of the spin density shows the radical located on the metal center (Figure S3). Also, present in the starting model are hydrogen peroxide and a third water molecule that has been displaced by the *N*-arylthiourea on its association with Ru. The difference in energy between the Ru-water complex and Ru-*N*-arylthiourea complex is 3.4 kcal/mol in favor of the former.

In Scheme 2, we describe the key changes in charge and spin density over the course of the chemical reaction. We have attempted to show the complex changes in bonding and the internal movement of electrons using single (homolytic) and double-headed arrows (heterolytic). Ru remains in the  $d^5$  (+3 oxidation state) over the course of the reaction, however significant charge transfer occurs, onto the *N*-arylthiourea atoms undergoing hybridization change, the peroxide as the O—O bond breaks, or its direct ligands ( $H_2O$  and Cl). The required (a) H atom or  $H^+$  proton transfers and (b) oxidative electron transfers in many instances occur in a concerted fashion via different centers and can be considered in the broad class of proton-coupled electron transfer (PCET) processes. [42, 43] The movement of bonding electrons in Scheme 2 is colored according to the three distinct reaction pathways that were found, while any internal electron transfer that may also be required are denoted using gray arrows.

#### 3.1 | Pathway A

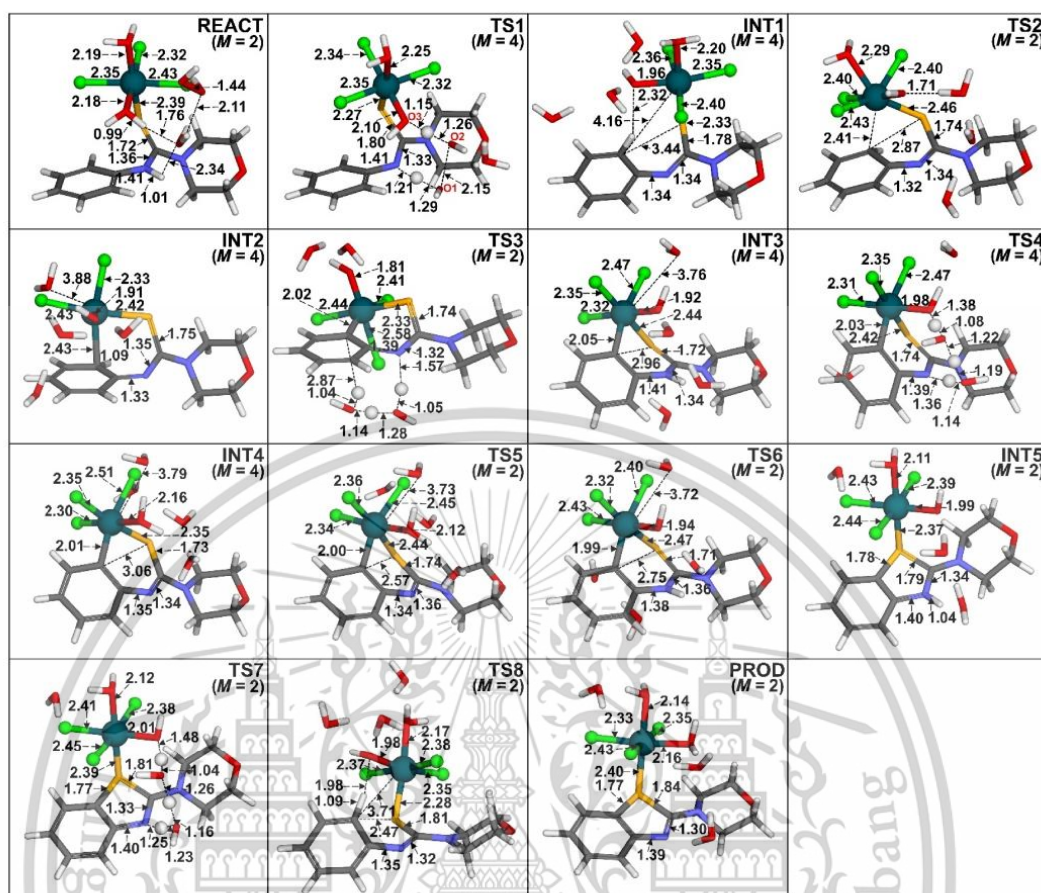
Mechanistic pathway A in Scheme 2 is equivalent to the mechanistic process described by Sharma et al. in Scheme 1. This process involves the generation of an electrophilic *ortho*



**SCHEME 2** | Illustration of the discrete steps involved in the production of 2-aminobenzothiazole from *N*-arylthiourea. Arrows indicate the approximate movement of electrons based on Mulliken charge and spin densities obtained for the stationary points.

phenyl carbon via Ru—C bond formation and reduction of hydrogen peroxide.

The reaction proceeds from the reactant (REACT) with the concomitant deprotonation by  $H_2O_2$  of both the thiourea nitrogen and a Ru-bound water molecule. This leads to the breaking of the peroxide bond and results in the first reaction intermediate (INT1). This structure is equivalent to **A** reported by Sharma et al. in Scheme 1.



**FIGURE 1** | Optimized geometries obtained in the production of 2-aminobenzothiazole from *N*-arylthiourea. Key distances are illustrated in Å. Transition state structures are as follows: TS1 (PCET); TS2 (Ru—C bond formation); TS3 (deprotonation); TS4 (PCET); TS5 (C—S cross-coupling); TS6 (C—S ring closure); TS7 (proton transfer); and TS8 (concerted C—S ring closure).

In the transition state (TS1), the peroxide O—O bond has elongated from 1.44 Å in the REACT to 2.15 Å and preferentially exists in the quartet spin state (3 unpaired electrons). Natural bond orbital (NBO) analysis indicates a homolytic process with the evolving radicals being located on the Ru and both peroxide oxygen atoms at the transition state (Figure S3). The two transferring protons have O—H distances of  $\sim 1.3$  Å indicating a PCET event where two electrons have transferred prior (Figure 1). INT1 also preferentially adopts a quartet spin state with the radical electrons being confined to the Ru atom, the substrate phenyl ring, and the thiourea moiety (Scheme 2). The barrier to reaction is predicted to be 16.2 kcal/mol (Table 1) while the intermediate is  $-33.1$  kcal/mol lower in energy than the REACT.

Ru—C bond formation is observed in TS2. This requires the removal of Ru-coordinated water molecules in the process. TS2 sees the Ru—C distance decreasing from 4.16 Å in INT1 to 2.41 Å at the transition state (Figure 1). Simultaneously, the

Ru—OH<sub>2</sub> bond elongates from 2.20 to 2.29 Å in INT1 and TS2, respectively. TS2 proceeds solely via a doublet spin state with a barrier of 42.2 kcal/mol (Table 1). In comparison, the values reported Ru—C barrier to formation by Sharma et al. [17] was 26.5 kcal/mol. However, the results are not directly comparable as a different model system is used, proton transfer from the *ortho* carbon can also occur in the latter step unlike here, and the stationary point spin states are not reported. In our case, the large distance (4.16 Å) of the *ortho* carbon hydrogen from the Ru-bound OH<sup>-</sup> makes direct proton transfer impossible in conjunction with Ru—C bond formation.

The resulting intermediate (INT2) exists in the quartet state and has an energy of  $-18.5$  kcal/mol relative to the reactant, but 14.6 kcal/mol is less stable than that of the previous INT1. NBO analysis shows the existence of two radicals on the Ru-center (Ru-plus directly bonded atoms) and one delocalized within the  $\pi$  molecular orbitals (MO) of the thiourea substrate. This

**TABLE 1** | Computed  $\Delta E$ ,  $\Delta G$ , and  $\Delta E_{sp}$  energies of stationary points listed in Scheme 2. Energies are reported in kcal/mol and relative to the reactant. Absolute barriers heights are in parenthesis.

ID	M	$\Delta E$	$\Delta G$	$\Delta E_{sp}$
REACT	2	0.0	0.0	0.0
TS1	4	16.2	10.0	10.4
INT1	4	-33.1	-34.5	-39.7
TS2	2	9.1 (42.2)	6.6 (41.1)	3.9 (43.6)
INT2	4	-18.5	-21.6	-25.1
TS3	2	-7.0 (11.5)	-9.5 (12.1)	-13.8 (11.4)
INT3	4	-24.9	-29.5	-34.9
TS4	4	-12.6 (12.3)	-20.3 (9.2)	-20.9 (14.0)
INT4	4	-25.3	-29.7	-32.2
TS5	2	-22.8 (2.5)	-25.8 (4.0)	-28.4 (3.8)
TS6	2	-14.1 (10.8)	-16.9 (12.6)	-21.4 (13.5)
INT5	2	-75.9	-71.2	-77.4
TS7	2	-71.9 (3.9)	-70.4 (0.8)	-72.4 (5.0)
TS8	2	-25.4 (7.7)	-26.7 (7.9)	-32.4 (7.3)
PROD	2	-77.2	-75.5	-79.3

structure corresponds to structure **C** predicted by Sharma et al. in Scheme 1. Note structure **B** does not exist here due to the use of an octahedral  $RuCl_3$  model.

TS3 involves the deprotonation of the  $sp^3$  hybrid *ortho* carbon of the substrate phenyl ring by the urea nitrogen, catalyzed through proton shuttling from the two water molecules generated from the reduction of peroxide and one liberated on Ru—C bond formation. The proton shuttling event proceeds via a doublet spin state with the re-establishment of the aromatic ring through further electron re-arrangement, that is, PCET. The resulting stationary point (INT3) exists in the quartet state with radicals located on the Ru-center. The structure is 6.4 kcal/mol more stable than INT2 and -24.9 kcal/mol lower in energy than the REACT.

For INT3 to form the product, proton transfer and ring closure steps are required. As Sharma et al. proposed ring closure as the final step, we therefore investigate proton transfer to give INT4 next (Scheme 2, Pathway A). TS4 is another PCET event that proceeds preferentially via a quartet state with a high barrier of 12.3 kcal/mol. A proton is shuttled from the protonated thiourea to the Ru-bound hydroxide via two water molecules. At the transition state, a hydronium ion exists to facilitate the transfer with a corresponding N—H distance of 1.36 Å and O—H distance of 1.38 Å (Figure 1).

INT4 exists preferentially in the quartet spin state with two radicals located on the Ru-center. Mulliken charge analysis shows the existence of a positive charge on the *ortho* carbon of the six-membered ring along with a delocalized radical within the substrate  $\pi$  system. This structure corresponds to a highly electrophilic carbon envisaged by Sharma et al. denoted **D** in Scheme 1. The structure is just 0.4 kcal/mol lower in energy than INT3.

The final step in the catalytic process involves C—S cross-coupling and the re-coordination of a water molecule with ruthenium to give an octahedral configuration (Scheme 2). The C—S electrophile-nucleophile distance in TS5 is 2.57 Å, reducing from 3.06 Å in INT4 (Figure 1). The doublet structure has a single unpaired electron of Ru and results in a relatively low barrier of 2.5 kcal/mol.

The regeneration of aromaticity in the benzothiazole product (PROD) results in a structure with an energy of -77.2 kcal/mol lower than the REACT. The octahedral Ru-complex has a doublet spin state with the unpaired electron located on the Ru atom.

### 3.2 | Pathway B

Pathway B in Scheme 2 differs from Pathway A at the point of INT3. This is because ring closure could occur prior to the required proton transfer step, giving rise instead to TS6.

In this structure, the C—S bond distance was marginally longer than that found in the comparable TS5, 2.75 versus 2.57 Å. As with TS5, the structure exists preferentially in a doublet state. However, the barrier to reaction for TS6 is found to be 10.8 kcal/mol due to the reduced electrophilicity of the six-membered ring as can be seen from the Mulliken charge distributions ( $C_{ortho}$  charges of 0.606 and 0.354, respectively, Figure S2).

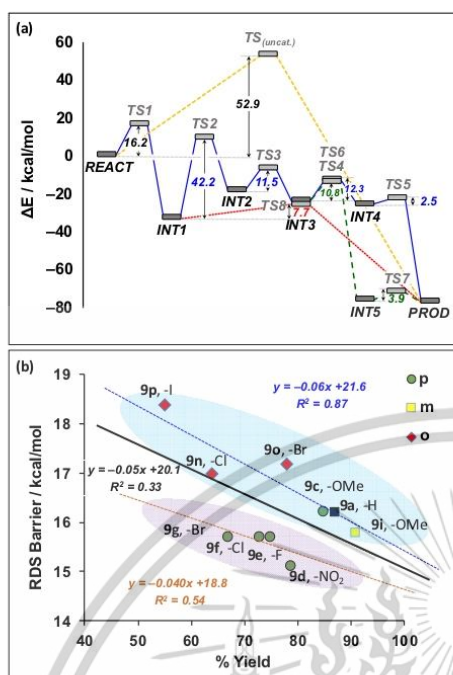
INT5 forms following C—S cross-coupling and coordination of one water molecule to Ru. The stationary point adopts a doublet electronic spin state and is again highly exothermic due to the re-aromatization of the phenyl ring, being -75.9 kcal/mol lower in energy than the REACT. Proton transfer completes the process giving the benzothiazole product. TS7 sees a proton shuttle from the thiourea nitrogen to the Ru-bound hydroxide. The barrier is just 3.9 kcal/mol.

As can be seen from Figure 2a, the rate-determining step on both Pathway A (blue) and Pathway B (green) is TS2 corresponding to Ru—C bond formation. Pathway B is marginally more favored over Pathway A given TS6 is lower than TS4 by 1.5 kcal/mol. However, based on the single point energies, the free energy barrier is found to be -3.4 kcal/mol in favor of the former suggesting that both potentially can complete.

### 3.3 | Pathway C

A third mechanistic possibility was investigated whereby the direct formation of a Ru—C bond is not involved in increasing the electrophilicity of the substrate. Indeed, this is the rate-determining step in both Pathways A and B with a barrier of 42.2 kcal/mol (Table 1 and Figure 2a).

Pathway C (red) starts from INT1 formed from the reduction of hydrogen peroxide, with a modest barrier of 16.2 kcal/mol. From INT1, we identified an alternative transition state whereby the concerted transfer of the *ortho* carbon proton to the Ru-bound hydroxide and C—S bond formation can occur (TS8). The C—S distance at the transition state reduces from 3.44 Å in INT1



**FIGURE 2** | (a) Computed reaction energy profile corresponding to the production of 2-aminobenzothiazole from *N*-arylthiourea and (b) a comparison of TS1 ( $M=4$ ) energy barriers and %yield, obtained for 9a and the substituents on the *ortho*-, *meta*-, and *para*-positions.

to 2.47 Å in TS8. This is noticeably shorter than the distance observed for the other ring closure transition states (TS5 and TS6) at 2.57 and 2.75 Å, respectively. The PCET process occurs after the transition state has been traversed as can be seen from the short C—H bond distance of 1.09 Å and long O—H interaction distance of 1.98 Å. The energy barrier for this doublet spin transition state was found to be just 7.7 kcal/mol.

## 4 | Discussion

### 4.1 | Probable Reaction Mechanism

We have investigated three possible mechanistic pathways leading to the conversion of *N*-arylthioureas to 2-aminobenzothiazoles using  $\text{RuCl}_3$ -based catalytic system. Two of the processes involve the direct formation of an Ru—C bond to increase the electrophilicity of the *ortho* carbon of the aryl ring (pathways A and B), originally proposed by Sharma et al., and pathway B involves only charge transfer effects. The rate-determining step for both pathways A and B is TS2. However, for pathway C it is TS8.

TS8 is considerably lower in energy than the alternative TS2 which is also derived from INT1. Indeed, TS2 is the rate-determining step for Pathways A and B, suggesting that

a mechanism involving direct Ru—C bond is implausible. Instead, it is likely that Ru increases the electrophilicity of the phenyl *ortho* carbon and the nucleophilicity of the thiolate via electron/charge transfer only. This means that the irreversible oxidative step (TS1, 16.2 kcal/mol) is the rate-determining step. Indeed, once INT1 is formed, the reverse barrier to reaction is 49.3 kcal/mol. Thus, the subsequent traversal of TS8 to form the benzothiazole product is facile. In addition, while Sharma et al. [17] found that the radical scavenging agent TEMPO does not affect the outcome of the reaction, given the low barrier to reaction for the quartet INT1 state, it is plausible that insufficient time exists for it to undergo reaction with the radical inhibitor given the low barrier to forward reaction.

Another important consideration is that KIE ( $k_H/k_D$ ) studies were performed using a substrate with a deuterated *ortho* aryl carbon. However, no KIE was observed confirming that the transfer of *ortho* aryl carbon proton (i.e., TS8 or TS3) cannot be involved in the rate-determining step. Indeed, this was a key element leading to Sharma et al. proposing their original mechanism involving a direct Ru—C bond formation (i.e. via TS2).

Our findings are broadly in agreement with the proposals of Sharma et al., yet it appears the role of ruthenium is to increase the electrophilicity of the aryl ring not through direct C—Ru bond formation, but rather through charge transfer effects. We find that the oxidation of the peroxide bond (TS1) followed by rapid proton transfer and ring closure (TS8) is (a) consistent with the KIE and (b) energetically much more favorable than the former.

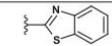
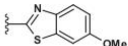
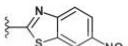
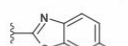
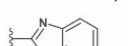
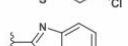
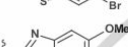


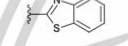
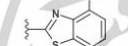
### 4.2 | Correlation of Yield vs. RDS Barrier

To assess the validity of our new mechanistic proposal, we investigated whether there was a correlation between our predicted rate-determining barrier (TS1) and the yield for 10 *N*-arylthioureas (9c-9g, 9i, 9n-9p) which display yields ranging from 91% to 55% (Table 2). These cover a range of electron-donating/neutral (MeO, H) and withdrawing groups (F, Cl, Br, I, and  $\text{NO}_2$ ). The substituents also cover the *ortho*-, *meta*-, and *para*-positions of the arylthioureas.

A plot of the TS1 energy barriers versus the reported benzothiazole reaction yields is reported in Figure 2b. A relatively weak correlation is observed for all 10 molecules as can be seen by the  $R^2$  of 0.33. The observation can be explained by the electron-donating substituents providing greater stabilization of the evolving positive charge on the aryl ring at TS1, leading to an increased yield. Note that we also assessed the correlation with the energy barriers of TS2, however, no correlation was found ( $R^2 = 0.0$ ).

While the overall correlation between the %yields and TS1 barrier is relatively weak, we find that it markedly improves when the data are broken down by the substituent type and/or location. When exemplars with *para*-substituted electron-withdrawing substituents are excluded,  $R^2 = 0.87$  is observed (Figure 2b). The latter set (9d, 9e, 9f, and 9g) is found to display much lower yields than would be expected based on their generally low barriers. In addition, the correlation within the excluded group is also much improved ( $R^2 = 0.54$ ).

**TABLE 2** | Computed energies obtained from the examination of the influence of electron-donating and electron-withdrawing groups substituent on the *ortho*-, *meta*-, and *para*- positions. Energies are relative to the reactant and reported in kcal/mol.

ID	Structure	% yield	TS1 ( <i>M</i> = 4)	PROD ( <i>M</i> = 2)
9a		87	16.2	-77.2
9c		85	16.2	-76.4
9d		79	15.1	-78.0
9e		75	15.7	-77.0
9f		73	15.7	-77.0
9g		67	15.7	-77.2
9i		91	15.8	-77.0
9i*		—	16.2	-76.4
9o		78	17.2	-77.1
9n		64	17.0	-77.0
9p		55	18.4	-78.4

\*An alternative product of 9i that is not observed experimentally.

The discrepancy between the two identified groups would suggest the model employed here does not describe some key experimental aspects of the real system. Indeed, the sterically less hindered *para*-substituted halides (9e, 9f, and 9g) potentially undergo side reactions with catalytic metals such as ruthenium and palladium resulting in their lower than predicted yields. [27, 44–46] Additionally, the lower than predicted yields for 9d could be due to an effect noted by Sharma et al. [17] that the nitro group can potentially coordinate with Ru directly, thus leading to reduced reactivity.

Finally, it is interesting to note that the *meta*-methoxy substituent of 9i can potentially result in two isomers, denoted 9i and 9i\* in Table 2. Our calculations clearly show that 9i is kinetically and thermodynamically preferred as is expected given 9i\* is not reported under experimental conditions.

## 5 | Conclusions

In summary, we report a detailed DFT study exploring the mechanism of formation of a novel class of benzothiazoles via intramolecular C—S bond formation catalyzed via an electrophilic ruthenation pathway.

Our results are in general agreement with Sharma et al. [17] that ruthenium acts to increase the electrophilicity of the aryl ring of the *N*-arylthioureas. However, our results suggest this is limited to charge transfer effects and does not necessitate Ru—C bond formation. We find that the initial oxidative step (TS1) is rate determining and that this is consistent with the observed kinetic isotope effects. Additionally, analysis of the relationship between the experimentally reported benzothiazole reaction yields and our predicted RDS barriers shows a good correlation giving us further confidence in our findings.

In summary, the results reported here are in good agreement with the experimental data reported on this reaction, showing the value of such calculations in synthetic organic chemistry. We show that such calculations could prove useful to rapidly explore the scope of such reactions, predicting reaction selectivity or the potential outcomes with new, untested reagents.

## Author Contributions

The manuscript was written through the contributions of all authors. All authors have given approval to the final version of the manuscript.

## Acknowledgments

DG would like to acknowledge financial support from King Mongkut's Institute of Technology Ladkrabang (KMITL) (KRIS-KREF046402) and the Thailand Science Research and Innovation (TSRI), and the National Science Research and Innovation Fund (NSRF) (FRB660065/0258-RE-KR IS/FF66/08). PK would like to acknowledge support by the School of Science, KMITL, (RA/TA-2562-M017).

## Data Availability Statement

All optimized coordinates have been included as a mol2 file and supporting information file.

## References

1. P. C. Sharma, A. Sinhar, A. Sharma, H. Rajak, and D. P. Pathak, "Medicinal Significance of Benzothiazole Scaffold: An Insight View," *Journal of Enzyme Inhibition and Medicinal Chemistry* 28 (2013): 240–266.
2. M. Singh and S. K. Singh, "Benzothiazoles: How Relevant in Cancer Drug Design Strategy?" *Anti-Cancer Agents in Medicinal Chemistry* 14 (2014): 127–146.
3. A. Kamal, M. A. H. Syed, and S. M. Mohammed, "Therapeutic Potential of Benzothiazoles: A Patent Review (2010–2014)," *Expert Opinion on Therapeutic Patents* 25 (2015): 335–349.
4. Y. I. Asiri, A. Alsayari, A. B. Muhsinah, Y. N. Mabkhot, and M. Z. Hassan, "Benzothiazoles as Potential Antiviral Agents," *Journal of Pharmacy and Pharmacology* 72 (2020): 1459–1480.
5. A. Irfan, F. Batool, S. A. Zahra Naqvi, et al., "Benzothiazole Derivatives as Anticancer Agents," *Journal of Enzyme Inhibition and Medicinal Chemistry* 35 (2020): 265–279.
6. E. N. Djuidje, R. Barbari, A. Baldisserotto, et al., "Benzothiazole Derivatives as Multifunctional Antioxidant Agents for Skin Damage: Structure–Activity Relationship of a Scaffold Bearing a Five-Membered Ring System," *Antioxidants* 11, no. 2 (2022): 407.
7. C. Chen and Y.-J. Chen, "Liquid-Phase Synthesis of 2-Substituted Benzimidazoles, Benzoxazoles and Benzothiazoles," *Tetrahedron Letters* 45 (2004): 113–115.

8. J. R. Mali, D. V. Jawale, B. S. Londhe, and R. A. Mane, "An Efficient Green Protocol for the Synthesis of 2-Aryl Substituted Benzothiazoles," *Green Chemistry Letters and Reviews* 3 (2010): 209–212.
9. R. Yella, S. Murru, A. R. Ali, and B. K. Patel, "Arylthioureas With Bromine or Its Equivalents Gives No 'Hugerschoff' Reaction Product," *Organic & Biomolecular Chemistry* 8 (2010): 3389–3393.
10. M. Bursch, J.-M. Mewes, A. Hansen, and S. Grimme. "Best-Practice DFT Protocols for Basic Molecular Computational Chemistry," *Angew. Chemie. Int. Ed.* 134, no. 42 (2022): e202205735.
11. Y. Cheng, Q. Peng, W. Fan, and P. Li, "Room-Temperature Ligand-Free Pd/C-Catalyzed C–S Bond Formation: Synthesis of 2-Substituted Benzothiazoles," *Journal of Organic Chemistry* 79 (2014): 5812–5819.
12. S. K. Sahoo, A. Banerjee, S. Chakraborty, and B. K. Patel, "Regioselective Intramolecular Arylthiolations by Ligand Free Cu and Pd Catalyzed Reaction," *ACS Catalysis* 2 (2012): 544–551.
13. L. L. Hegedus and C. J. Pereira, "Reaction Engineering for Catalyst Design," *Chemical Engineering Science* 45 (1990): 2027–2044.
14. C. Liu, H. Zhang, W. Shi, and A. Lei, "Bond Formations Between Two Nucleophiles: Transition Metal Catalyzed Oxidative Cross-Coupling Reactions," *Chemical Reviews* 111 (2011): 1780–1824.
15. W. Shi, C. Liu, and A. Lei, "Transition-Metal Catalyzed Oxidative Cross-Coupling Reactions to Form C–C Bonds Involving Organometallic Reagents as Nucleophiles," *Chemical Society Reviews* 40 (2011): 2761–2776.
16. M. L. Louillat and F. W. Patureau, "Oxidative C–H Amination Reactions," *Chemical Society Reviews* 43 (2014): 901–910.
17. S. Sharma, R. S. Pathare, A. K. Maurya, et al., "Ruthenium Catalyzed Intramolecular C–S Coupling Reactions: Synthetic Scope and Mechanistic Insight," *Organic Letters* 18 (2016): 356–359.
18. C. Shen, P. Zhang, Q. Sun, S. Bai, T. S. Hor, and X. Liu, "Recent Advances in C–S Bond Formation via C–H Bond Functionalization and Decarboxylation," *Chemical Society Reviews* 44 (2015): 291–314.
19. A. H. Romero, "Fused Heteroaromatic Rings via Metal-Mediated/Catalyzed Intramolecular C–H Activation: A Comprehensive Review," *Topics in Current Chemistry* 377 (2019): 21.
20. H. H. Al Mamari, B. Štefane, and H. B. Žugelj, "Metal-Catalyzed C–H Bond Functionalization of Phenol Derivatives," *Tetrahedron* 76 (2020): 130925.
21. M. C. Henry, V. M. Abbinante, and A. Sutherland, "Iron-Catalyzed Regioselective Synthesis of 2-Arylbenzoxazoles and 2-Arylbenzothiazoles via Alternative Reaction Pathways," *European Journal of Organic Chemistry* 2020 (2020): 2819–2826.
22. Z. Zhou, S. Chen, Y. Hong, et al., "Non-C2-Symmetric Chiral-at-Ruthenium Catalyst for Highly Efficient Enantioselective Intramolecular C(sp<sup>3</sup>)–H Amidation," *Journal of the American Chemical Society* 141 (2019): 19048–19057.
23. H. Li and M. B. Hall, "Mechanism of the Formation of Carboxylate From Alcohols and Water Catalyzed by a Bipyridine-Based Ruthenium Complex: A Computational Study," *Journal of the American Chemical Society* 136 (2014): 383–395.
24. G. Manca, E. Gallo, D. Intriери, and C. Mealli, "DFT Mechanistic Proposal of the Ruthenium Porphyrin-Catalyzed Allylic Amination by Organic Azides," *ACS Catalysis* 4 (2014): 823–832.
25. P. Devi, V. D. Ghule, and S. Muthaiah, "Ruthenium-Induced Decomposition of Hexamethylenetetramine as a Tool for the Acid-Free Sommelet Reaction in Aqueous Medium," *Journal of Organic Chemistry* 89 (2024): 4366–4374.
26. L. M. Sousa, D. M. S. Araújo, K. M. Oliveira, et al., "Synthesis, Spectroscopic Characterization and Computational Study of Ru(II)/DMSO Complexes With Monocoordinated Carbazate Ligands," *Journal of Coordination Chemistry* 73 (2020): 1605–1618.
27. M. K. Ghosh, S. Mandal, A. Islam, S. Mohapatra, and S. Chattopadhyay, "Ruthenium-Carbon(Aryl) Bond Cleavage and Change in the Ligand Coordination Mode in a Four-Membered Ortho-Metalated Ruthenium(II) Organometallics Promoted by Thiolato Ligands," *ChemistrySelect* 2 (2017): 6710–6716.
28. R. Ben Said, K. Hussein, B. Tangour, S. Sabo-Etienne, and J.-C. Barthelat, "A Density Functional Theory Study of Dinitrogen Bonding in Ruthenium Complexes," *Journal of Organometallic Chemistry* 673 (2003): 56–66.
29. J. Flanagan, W. P. Griffith, and A. C. Skapski, "The Active Principle of Caro's Acid, HS05-: X-Ray Crystal Structure of KHS05·H<sub>2</sub>O," *Journal of the Chemical Society, Chemical Communications* 23 (1984): 1574–1575.
30. Y. Gao, Y. Zhu, Z. Chen, Q. Zeng, and C. Hu, "Insights Into the Difference in Metal-Free Activation of Peroxymonosulfate and Peroxydisulfate," *Chemical Engineering Journal* 394 (2020): 123936.
31. M. J. Frisch, G. W. Trucks, H. B. Schlegel, et al., "Gaussian 16 Rev. C.01," in Wallingford, CT, 2016.
32. A. D. Becke, "Density-Functional Thermochemistry. III. The Role of Exact Exchange," *Journal of Chemical Physics* 98 (1993): 5648–5652.
33. J. Moto Ongagna, A. D. Tamafo Fouegue, B. Ateba Amana, et al., "B3LYP, M06 and B3PW91 DFT Assignment of nd<sup>8</sup> Metal-Bis-(N-Heterocyclic Carbene) Complexes," *Journal of Molecular Modeling* 26 (2020): 246.
34. M. Grelhier, T. Ayed, J.-C. Barthelat, et al., "Versatile Coordination of 2-Pyridinetetramethylsilylazane at Ruthenium: Ru(II) vs Ru(IV) as Evidenced by NMR, X-Ray, Neutron, and DFT Studies," *Journal of the American Chemical Society* 131 (2009): 7633–7640.
35. A. Song, J. C. Lee, K. A. Parker, and N. S. Sampson, "Scope of the Ring-Opening Metathesis Polymerization (ROMP) Reaction of 1-Substituted Cyclobutenes," *Journal of the American Chemical Society* 132 (2010): 10513–10520.
36. B. Tutkowski, E. Meggers, and O. Wiest, "Understanding Rate Acceleration and Stereoinduction of an Asymmetric Giese Reaction Mediated by a Chiral Rhodium Catalyst," *Journal of the American Chemical Society* 139 (2017): 8062–8065.
37. T. Zhang, T. Li, X. Wu, and J. Li, "Theoretical Study of Ruthenium(0)-Catalyzed Transfer Hydrogenative Cycloaddition of Cyclohexadiene and Norbornadiene With 1,2-Diols to Form Bridged Carbocycles," *Journal of Organic Chemistry* 84 (2019): 3377–3387.
38. F. Weigend and R. Ahlrichs, "Balanced Basis Sets of Split Valence, Triple Zeta Valence and Quadruple Zeta Valence Quality for H to Rn; Design and Assessment of Accuracy," *Physical Chemistry Chemical Physics* 7 (2005): 3297–3305.
39. L. Hückmann, S. Álvarez-Barcia, M. Fuhrer, B. Plietker, and J. Kästner, "Ruthenium-Catalyzed Secondary Amine Formation Studied by Density Functional Theory," *ChemCatChem* 13 (2021): 1383–1388.
40. G. Zhang, C. Liu, H. Yi, et al., "External Oxidant-Free Oxidative Cross-Coupling: A Photoredox Cobalt-Catalyzed Aromatic C–H Thiolation for Constructing C–S Bonds," *Journal of the American Chemical Society* 137 (2015): 9273–9280.
41. Y. Cheng, J. Yang, Y. Qu, and P. Li, "Aerobic Visible-Light Photoredox Radical C–H Functionalization: Catalytic Synthesis of 2-Substituted Benzothiazoles," *Organic Letters* 14 (2012): 98–101.
42. J. J. Warren, T. A. Tronic, and J. M. Mayer, "Thermochemistry of Proton-Coupled Electron Transfer Reagents and Its Implications," *Chemical Reviews* 110 (2010): 6961–7001.
43. C. Costentin, M. Robert, and J.-M. Savéant, "Concerted Proton–Electron Transfers: Electrochemical and Related Approaches," *Accounts of Chemical Research* 43 (2010): 1019–1029.

44. Y. Kondo, K. Inamoto, and K. Nozawa, "Palladium-Catalyzed C-H Cyclization in Water: A Milder Route to 2-Arylbenzothiazoles," *Synlett* 23 (2012): 1678–1682.

45. B. P. Moloto, P. Vermeeren, M. Dalla Tiezza, C. Esterhuysen, F. M. Bickelhaupt, and T. A. Hamlin, "Palladium-Catalyzed Activation of Carbon–Halogen Bonds: Electrostatics-Controlled Reactivity," *European Journal of Organic Chemistry* 2022, no. 26 (2022): e202200722.

46. M. Lei, Y. Tang, H. Wang, et al., "A Catalytic Strategy for Rapid Cleavage of C-Cl Bond Under Mild Conditions: Effects of Active Hydrogen Induced by Pd Nanoparticles on the Complete Dechlorination of Chlorobenzenes," *Chemical Engineering Journal* 419 (2021): 129510.

#### Supporting Information

Additional supporting information can be found online in the Supporting Information section.



## Author biography

**Name** Miss Pacharaporn Krawmanee  
**Date of Birth** 4 November 1996  
**Address** 61 Moo 2, Salaeng Subdistrict, Mueang Chanthaburi District,  
Chanthaburi, 22000  
**Education** The Degree of Master of Science in Applied Chemistry  
Department of Chemistry School of Science,  
King Mongkut's Institute of Technology Ladkrabang  
**Scholarship** RA/TA-2562-M017

### Academic Publications

1. Pacharaporn Krawmanee, M. Paul Gleeson and Duangkamol Gleeson, "Computational Investigation of the Ru-Mediated Preparation of Benzothiazoles From N-Arylthioureas: Elucidation of the Reaction Mechanism and the Origin of Differing Substrate Reactivity", *International Journal of Quantum Chemistry*, Vol. 124 (2024), Issue 19, e27480.
2. Thanachon Somnarin, Pacharaporn Krawmanee, Matthew Paul Gleeson and Duangkamol Gleeson, "Computational investigation of the radical-mediated mechanism of formation of difluoro methyl oxindoles: Elucidation of the reaction selectivity and yields", *Journal of Computational Chemistry*, Vol. 44, Issue 5, Pages 670-676.